

REPORT DOCUMENTATION PAGE

Form Approved
OMB No. 0704-0188

Public reporting burden for this collection of information is estimated to average 1 hour per response, including the time for reviewing instructions, searching existing data sources, gathering and maintaining the data needed, and completing and reviewing the collection of information. Send comments regarding this burden estimate or any other aspect of this collection of information, including suggestions for reducing this burden, to Washington Headquarters Services, Directorate for Information Operations and Reports, 1215 Jefferson Davis Highway, Suite 1204, Arlington, VA 22202-4302, and to the Office of Management and Budget, Paperwork Reduction Project (0704-0188), Washington, DC 20503.

1. AGENCY USE ONLY (Leave blank)		2. REPORT DATE 9 Jan 97	3. REPORT TYPE AND DATES COVERED
4. TITLE AND SUBTITLE Liquid Contact Luminescence From Semiconductor Laser Materials		5. FUNDING NUMBERS	
6. AUTHOR(S) Craig Cody Largent			
7. PERFORMING ORGANIZATION NAME(S) AND ADDRESS(ES) University of Florida		8. PERFORMING ORGANIZATION REPORT NUMBER 96-36D	
9. SPONSORING/MONITORING AGENCY NAME(S) AND ADDRESS(ES) DEPARTMENT OF THE AIR FORCE AFIT/CIA 2950 P STREET WPAFB OH 45433-7765		10. SPONSORING/MONITORING AGENCY REPORT NUMBER	
11. SUPPLEMENTARY NOTES			
12a. DISTRIBUTION AVAILABILITY STATEMENT Unlimited		12b. DISTRIBUTION CODE	
13. ABSTRACT (Maximum 200 words)			
DTIC QUALITY INSPECTED 2 19970116 017			
14. SUBJECT TERMS		15. NUMBER OF PAGES 133	
		16. PRICE CODE	
17. SECURITY CLASSIFICATION OF REPORT	18. SECURITY CLASSIFICATION OF THIS PAGE	19. SECURITY CLASSIFICATION OF ABSTRACT	20. LIMITATION OF ABSTRACT

LIQUID CONTACT LUMINESCENCE
FROM
SEMICONDUCTOR LASER MATERIALS

By

CRAIG CODY LARGENT

A DISSERTATION PRESENTED TO THE GRADUATE SCHOOL
OF THE UNIVERSITY OF FLORIDA IN PARTIAL FULFILLMENT
OF THE REQUIREMENTS FOR THE DEGREE OF
DOCTOR OF PHILOSOPHY

UNIVERSITY OF FLORIDA

1996

TO DONNA, MY WIFE AND BEST FRIEND

ACKNOWLEDGMENTS

I would like to acknowledge the unconditional love and faithful support of my wife, Donna Largent. This work would not have been possible without the cheerful companionship and heartfelt encouragement that she has provided since the day we met in 1988 and especially while we have been here at the University of Florida. To dedicate this work to her is a conspicuous understatement, for my debt to her is beyond words.

I would like to express my sincere thanks to my advisor, Dr. Peter S. Zory. He has been both a technical and personal mentor during my studies and I have truly enjoyed working for him. He has a way of explaining complicated subjects that makes the concepts understandable while not dumbing down the information content. I hope that I have developed some of these communication skills under his guidance and will be able to transfer them to others.

I would also like to thank the members of my committee; Dr. Gijs Bosman, Dr. Frederik Lindholm, Dr. Ramakant Srivastava, and Dr. Chris Stanton. I have appreciated the guidance they have provided for this dissertation and their contribution to my understanding of semiconductor properties and devices. Special thanks also go to Dr. Sheng Li, from whom I took several classes, for his helpful comments on this dissertation. I would also like to thank my parents for the emphasis they have always placed on education and excellence.

I would be remiss if I didn't recognize the other students with whom I have worked during the last few years. Particular thanks go to Jeong-Seok "Jason" O, Chia-Fu

"Jeff" Hsu, Bob Widenhofer, Carl Miester, Mike Grove, and Chih-Hung "David" Wu.

The PAL circuit model was predominantly created by Bob Widenhofer and his knowledge of circuits and their modeling was invaluable. Bob McClain and the other departmental staff have smoothed some of the bumps in the road and I have appreciated their help.

On a bureaucratic note, I would like to recognize the United States Air Force, which provided my salary and tuition during the course of my studies. Funding for equipment purchases related to my research was provided by the Semiconductor Laser Applications Branch of the Phillips Laboratory, Kirtland Air Force Base, New Mexico. It is politically popular these days to talk about trimming the size of the federal budget and reducing the amount of money spent on the armed forces. In my case, I am glad that most of these arguments did not gain momentum until I was well into my doctoral studies.

TABLE OF CONTENTS

	<u>page</u>
ACKNOWLEDGEMENTS	iii
ABSTRACT	vii
CHAPTERS	
1 INTRODUCTION	1
Pulsed Anodization / Luminescence	3
Liquid Contact Luminescence	4
Liquid Contact Luminescence - Diagnostic.....	4
Liquid Contact Luminescence - Displays	5
Conclusions and Future Directions	6
2 PULSED ANODIZATION / LUMINESCENCE	7
Introduction.....	7
Pulsed Anodic Oxidation (Anodization) Overview	8
Traveling Oxide Phenomenon	10
Pulsed Anodization for Diffraction Grating Fabrication	11
Holographic Setup	13
Photoresist Considerations.....	13
Alignment Procedure for Holography Setup	15
Grating Fabrication Procedure	17
Grating Characterization.....	18
Pulsed Anodization Undercutting Experiments	18
Pulsed Anodization Luminescence (PAL)	21
PAL - Initial Observation and Experimental Setup	22
PAL - Spectral Characteristics.....	23
PAL - Temporal Characterization.....	29
PAL Circuit Model.....	30
Post-oxide Growth PAL - Comparison using Experiments and Modeling	35
Emission Delay vs. Pulse Width.....	36
PAL for Electrically Isolated Sample	37
PAL for Electrically Exposed Sample	42
Modeling of Light Emission and Delay.....	43

3 LIQUID CONTACT LUMINESCENCE	46
Literature Search Results	47
Liquid Contact Luminescence Process	49
LCL as a Lambertian Source	55
LCL during Substrate Anodization	58
Applications of LCL	62
4 LIQUID CONTACT LUMINESCENCE - DIAGNOSTIC.....	63
Luminescence Temporal Stability (LTS) Problem.....	63
Standard Contact and GWA Electrolyte	64
Standard Contact and EDTA Electrolyte.....	66
Insulated Contact and GWA Electrolyte.....	67
Relative Internal Quantum Efficiency Measurements	71
Low Level Injection.....	75
High Level Injection	78
LCL Sample Holder	80
5 LIQUID CONTACT LUMINESCENCE - DISPLAYS	85
Photoelectrochemical Introduction	86
Solvents, Supporting Electrolytes, and Redox Couples.....	91
Solvents.....	91
Supporting Electrolytes.....	92
Redox couples.....	93
Oxidation-Reduction (Redox) Reactions.....	93
Light Emission using Non-aqueous Solvents	96
Solution Resistance vs. Supporting Electrolyte Concentration	100
Solution Resistance vs. Redox Couple Concentration.....	103
Electrolyte Comparison	106
Non-aqueous Electrolyte Lifetime Experiments.....	110
6 SUMMARY AND FUTURE DIRECTIONS	117
Summary	117
Future Directions - Diagnostic.....	118
Future Directions - Displays	121
APPENDIX: CHEMICAL PROPERTIES	124
REFERENCES	129
BIOGRAPHICAL SKETCH	132

Abstract of Dissertation Presented to the Graduate School of the University of Florida in
Partial Fulfillment of the Requirements for the Degree of Doctor of Philosophy

LIQUID CONTACT LUMINESCENCE
FROM
SEMICONDUCTOR LASER MATERIALS

By

CRAIG CODY LARGENT

August, 1996

Chairman: Peter S. Zory

Major Department: Electrical and Computer Engineering

Semiconductor diode lasers are now widely used in many applications such as optical memories (e.g. compact-disk players) and fiber-optic communications. Recently, we discovered that a liquid contact made to standard diode laser material can be used to obtain light emission resulting from electron-hole recombination in the "active" layer buried in the multilayer epitaxial structure. Since the active layer is responsible for light amplification in diode lasers made from such material, this liquid contact luminescence phenomenon has potential as a new type of diode laser material evaluation technique. In addition, since the efficiency of the light emission process can be high, the liquid contact luminescence phenomenon has the potential for use as a new type of flat panel display (FPD).

Historically, the liquid contact luminescence phenomenon was discovered during the course of experiments involving pulsed anodic oxidation (anodization) of semiconductor laser materials in liquid electrolytes. When observed in the time domain, we found that the light was emitted, with long delays, after the termination of the voltage pulse. The complex relationship between oxide thickness, light emission intensity, and turn-on delay is described.

When the drive current direction is reversed from that used in pulsed anodization, the material is not anodized and light is emitted continuously from the active layer inside the semiconductor material as long as the current is on. Because this configuration produces light emission similar to that produced using photoluminescence (PL), we refer to it as liquid contact luminescence or LCL. LCL is a quick, inexpensive, and non-destructive way to obtain information about a variety of material parameters including peak emission wavelength, spectral linewidth, and relative internal quantum efficiency.

The use of aqueous electrolytes in the initial LCL experiments resulted in bubble generation. Based on a systematic study of non-aqueous solutions, it was discovered that it was possible to perform LCL without bubble generation and to reduce circuit resistance. As a consequence, we have now demonstrated the feasibility of using the liquid contact luminescence phenomenon as the basis for a new type of FPD technology.

CHAPTER 1

INTRODUCTION

In the last 50 years, there has been an explosion of science and technology in the fields of microelectronics and optoelectronics. Indeed, the unprecedented technical developments in semiconductors have revolutionized our lives in ways unimaginable just a few decades ago. Lasers that can be modulated at frequencies in excess of 1 GHz have opened the door to the “Information Age,” where a marriage of electronics and photonics has led to applications such as the internet, digital communications, optical recording, and compact disc players. Most of these applications have been made possible by advances in heteroepitaxy that have expanded the materials available for use in these devices to include compound semiconductors, most predominantly those composed from column III and column V elements. Metal Organic Chemical Vapor Deposition (MOCVD) and Molecular Beam Epitaxy (MBE) are now used to grow high quality semiconductor laser wafers that have direct bandgaps suitable for light emission at many wavelengths, from blue to the mid-infrared.

Electrically pumped at low voltages, semiconductor diode lasers have found their widest application to date in the music industry due to their use in compact disk players. Because these lasers are small (typical dimensions of $500 \mu\text{m} \times 500 \mu\text{m} \times 100 \mu\text{m}$) and highly efficient (50% wall plug efficiency), they have proven useful for applications that require spectrally coherent, high power optical radiation in a reliable package with no

moving parts. Long haul trunk telephone transmissions are almost entirely the domain of fiber optic technology with diode laser transmitters.

The characterization of epitaxially grown semiconductor laser material is a well developed field with a variety of tools available to provide researchers with information about laser wafer uniformity and quality. Recently, during experiments related to the fabrication of visible semiconductor lasers, we have developed a novel technique that generates bright emission from semiconductor wafers using a liquid contact. We have named this technique liquid contact luminescence (LCL). LCL opens up new avenues for material characterization and new opportunities for luminescent applications such as flat panel displays.

We have used LCL as a quick, inexpensive, and nondestructive technique to obtain information about a variety of epitaxial laser wafer material parameters at the unprocessed wafer level. Several of these wafer qualities are: peak emission wavelength, spectral linewidth, and relative light emission capability versus current density. Additionally, LCL has been used to determine relative values of internal quantum efficiency (η_i) for laser material.

In addition to applications of LCL for wafer characterization, we believe that it has possible display applications. Flat panel display technology has progressed rapidly in recent years. Cathode ray tubes are being replaced in many applications by flat panel displays (FPDs) that are continually increasing in brightness and pixel density. In military applications such as "heads-up displays," the compact size of FPDs makes them the technology of choice. The bright emission characteristics of semiconductor laser material naturally lead to applications for light emitting displays. In order to meet the requirements of

these applications, several problems inherent in the early LCL process needed to be solved. We solved some of these problems by redesigning the LCL liquid electrolyte and basing it on non-aqueous solvents. A systematic study of these non-aqueous solutions was performed and promising lifetest results were obtained.

Based on the successful demonstration of the novel LCL technique and its application to semiconductor laser wafer characterization, future experiments are proposed to improve the LCL efficiency and electrolytes.

1.1 Pulsed Anodization / Luminescence

Historically, the development of LCL followed the observation and characterization of pulsed anodization luminescence (PAL). In Chapter 2, an introduction to the theory and practice of pulsed anodization (PA), a technique developed at the University of Florida that is useful for depositing native oxides on a variety of semiconductor laser materials, is provided. The first application of PA to form submicron diffraction gratings is described and experiments that were performed to determine the undercutting present in the PA process are reported.

During the use of PA to form current blocking layers on visible laser wafers, anomalous light emission was observed. In Chapter 2, the characterization of PAL is described. PAL presented the first evidence that liquid contacts were useful for injecting current into the active region of semiconductor laser materials. Based on spectral measurements of the PAL emission and modeling results, we determined that the source of PAL was electron-hole recombination in the quantum well active region. Measurements of the temporal behavior of the PAL emission (the relationship between the timing of the PA current pulse and the emitted light) were used to develop a circuit model. We have

used this circuit model to quantitatively describe the changes in current flow and light emission both during PA and after the termination of oxide growth.

1.2 Liquid Contact Luminescence

As stated previously in this introduction, we have developed a novel technique to produce bright emission from semiconductor wafers using a liquid contact, LCL. In Chapter 3, we describe the results of a literature search concerning liquid contacts to semiconductors. Although liquid contacts have been used extensively by electrochemists to fabricate liquid junction solar cells, to study the semiconductor electrode/liquid electrolyte interface, and to make electrical contact to materials in which the fabrication of standard electrical contacts is difficult (e.g. porous silicon), they have not been utilized to electrically generate light from buried layers in multilayer, epitaxially grown, semiconductor materials. The fundamental processes occurring in LCL are explained including current injection at the semiconductor electrode-liquid electrolyte interface. Experiments demonstrating that LCL is a Lambertian source and that LCL occurs during pulsed anodization of the n-type wafer substrate in certain configurations are reported.

1.3 Liquid Contact Luminescence - Diagnostic

As a diagnostic tool, LCL can provide much useful information about the quality of the epitaxial wafer prior to laser fabrication. In Chapter 4, some of the diagnostic techniques developed using LCL will be described along with data obtained by this method. The first subject covered is the decay of light emission as a function of time, a phenomenon observed in some LCL experiments. The explanation for this decay phenomenon and a sample contacting scheme which prevents emission decay is described. Next, the application of LCL to the measurement of relative internal quantum efficiency is discussed. A

theoretical model is proposed for LCL at both low and high injection levels. Experimental data is used to verify the model and demonstrate that the relative internal quantum efficiency can be measured at high injection levels. Finally, the design of a sample holder employed to obtain repeatable LCL measurements is described.

1.4 Liquid Contact Luminescence - Displays

Because of the bright emission properties of LCL, it has been proposed that displays incorporating LCL as the light emission source could be possible. If this is to be the case, then several problems inherent in the early LCL results needed to be solved. Chief among these problems were H₂ bubble formation at the semiconductor cathode and low cell efficiency, characteristics which depend on the electrolyte. In order to solve these problems, we performed a literature search to obtain more information about electrolytes used in electrochemistry. In Chapter 5, the electrochemistry of the semiconductor electrode-liquid electrolyte interface is explored and photoelectrochemistry experiments that sought to employ reactions at this interface to generate chemical fuels and electrical power from sunlight are described. Based on the chemical processes occurring in the electrochemical cell, we redesigned our electrolyte and tested these new electrolytes, which demonstrated improved characteristics over the original LCL electrolyte. Using electrolytes with non-aqueous solvents, we have accomplished the first demonstration of light emission from semiconductor laser materials using non-aqueous liquid contacts. Resistance measurements for new solvent/electrolyte/redox couple solutions are discussed and a systematic study comparing the light emission characteristics of several non-aqueous electrolytic solutions as a function of supporting electrolyte molarity is presented. Finally,

lifetests were performed using some of these non-aqueous electrolytes and we report on these results and conclusions drawn from the experimental data.

1.5 Conclusions and Future Directions

In Chapter 6, we summarize this work and propose several future directions. Based on the successful experiments using LCL, there are several areas of research which we believe would produce profitable results upon further exploration. Foremost among these experiments is the use of LCL in a pulsed format to obtain information about built-in charge at the p-n junction. Additionally, improvements in the LCL sample holder and electrolytic solution are proposed. The extension of the LCL technique to light emitting diode (LED) materials is also proposed. If LCL is to prove useful for FPD applications, significant reductions in materials cost will be necessary and may be possible using LED materials. Increases in luminescence lifetime and improvements in the electrolytic solution will also be required. Finally, practical FPD designs are required if LCL is to be used as the light generation mechanism for displays.

CHAPTER 2

PULSED ANODIZATION / LUMINESCENCE

2.1 Introduction

Pulsed anodization (PA) is a technique developed at the University of Florida that is useful for depositing native oxides on a variety of semiconductor laser materials. In this chapter, an introduction to the theory and practice of PA is provided, including a description of the process which we have referred to as the “traveling oxide” phenomenon, in which the oxide layer is recessed into the semiconductor material in a self-aligned manner. The first application of PA to form submicron diffraction gratings is described and experiments that were performed to determine the undercutting present in the PA process are reported. As described in Chapter 1, an anomalous light emission mechanism in semiconductor laser wafer material was observed during pulsed anodization (PA). In this chapter, the initial observation and characterization of the pulsed anodization luminescence (PAL) process are described. Based on spectral measurements of the PAL emission and modeling results, we determined that the source of PAL was electron-hole recombination in the quantum well active region. Measurements of the temporal behavior of the PAL emission (the relationship between the timing of the PA current pulse and the emitted light) were used to develop a circuit model. We have used this circuit model to quantitatively describe the changes in current flow and light emission both during anodic oxide formation and after the termination of oxide growth. Finally, experimental PAL results are compared with theoretical results produced using the circuit model.

2.2 Pulsed Anodic Oxidation (Anodization) Overview

Pulsed anodization (PA) is a technique developed at the University of Florida that is useful for depositing native oxides on a variety of semiconductor laser materials. This process has been used to fabricate low ridge height, wide stripe GaAs/AlGaAs lasers and low ridge height, thin p-clad, narrow stripe InGaAs/AlGaAs lasers. It has also been used to fabricate variable ridge height, narrow stripe GaAs/AlGaAs lasers [Grov94a], [Grov94b], [Huds94]. A complete description of the theory and practice of pulsed anodization can be found in the literature and will not be repeated here. However, in order to understand the experiments reported in this work, it is necessary to review the basic features of the pulsed anodization process.

As shown in Figure 2-9, PA is carried out by placing the semiconductor sample in an electrolytic cell, where it is connected to the positive terminal of a pulse generator and serves as the anode. The electrolyte used was a mixture of 40 parts ethylene glycol, 20 parts de-ionized water, and 1 part 85% phosphoric acid (GWA electrolyte) [Hasa76]. A noble metal, in our case, a platinized titanium grid, is connected through a variable resistor, R_{var} , and a 10Ω resistor to the negative terminal of the supply and serves as the cathode. We typically operate the pulsed power supply at maximum voltage and use the variable resistor to control the current flow in the circuit. The current flow through the circuit is monitored in real-time by measurement of the voltage drop across the 10Ω resistor. A high source impedance is used to cause the anodization to proceed under “constant current” conditions [Ghan83]. For typical oxide growths, the voltage pulse width is $700 \mu s$ and the value of R_{var} is in the range of $2-5 k\Omega$, resulting in current densities of ~ 50 mA/ m^2 .

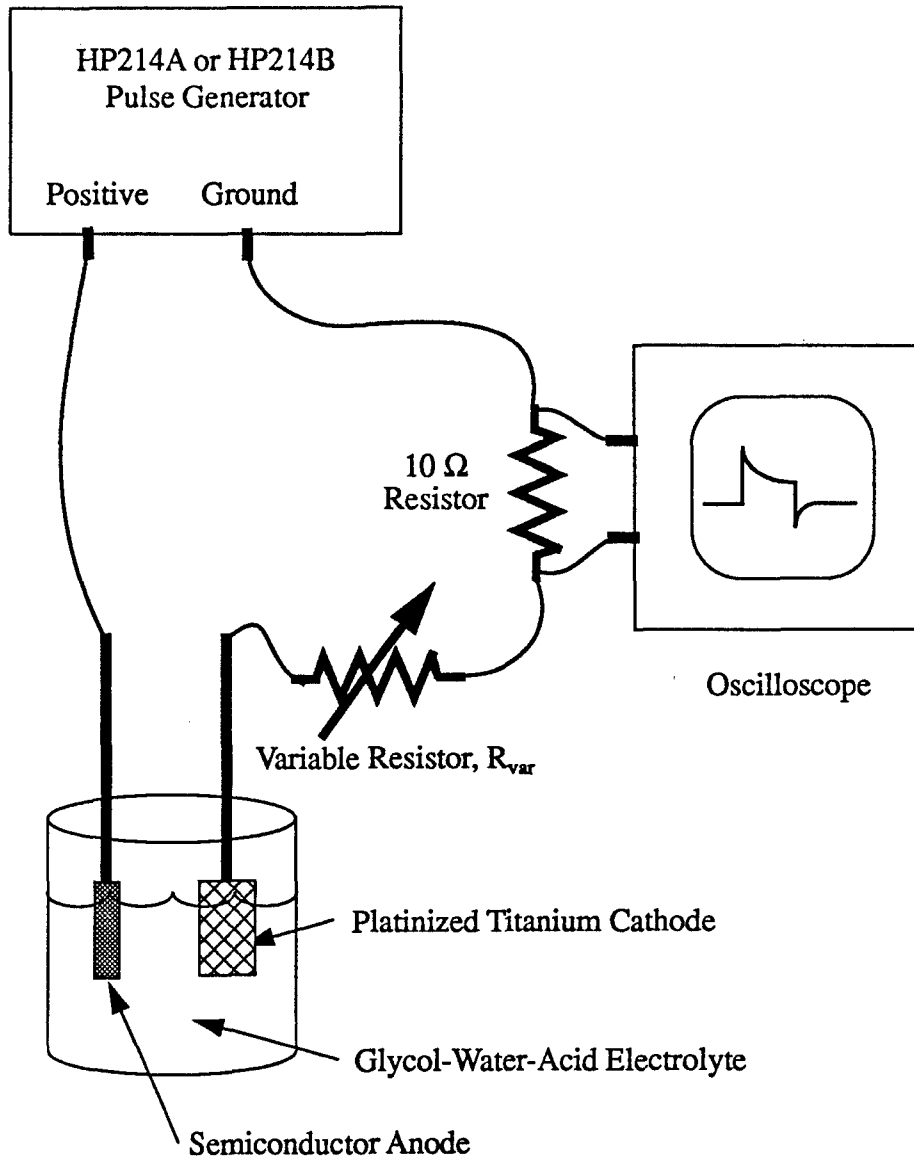


Figure 2-1. Schematic of the experimental setup used for pulsed anodic oxidation (anodization).

cm^2 . Utilizing these anodization parameters, oxide thicknesses on the order of 1000 Å are obtained in ~5 minutes.

Measurement of the voltage drop across the 10Ω resistor on an oscilloscope produces oscilloscope traces similar to those shown in Figure 2-2. Snapshots of the trace are shown at three times (t_0, t_1, t_2). As the oxide becomes thicker, the pulse shape decays from a top-hat shaped pulse to a pulse with an unchanged leading edge and a capacitively

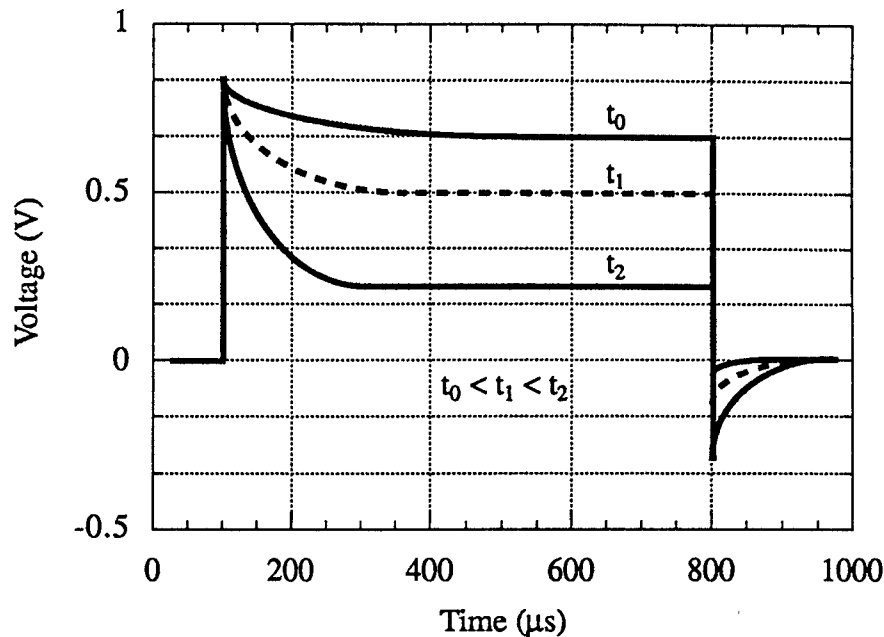


Figure 2-2. Representative oscilloscope trace during the pulsed anodization process.

reduced trailing edge. The pulse shape at t_1 or t_2 can be understood if one considers the capacitive effect of the oxide layer. When the voltage pulse is first applied to the circuit, current flows to charge the capacitor. Once the capacitor charges, the steady-state current flow ($0.5V/10\Omega$ for t_1) is determined by the resistance of the cell including the oxide layer. As the oxide thickens and increases in resistance (e.g. time t_2), the steady-state current flow decreases further. Additional details about the current pulse flowing in the 10Ω resistor, including the “negative” voltage measured after $800\mu s$ in Figure 2-2 are discussed in section 2.7, where the PA circuit model is presented.

2.3 Traveling Oxide Phenomenon

One significant way that the PA process differs from traditional insulator deposition processes is that the semiconductor material is consumed during the oxide growth process. For GaAs-based material systems, this material consumption process, combined

with the pulsed nature of the PA process, leads to a phenomenon that we have termed the "traveling oxide" phenomenon. The physical process that produces a traveling oxide is presented in Figure 2-3. Since the electrolyte used in the process is a mild etchant of the native oxide, the oxide grows when the current pulse is on and dissolves when it is off. This quasi-steady state of etching and growth allows for the formation of ridges with arbitrary height and oxides of arbitrary thickness up to about 2000 Å. Of course, one can achieve essentially the same result by a series of pulse anodization and oxide stripping steps, the final stripping step being eliminated when the desired ridge height is achieved. However, the simplicity and repeatability of the traveling oxide process makes it the process of choice for various structures including ridgeguide formation. In this case, the self-aligned nature of the pulsed anodic process is advantageous. Self alignment of the laser stripe and the oxide is inherent in PA because the semiconductor material is consumed during the traveling oxide formation process.

2.4 Pulsed Anodization for Diffraction Grating Fabrication

In addition to use of PA for current blocking layers in the variety of laser structures already discussed, we have used pulsed anodization to fabricate sub-micron diffraction gratings in semiconductor laser materials. We believe that this is the first report of the use of pulsed anodization to form such diffraction gratings. This section describes the holographic setup used for this demonstration, considerations related to photolithography and optical alignment, the actual fabrication process, and the procedures used to characterize the finished grating.

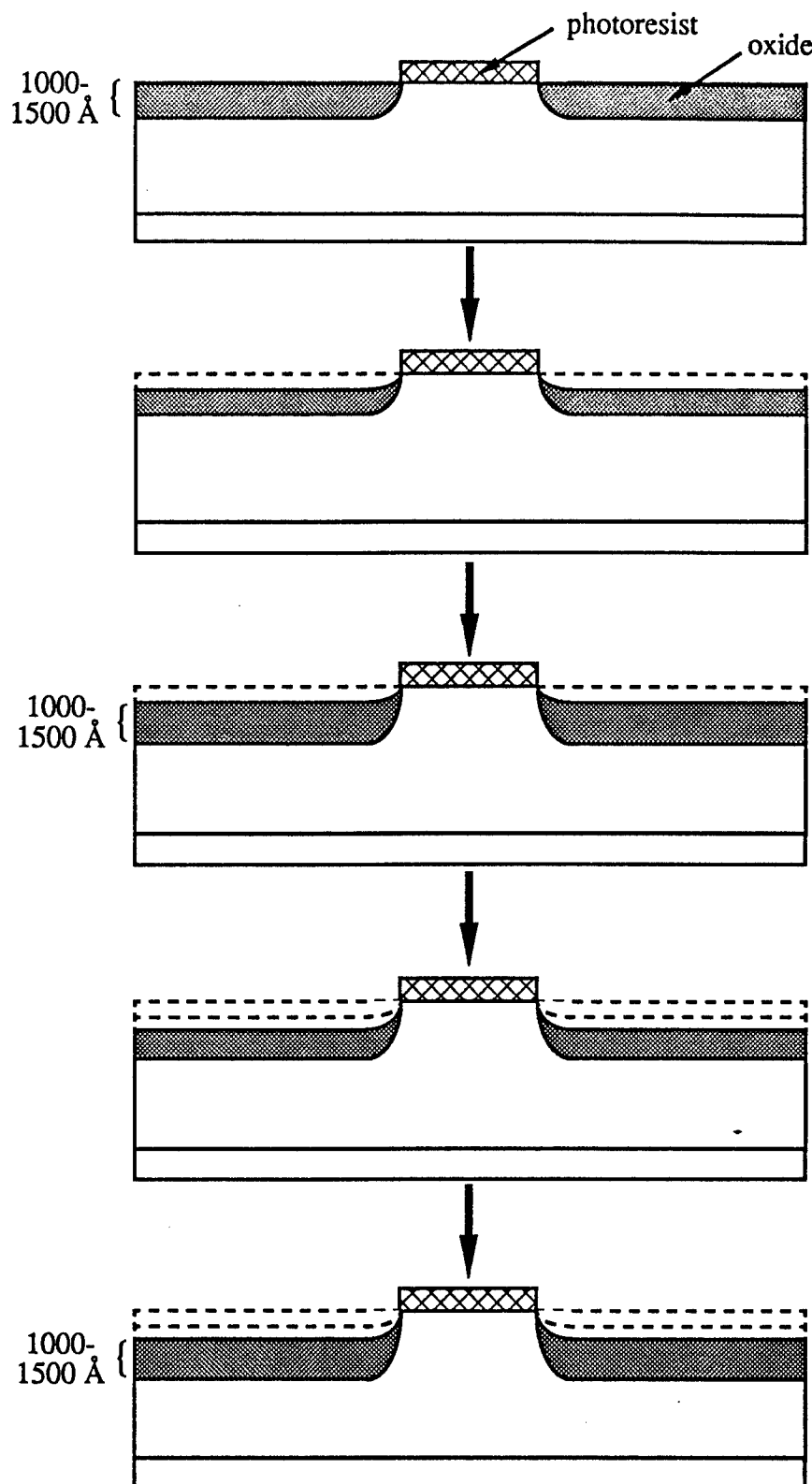


Figure 2-3. Process flow for traveling oxide phenomenon. Due to the pulsed growth and dissolution process, the oxide travels into the semiconductor material.

Holographic Setup

Figure 2-4 is a drawing of the experimental setup used for holographic grating fabrication. A Spectra-Physics model 164-06 argon ion laser that emitted \sim 100 mW of radiation at 4579 Å was used. The laser beam was aligned so that the beam height was equal to the height of the spatial filters across the entire area of the optical table. The output from the laser, polarized orthogonal to the plane of the optical table, was steered into a polarizing beam splitter that divided the incident beam into two equal beams, forming the legs of the holographic exposure system. The beam splitter was oriented so that the two beams were perpendicular to each other and at 45° angles to a line connecting the beam splitter and the sample holder. The beams were reflected off of mirrors and passed through Newport model 900 spatial filters with 10X microscope objectives. After the beams were cleaned up by the spatial filters, the divergent beams were passed through collimating lenses and interfered at the sample holder. The semiconductor samples were mounted on the holder perpendicular to the table and held in place by a vacuum chuck. At the sample holder, where the two collimated beams were interfered, a periodic variation in light intensity was produced. As one can see from the inset plot in Figure 2-4, the grating spacing for this configuration is determined by the angle between the normal to the sample surface and the incident beams (θ_{hol}). Through photolithography and PA, this periodic variation was transferred into the semiconductor samples.

Photoresist Considerations

When fabricating submicron grating features, the photoresist thickness is critical. To be an effective mask for anodic oxidation, the photoresist must develop completely through to the semiconductor surface. To reliably meet this requirement when fabricating

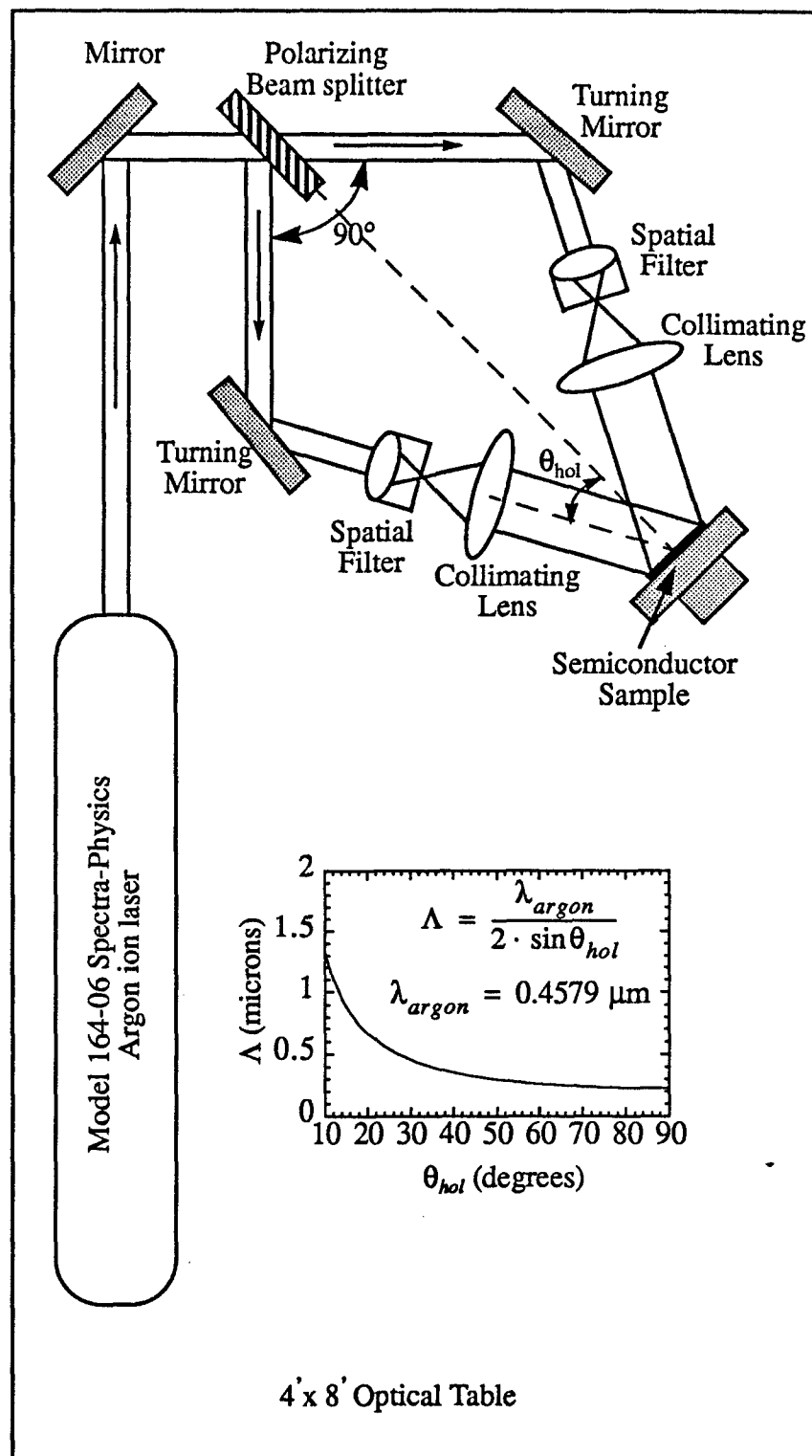


Figure 2-4. Experimental setup for holographic grating fabrication. Optical table was floated for stability.

gratings with submicron periodicity, thin photoresist films are needed. In previous work, 1000 Å photoresist films were used in the fabrication of a 2400 Å period mask [Come74]. In order to obtain 1000 Å photoresist films, I diluted Hoechst-Celanese AZ1350 photoresist with Shipley Thinner A. Alternating between the use of the photoresist spinner and the Nanometrics NanoSpec/AFT microarea gauge, which is a thin film profiler, I added thinner to the photoresist until photoresist films on the order of 1000 Å were obtained. At a ratio of approximately 3:1 (thinner:AZ1350), the photoresist thicknesses shown in Table 2-1 were obtained:

Table 2-1. Photoresist thicknesses as a function of spinner speed.

Spinner Speed (RPM)	Photoresist Thickness (Å)
3000	1000
4000	900

Alignment Procedure for Holography Setup

The polarizing beam splitter was oriented to produce two beams of equal intensity perpendicular to each other and at 45° angles to a line connecting the beam splitter and the sample holder. This is shown in Figure 2-4.

In order to ensure proper beam alignment during holographic exposure, we used a method that relied on the incident laser beams traversing opposite paths. The first step in the alignment procedure was to align the tilt angle of mirror M1 so that it reflected beam A in such a manner as to direct it along a path toward the sample holder at the desired holographic exposure angle, θ_{hol} . Proper alignment of this beam was critical as beam A was used to align beam B. A glass slide coated with evaporated metal was placed on the vac-

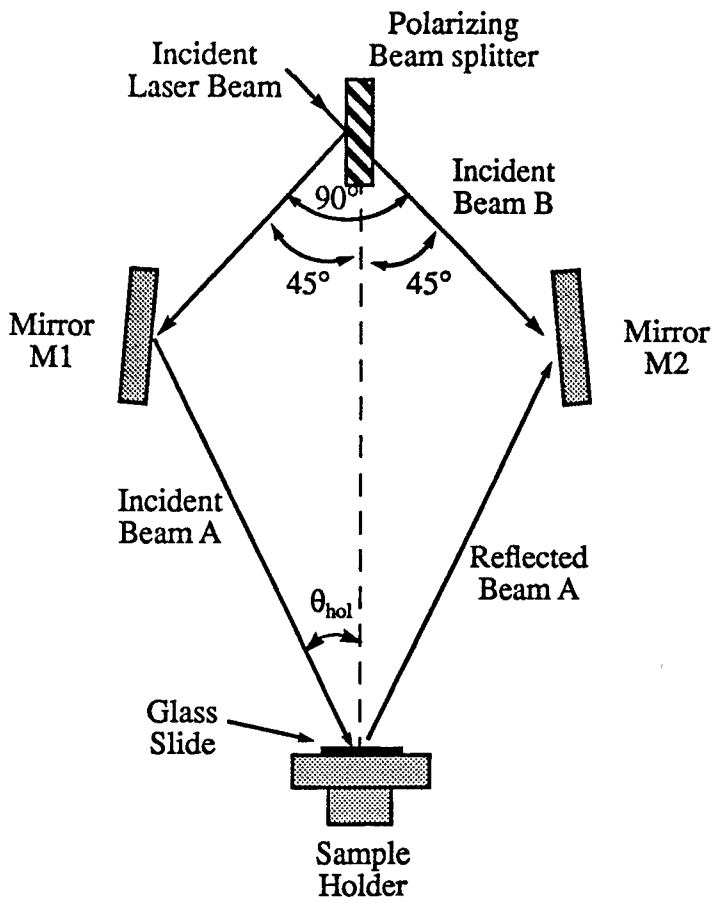


Figure 2-5. Alignment procedure for holographic grating setup.

uum chuck to allow for reflection at the sample holder. Because the desired outcome was to have both holography beams incident at θ_{hol} , the law of reflection:

$$\sin \theta_i = \sin \theta_r, \quad (2.1)$$

was used to obtain the alignment information for the beam in leg B. Tracing the path of the reflected portion of beam A up toward mirror M2, the position of mirror M2 was adjusted until the spot created on mirror M2 by the reflected beam A was aligned with the spot created on mirror M2 by beam B coming toward mirror M2 from the beam splitter. Finally, once the position of mirror M2 was fixed, the angle of mirror M2 was adjusted so that beam B traced the reverse of the path taken by beam A. Therefore, the two beams were traveling identical paths in opposite directions and θ_{hol} was equal for both exposure

beams. The equality of the angles θ_{hol} was used in the simplification of Eq. 2.2 to obtain Eq. 2.3 and the plot found in the inset in Figure 2-4.

The grating spacing was calculated using the following equation, which is a variant of the grating equation in reflection:

$$\Lambda = \frac{\lambda_{argon}}{\sin\theta_1 + \sin\theta_2}. \quad (2.2)$$

For the case in which the angles of incidence for the hologram are the same and equal to θ_{hol} , which was the setup we utilized, Eq. 2.2 reduces to

$$\Lambda = \frac{\lambda_{argon}}{2 \cdot \sin\theta_{hol}}. \quad (2.3)$$

This is the equation that was used for the plot found in the inset in Figure 2-4.

Grating Fabrication Procedure

Using the holographic setup already described, samples with thin photoresist were mounted on the vacuum chuck and exposed with a grating pattern. Using the available output of the ion laser (~100 mW), the power in each leg of the holographic system was ~35 mW/beam after cleanup in the spatial filters. The diameter of the collimated beam was ~3 cm. Exposure times were varied and 30 seconds was found to be optimum. This value reliably produced a 50% duty cycle pattern in the photoresist that was observed using an optical microscope at large grating spacings. After exposure, the sample was developed in Hoechst Celanese AZ®312 MIF developer (diluted 1:1.2) for 30 seconds. The sample, now with patterned photoresist, was rinsed in DI H₂O and dried with N₂.

To transfer the periodic pattern from the photoresist to the semiconductor sample, the sample was placed in the anodization setup and anodized at ~50 mA/cm² (accounting for the 50% duty cycle of the photoresist) for 7 minutes. This anodization produced an oxide that was light blue in color. After the oxide growth process, and while both the ph-

toresist and the oxide grating were present on the surface of the laser wafer, the argon ion laser was used to verify grating definition as described in the next section.

In order to verify that the anodization had transferred the grating pattern into the semiconductor sample, acetone was used to remove the photoresist and the grating spacing was again measured. Finally the oxide layer was removed using a dilute KOH solution. Although the native oxides formed by PA are stable in a number of typical processing solvents (trichloro-ethane, acetone, and methanol), they are easily dissolved in a basic DI H₂O:KOH solution (pH ≈ 12).

Grating Characterization

In order to characterize the diffraction gratings after fabrication, we utilized the argon ion laser as a probe beam and the grating equation in reflection:

$$\sin \theta_i + \sin \theta_q = \frac{q\lambda_{argon}}{\Lambda}, \quad (2.4)$$

where θ_i is the angle of incidence, θ_q is the angle of the q-th diffracted order, q is the diffracted order number, λ_{argon} is the wavelength of the argon ion laser beam (4579 nm), and Λ is the grating spacing. Measuring the angles of incidence and diffraction, we calculated the grating spacing, Λ . For example, for gratings made with $\theta_{hol} = 45^\circ$, $\Lambda = 0.32 \mu\text{m}$. The grating spacing can be verified by setting the angle of incidence at 70° and measuring the angle of diffraction for the first order, which turns out to be 27° as shown in Figure 2-6.

2.5 Pulsed Anodization Undercutting Experiments

In defining stripes using pulsed anodization, accurate knowledge of the stripe width is always a useful and sometimes critical component of the design process. Although this information is less than critical for gain guided or wide stripe lasers, it is

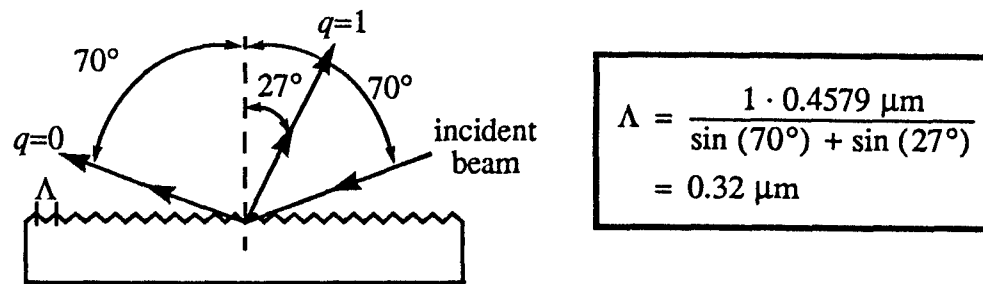


Figure 2-6. Characterization of the diffraction grating spacing, Λ , by measurement of the angles of incidence and diffraction.

important for the design and fabrication of ridgeguide lasers using pulsed anodization. For ridgeguide lasers fabricated using pulsed anodization, the existence of undercutting has been predicted [Huds94]. However, neither the existence of the proposed undercutting or the determination of the aspect ratio has been determined for PA. Although the exact determination of these undercutting parameters has not been fully determined, some initial experiments were conducted to provide initial understanding of the undercutting issue.

In a preliminary experiment to characterize the amount of undercutting, if any, samples were prepared with both ridgeguides and isolation grooves. A schematic diagram of the ridgeguide mask is shown in Figure 2-7 and a schematic of the isolation groove design is shown in Figure 2-8.

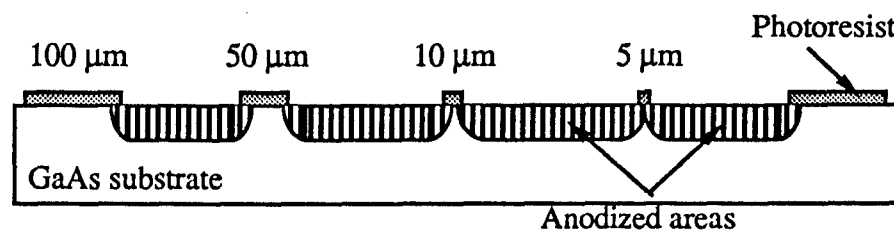


Figure 2-7. Schematic diagram for ridgeguide undercutting experiment.

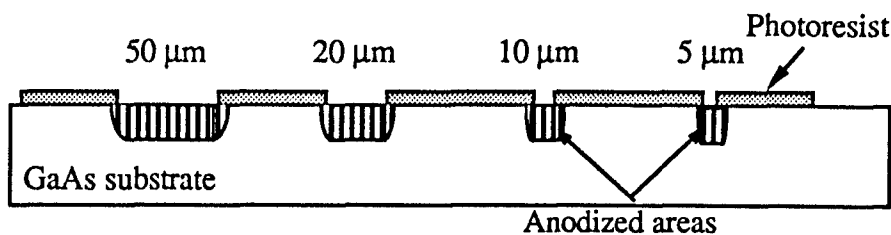


Figure 2-8. Schematic diagram for isolation groove undercutting experiment.

Two repolished GaAs substrate samples were prepared, one with the ridgeguide pattern and one with the isolation groove pattern. After the completion of photolithography, both of the samples were cleaved into two sections. One of the ridgeguide samples and one of the isolation groove samples were anodized for five minutes to provide a baseline for measurements. This anodization time was chosen because it is the minimum time required in our typical anodization processes and any undercutting that occurs during this short time will be unavoidable in typical processes. It should be noted that minimal undercutting is expected for this short time and the resulting oxide depth of $\sim 1200 \text{ \AA}$. The two remaining samples were anodized for 60 minutes. During anodization, the color of the oxide was monitored and the current density was adjusted to produce light blue oxide layers ($\sim 1200 \text{ \AA}$). Table 2-2 presents the data collected using a calibrated optical microscope for all four samples.

For the ridgeguide structure, there was not enough undercutting to measure it accurately with an optical microscope. Therefore, an SEM will be required to provide useful data for the ridgeguide structure.

For the isolation groove structure, the results were significantly different. Most noticeable is that the amount of undercutting was significant for all isolation groove widths, as the grooves widened measurably in each case.

Table 2-2. Undercutting experiment results for ridgeguide and isolation groove structures.

Ridgeguide Width (μm)		Isolation Groove Width (μm)	
5 Min. PA	60 Min. PA	5 Min. PA	60 Min. PA
5	3.6	5	8.8
10	9.1	10	13.2
		20	24
		50	54.3

The differences in undercutting for the two structures need to be examined and understood. Further development in this area will allow for ridgeguide designs that accurately account for undercutting during the design phase.

2.6 Pulsed Anodization Luminescence (PAL)

The first materials used in the development of PA here at the University of Florida were GaAs-based laser materials. Emission wavelengths for these materials are in the near infrared, typically 800-1000 nm. As a result, no notice was made that light was emitted during the anodization process. As the anodization process was extended to new materials, work was begun on the growth of native oxides by PA for use as current blocking layers in $(\text{AlGa})_{0.5}\text{In}_{0.5}\text{P}$ visible laser wafers. These laser materials were developed for applications including laser printing and HeNe replacement [Bour94].

During the PA of these visible laser wafers, it was observed that light was emitted from the laser wafers during the anodization process. The source of the emission and its relationship to the pulsed electrochemistry of the anodization cell was not clearly understood until recently [Larg95b]. This section focuses on the observation and characterization of pulsed anodization luminescence (PAL), an anomalous light emission mechanism observed for the first time in this material system. Measurements of the spectral and tem-

poral characteristics of light emitted from the laser wafers during the PA process are presented and explained.

PAL - Initial Observation and Experimental Setup

During the use of PA to form current blocking layers for $(\text{AlGa})_{0.5}\text{In}_{0.5}\text{P}$ laser wafers, two students, Doug Hudson and Mike Grove, happened to be operating the anodization setup in low light conditions and observed that red-colored light was emitted from the laser wafer surface during the PA process. Although there have been reports of visible emission from porous silicon during anodic oxidation with a constant voltage source [Mull93], [Bill91], we believe this is the first report of light emission from porous silicon during a pulsed anodic oxidation process. We refer to this emission as pulsed anodization luminescence (PAL).

The setup used for PAL experiments was the same as that used for pulsed anodization, as shown in Figure 2-9 except for the addition of a spectrometer or photodetector to monitor the light output. One of two voltage sources, an HP214A or an HP214B pulse generator, were used with similar results during the experiments. The solution, electrodes, and pulse generator were connected in series with a small (10Ω) resistor, which was used to monitor the current in the circuit, and a large variable resistor (R_{var}), which was used to control the current density (see Figure 2-1). For typical oxide growths, the voltage pulse width is $700 \mu\text{s}$ and the value of R_{var} is in the range of $2-5 \text{ k}\Omega$, resulting in current densities of $\sim 50 \text{ mA/cm}^2$. Utilizing these anodization parameters, oxide thicknesses on the order of 1000 \AA are obtained in ~ 5 minutes. For spectral measurements, an EG&G Princeton Applied Research Optical Multichannel Analyzer (OMA) was used. The temporal characteristics and intensity of the light emission from the wafer were detected using a silicon

PIN photodetector. The current pulse shape and the photodetector output were monitored on an oscilloscope.

PAL - Spectral Characteristics

In this section, measurements of the spectral profiles obtained by PAL, photoluminescence, and computer modeling are compared. Based on these spectral profiles and a comparison performed using two visible laser wafers, we have determined that the source of the PAL emission is the QW active region. Figure 2-9 is a schematic diagram of the $(\text{AlGa})_{0.5}\text{In}_{0.5}\text{P}$ semiconductor laser wafer (#428) used for these PAL experiments. The laser wafer was grown by MOCVD at Xerox Palo Alto Research Center (PARC) by Dr. David Bour.

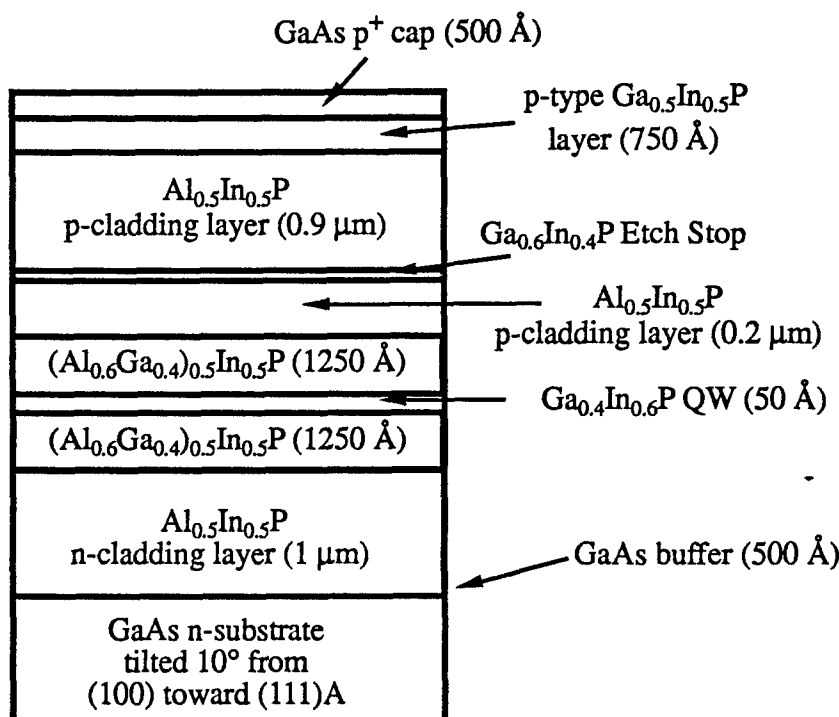


Figure 2-9. Schematic of $(\text{AlGa})_{0.5}\text{In}_{0.5}\text{P}$ semiconductor laser wafer (#428) used for pulsed anodization luminescence (PAL) experiments.

Figure 2-10 presents emission spectra obtained during PA and photoluminescence (PL). The PAL spectrum, which is offset below the PL profile for comparison, is similar in shape to the PL profile, which was taken at Xerox PARC [Larg94]. The PAL spectrum was obtained by imaging the emission from the epitaxial surface of the wafer into the OMA. For ease of comparison, both profiles were normalized to the same peak intensity and are plotted on the same wavelength scale. The peak emission wavelengths for both PAL (650 nm) and PL (649 nm) are blue-shifted with respect to the lasing wavelength (665 nm) of devices fabricated from the wafer. The similarity of the two profiles extends to the asymmetric high-energy tail characteristic of spontaneous emission. The strong correlation between these spectra lead to the conclusion that the source of the PAL emission is the QW active region.

Using electron-hole plasma theory, spontaneous emission profiles were calculated for the laser wafer used in this experiment. Figure 2-11 shows the calculated spectrum. One can see that the profile is similar to the profiles obtained from PL and PAL. This correlation between theory and experiment provided additional confirmation that the source of PAL emission was the QW active region.

According to the electron-hole plasma model [Zory93], the spontaneous emission rate per unit volume in a given energy range is calculated by multiplying the downward transition rate per unit volume by the number of optical modes in the energy range $d(h\nu)$:

$$\begin{aligned}
 r_{sp}(h\nu)d(h\nu) &\equiv W_{c \rightarrow v}[V\rho_{opt}(h\nu)d(h\nu)] \\
 &= \left(\frac{1}{h\nu}\right) \frac{\pi e^2 \hbar}{\bar{n} \epsilon_0 m_0} |M_{avg}|^2 \rho_{red}(E_{eh} - E_g') \rho_{opt}(h\nu) f_c (1 - f_v)
 \end{aligned} \tag{2.5}$$

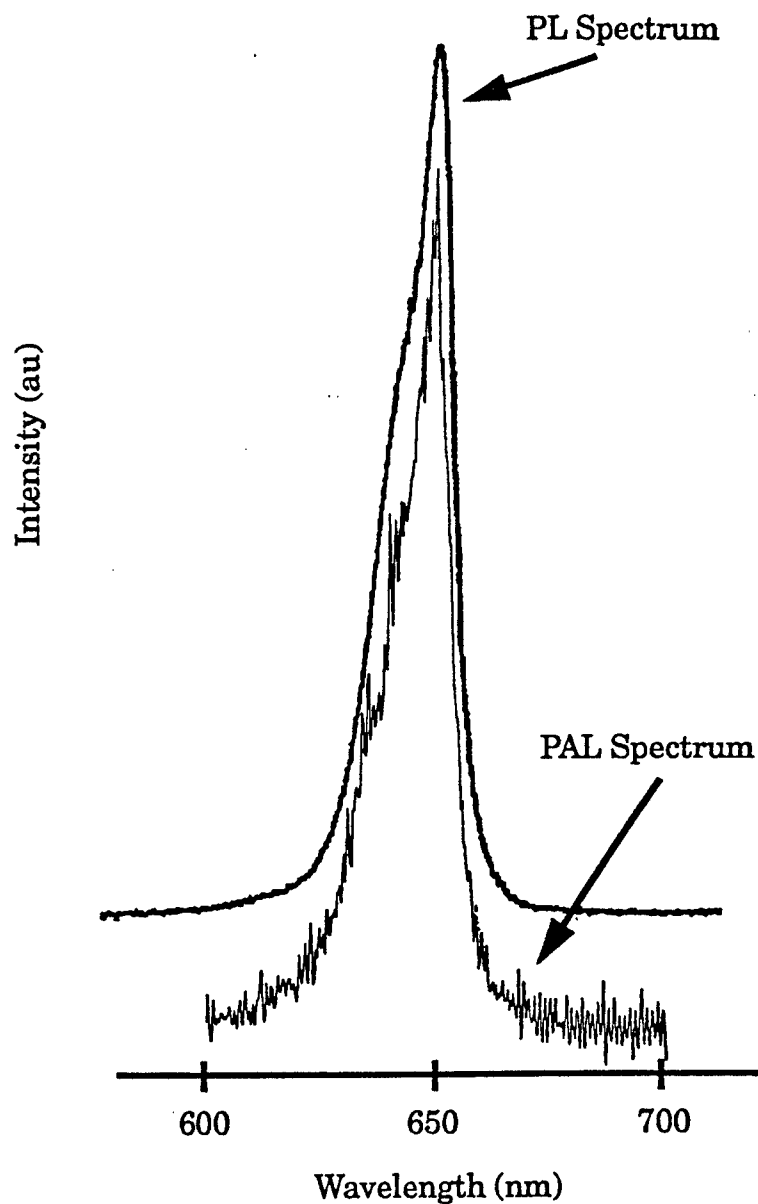


Figure 2-10. Pulsed anodization luminescence (PAL) and Photoluminescence (PL) spectra for $(\text{AlGa})_{0.5}\text{In}_{0.5}\text{P}$ semiconductor laser wafer.

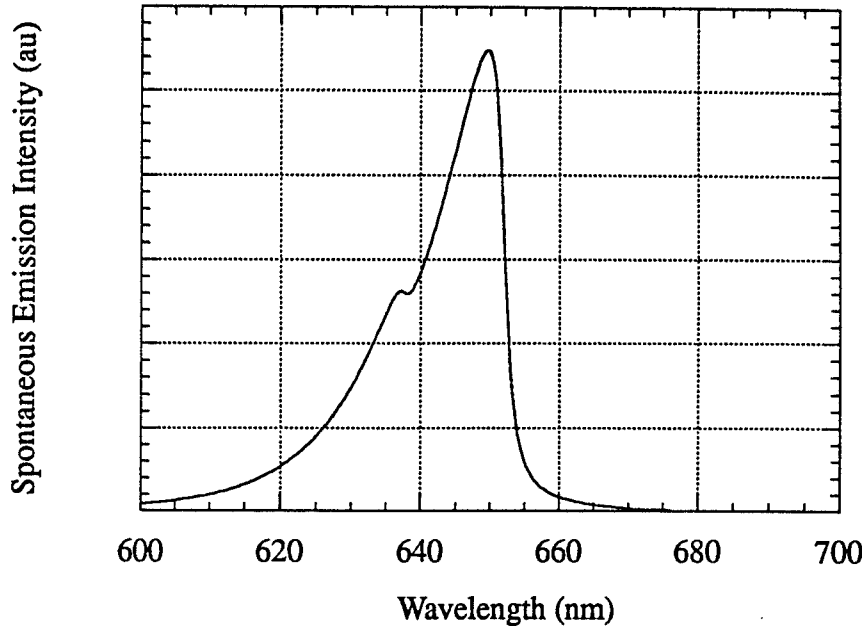


Figure 2-11. Calculated spontaneous emission spectrum for GaInP QW with $E_g=1.833$ eV and QW width=50 Å.

where $\rho_{opt}(hv)$ is the reduced density of states:

$$\rho_{opt}(hv) = \frac{\rho_k(k_{opt})}{\frac{dE}{dk_{opt}}} = 2 \frac{k_{opt}^2 dk_{opt}}{2\pi^2 dE} = \frac{1}{\pi^2} \frac{\bar{n}^2 n_g}{(\hbar c)^3} (hv)^2 \quad (2.6)$$

and $|M_{avg}|^2$ is the matrix element averaged over all three directions:

$$|M_{ave}|^2 \equiv \frac{1}{3} \sum |M_T|^2 \quad (2.7)$$

Substituting into Eq. 2.5,

$$r_{sp}(hv) = \frac{4\pi e^2 n_g}{\epsilon_0 h^2 c m_0} |M_{avg}|^2 (hv) \rho_{red} f_c (1 - f_v) . \quad (2.8)$$

Combining the three polarizations, the average matrix element can be written:

$$|M_T|_{ave}^2 = \frac{2}{3} |M_T|_{TE}^2 + \frac{1}{3} |M_T|_{TM}^2 . \quad (2.9)$$

The two terms for the TE polarizations are for transitions from the conduction band to the heavy hole and from the conduction band to the light hole:

$$\begin{aligned} \frac{|M_T|_{TE}^2}{|M|^2} &= \frac{1}{2}(1 + \cos^2 \theta_{nz}) \quad \text{for C-HH} \\ &= \frac{1}{6}(5 - 3\cos^2 \theta_{nz}) \quad \text{for C-LH} \end{aligned} \quad (2.10)$$

For the TM polarization,

$$\begin{aligned} \frac{|M_T|_{TM}^2}{|M|^2} &= 1 - \cos^2 \theta_{nz} \quad \text{for C-HH} \\ &= \frac{1}{3} + \cos^2 \theta_{nz} \quad \text{for C-LH} \end{aligned} \quad (2.11)$$

In both cases,

$$\begin{aligned} M &= \left(\frac{m_0}{m^*} - 1 \right) \frac{E_g + \Delta}{2(E_g + \frac{2}{3}\Delta)} m_0 E_g \quad \text{and} \\ \cos^2 \theta_{nz} &= \frac{E_{\Gamma, nz} + E_{v, nz}}{h\nu - E_g} \end{aligned} \quad (2.12)$$

where, $E_{\Gamma, nz}$ is the difference between the bottom of the electron quantized subband and the conduction band edge and $E_{v, nz}$ is the energy difference between the bottom of the hole quantized subband and the valence band edge.

Intraband relaxation plays an important role in the optical spectrum produced by quantum well lasers. The spectral shape becomes smooth and broad despite the sharp step-like density of states characteristic of a quantum well. The spontaneous emission coefficient as a function of photon energy including the effects of intraband relaxation is expressed as

$$R_{sp}(h\nu) = \int_{E_s}^{\infty} r_{sp}(E_{cv}) L(h\nu - E_{cv}) dE_{cv}, \quad (2.13)$$

where $L(hv - E_{cv})$ is the line broadening function characterized by the intraband relaxation phenomenon. Often, a Lorentzian distribution is used for this convolution. However, in the case of QW lasers, the Lorentzian lineshape function is not accurate. Our group has developed a computer model which, based on fundamental processes, provides accurate results for the convolution in Eq. 2.13 [Youn95]. This computer program was used for the spontaneous emission profile shown in Figure 2-11.

In addition to confirmation from PL and modelling results, an additional confirmation that the source of the PAL emission was the QW active region was a comparison we made using two visible laser wafers with slightly different epitaxial structures. Wafer #428 with the structure shown in Figure 2-9 was compared with wafer #431, which had an identical epitaxial structure except for a wider quantum well. Due to the difference in QW width, the lasing wavelengths of the lasers were different by ~25 nm. Because these laser wafers differed only in QW width, we expected that the PAL emission from the wafers would be blue-shifted from the respective lasing wavelengths the same amount for both wafers. Table 2-3 is a summary of the data collected by both PAL and PL, and the peak wavelength for laser operation for both wafers. The consistency of the blue-shift led us to the conclusion that the QW was, in fact, the source of the PAL emission.

Table 2-3. Peak wavelength data for Pulsed Anodization Luminescence (PAL), Photoluminescence (PL), and lasing.

Wafer	PAL Data		PL Data		Laser Peak λ (nm)
	Peak λ (nm)	Δ_1 (nm)	Peak λ (nm)	Δ_2 (nm)	
428	650	15	649	16	665
431	672	18	670	20	690

PAL - Temporal Characterization

In order to better understand the light emission mechanism, we examined the relationship between the current pulse and light output pulse. When the pulsed anodization process is first initiated, no light is emitted from the semiconductor material. As oxide growth progresses, changes occurring in the shape of the current pulse correlate with changes in the intensity and timing of the light emission as shown in Figure 2-12. This figure is a trace of an oscilloscope waveform with the current pulse measured across the $10\ \Omega$ resistor shown in Figure 2-12 (a), and the output from the photodetector displayed in Figure 2-12 (b). An actual oscilloscope trace is shown in part (c) of the figure. The solid and dashed lines correspond to data taken at approximately 2 and 5 minutes after oxide growth began, respectively. As can be seen in Figure 2-12, the current pulse flowing through the $10\ \Omega$ resistor changes significantly during the oxide growth process.

Due to changes in resistance and capacitance as the oxide forms, the pulse, as measured across the $10\ \Omega$ resistor, develops a reduced trailing edge and a significant "negative" current after the applied voltage returns to zero. As the oxide thickness increases, the negative current increases in magnitude, the peak intensity of the light emission increases, and the time delay between the end of the positive voltage pulse and the onset of light emission decreases. As the oxide layer reaches its final thickness, the negative current stabilizes and both the intensity and delay of the light emission stabilize. Although the correlation between the magnitude of the negative current pulse and the peak intensity and timing of the light emission is apparent, section 2.7 will explain that, in fact, the negative current is not the diode injection current that results in light emission, a result one would expect considering the long delays observed.

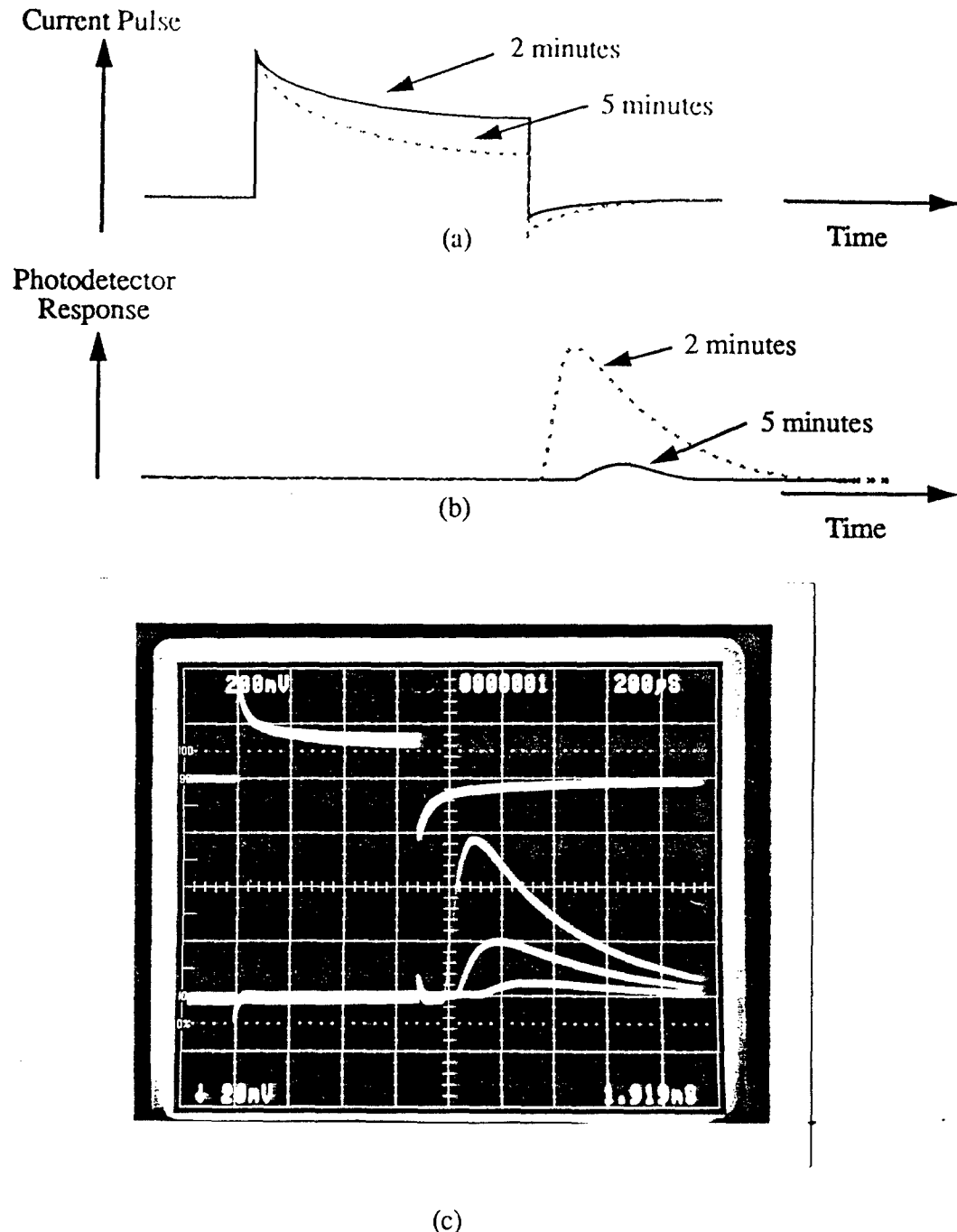


Figure 2-12. Schematic diagrams of (a) current pulse and (b) photodetector response at 2 minutes (solid line) and 5 minutes (dashed line) after initiation of PA. Measured oscilloscope trace (triple exposure) is shown in (c).

2.7 PAL Circuit Model

In order to improve our understanding of the electrical and optical processes occurring during the PAL process, an equivalent circuit model useful for simulating the

electrical processes was developed [Wide96]. Using this model, we have improved our original qualitative explanations of the temporal behavior of the PAL emission process to include quantitative modeling of the electrical and optical emission processes which occur during PAL. The schematic diagram of the equivalent circuit model developed for PAL is shown in Figure 2-13.

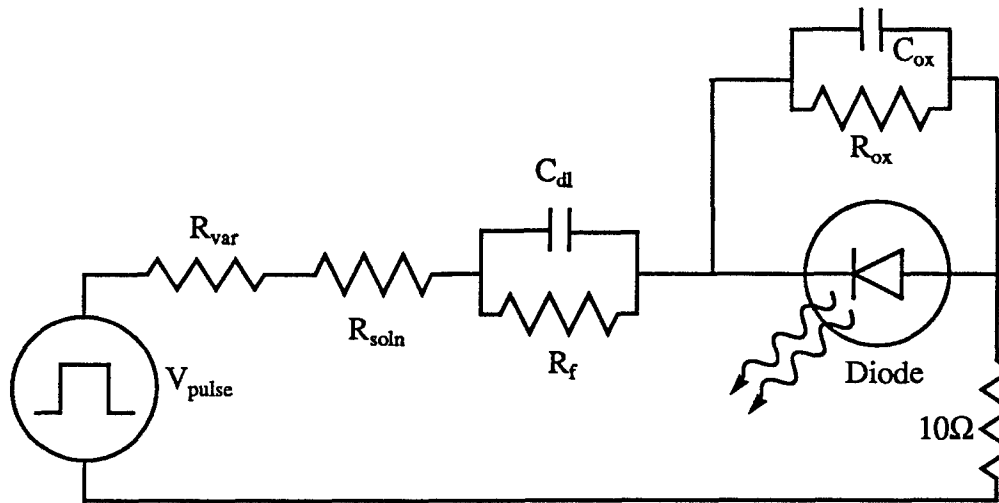


Figure 2-13. Schematic diagram of the PAL circuit used for circuit simulations.

Moving from the left to the right in the figure, the pulse generator provides a bias to the anodization setup. The variable resistor, which is used to externally control the current flowing in the circuit is connected in series with the circuit elements that reside in the beaker: the resistance of the electrolytic solution, the double layer formed at the semiconductor/electrolyte interface, and the semiconductor wafer. Current flow through the externally accessible portion of the circuit is measured using an oscilloscope, which measures the voltage drop across a 10Ω resistor. Values for the various circuit elements were determined using conventional circuit analysis techniques and data from previous research [Wide96]. Given these values, various conditions were modeled using PSPICE, a circuit simulation model.

A qualitative understanding of current flow in the PAL equivalent circuit and the resulting light emission may be obtained by examining Figure 2-14. When the pulse generator applies a voltage, V_{pulse} , to the circuit as shown in Figure 2-14 (a), current flows in the direction indicated by the arrows. This current flow results in the charging of capacitors C_{dl} and C_{ox} . During this time, the diode is under reverse bias and no light is emitted. As the capacitors become fully charged, the system current monitored via the 10Ω resistor decays to its steady-state value. When the pulse from the pulse generator turns off, it effectively shorts that portion of the circuit. As shown in Figure 2-14 (b), the capacitors begin to discharge, resulting in the “negative” current observed on the oscilloscope through the 10Ω resistor. Since C_{ox} takes a finite time to discharge and it is in parallel with the diode, the diode initially remains in reverse bias despite the reversal in the general direction of current flow. This is the source of the delay between termination of the input pulse and the onset of light emission. Finally, as shown in Figure 2-14 (c), once C_{ox} discharges sufficiently, the diode is forward biased, and light is emitted as hole-electron pairs recombine in the quantum well active region. One should note that the delay in light emission is not due to a delay between the injection of current into the active region of the semiconductor laser material, for these delays are much shorter than those measured here. As the oxide layer increases in thickness, the value of C_{ox} decreases, resulting in a progressive decrease in discharge time, which leads to shortening of the temporal delay between the trailing edge of the anodization pulse and the onset of light emission.

Figure 2-15 shows calculations of the currents flowing in the 10Ω resistor and the p-n junction diode inside the laser wafer as a function of time. Figure 2-15 (a) shows the calculated currents flowing at the beginning of the pulsed anodization process. The oxide

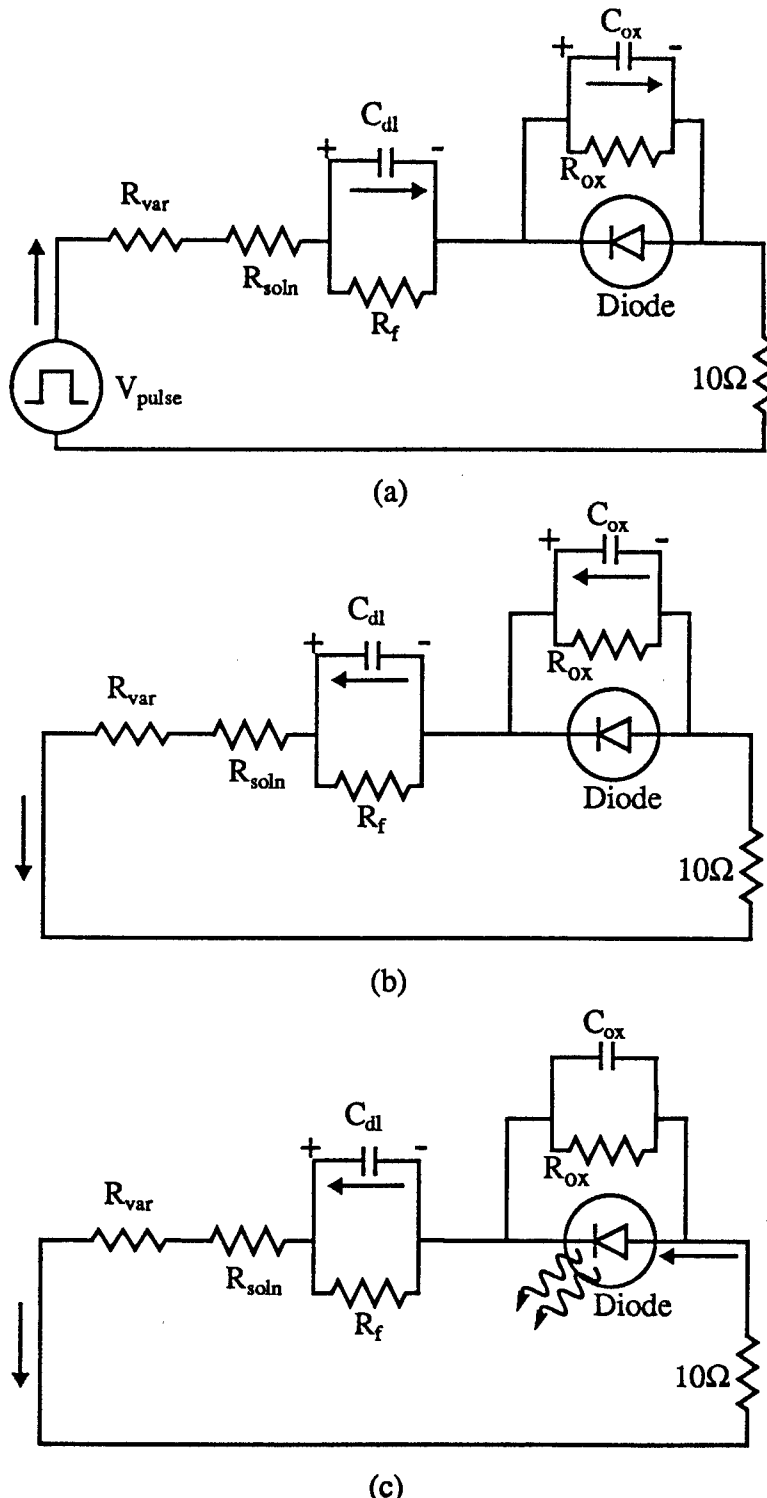


Figure 2-14. Circuit diagrams useful for explaining the current flow during PAL. (a) Charging of capacitors occurs during oxide growth. (b) Capacitors partially discharge after growth pulse ends. (c) Light is emitted as the double layer capacitor fully discharges.

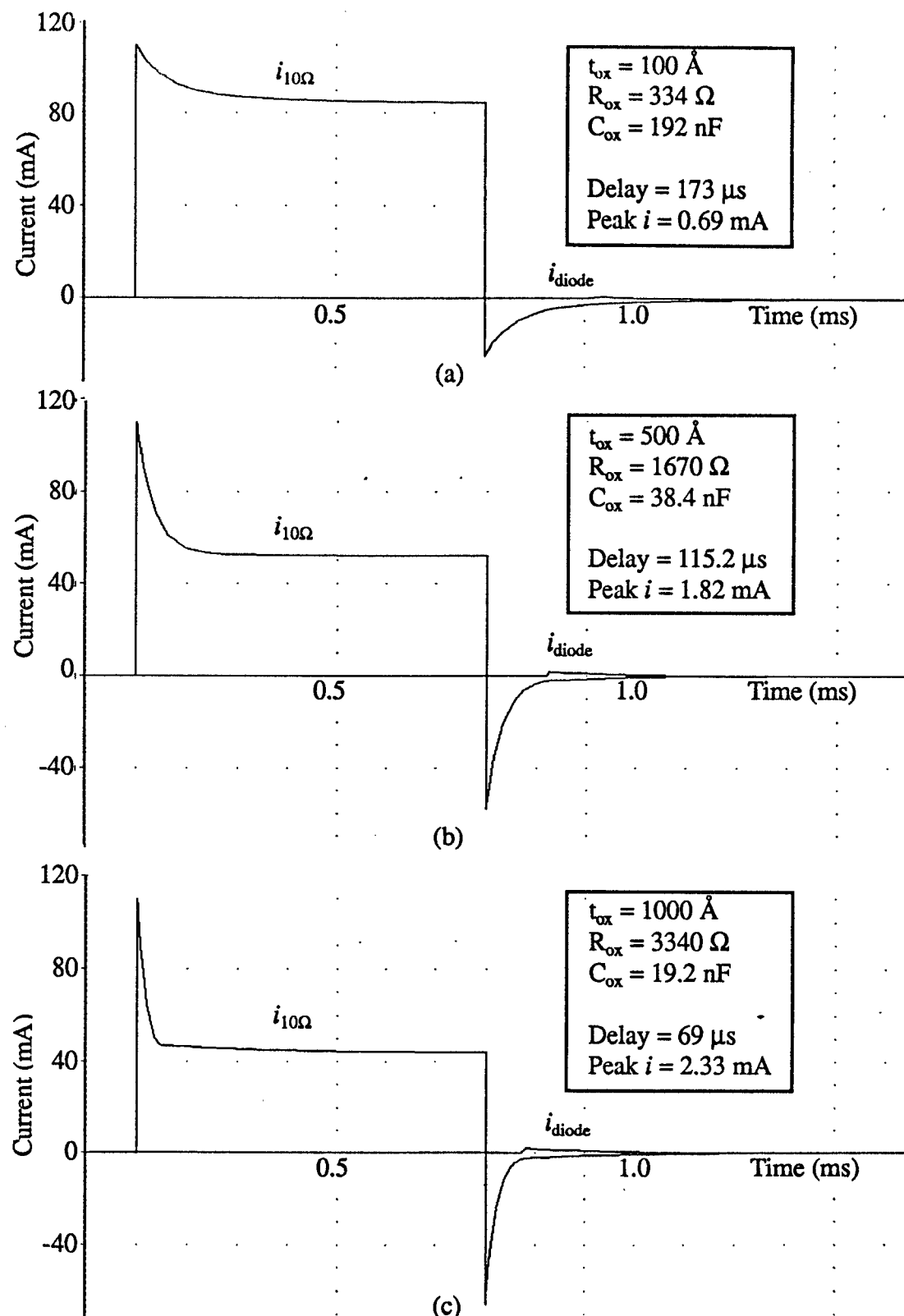


Figure 2-15. Modeling results for the 10Ω resistor current and the diode current as a function of time. Different profiles correspond to increasing anodic oxide thickness, t_{ox} : (a) 100 \AA , (b) 500 \AA , and (c) 1000 \AA .

layer in this case is assumed to be 100 Å thick, with a corresponding resistance of 334 Ω and a capacitance of 192 nF. The current flowing through the 10 Ω resistor is labelled as $i_{10\Omega}$ and the current flowing through the diode is labelled i_{diode} . As the oxide growth process progresses, the anodic oxide grows thicker, resulting in an increase in the oxide resistance and a decrease in the oxide capacitance. Figure 2-15 (b) and (c) show the current traces calculated as these parameters changed during oxide growth. An examination of the experimental data shown in Figure 2-12 and the calculated profiles shown in Figure 2-15 demonstrates close agreement between theory and experiment.

2.8 Post-oxide Growth PAL - Comparison using Experiments and Modeling

We have previously demonstrated that the PAL circuit model accurately describes the experimental PAL data during oxide growth with regard to the changes in the current flowing through the 10 Ω resistor and the diode current, which produces the observed light emission. An additional task of the modeling effort was to determine if the model would accurately reproduce measurements obtained after the oxide growth process had terminated. Three experiments were performed in which the anodization pulse width was varied after the oxide growth process had terminated. We observed that as the pulse width increased, the delay between the end of the post-oxide growth current pulse and the onset of light emission decreased and eventually saturated. Additionally, we examined the relationship between emission intensity (integrated spectral counts) and the post-oxide growth pulse width for two different anodization configurations. Using the models developed in the previous section, we were able to perform comparisons between this post-oxide growth experimental data and modeling results.

Several types of data are presented in this section, including trailing edge amplitude and integrated spectral counts. Examining the voltage pulse in Figure 2-2, the amplitude of the leading edge (0.83 V) and the trailing edge of the pulse can be specified at any given time. For example, at t_0 , the amplitude of the trailing edge is equal to 0.66 V and at t_1 , it is equal to 0.5 V. Since this voltage is measured across a 10Ω resistor, the conversion to current is straightforward. The amplitude of the trailing edge current decreases as the oxide thickness increases and eventually saturates. Values obtained for the amplitude of the trailing edge as a function of pulse width will be presented below. The other PAL data that is presented below is referred to as the integrated spectral counts, which is a measure of the amount of light emitted from the sample. This value is obtained as follows: the PAL emission was imaged into the slit of an optical multichannel analyzer (OMA) and spectra were obtained; the total number of counts registered on the OMA under the spectral envelope were integrated to obtain the value for integrated spectral counts.

Additional data is presented in this section that was collected using an oscilloscope during the PAL process. In the pictures of the oscilloscope screen, the current flowing through the 10Ω resistor is shown in the top trace. The bottom trace represents the response of the PIN 10-D photodetector. In all four of these pictures, the scale of the horizontal axis is $200 \mu s$ per division.

Emission Delay vs. Pulse Width

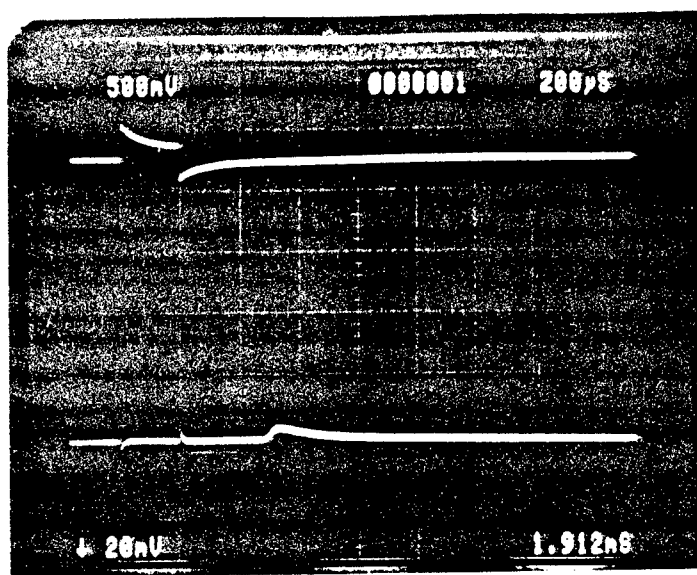
Although the emission intensity and delay stabilize as the oxide growth process terminates at a final oxide thickness, variation of the anodization parameters (pulse width, applied voltage, and R_{var}) after the current pulse stabilizes results in changes in the peak emission intensity and the delay between the end of the anodization pulse and the onset of

light emission. For example, as the width of the anodization current pulse, which is nominally 700 μ s during anodization, is increased from 200 μ s to 4000 μ s, the delay from the end of the positive current pulse to the beginning of light emission decreases from over 200 μ s to less than 30 μ s. Four oscilloscope traces that are representative of the decrease in delay to the onset of emission and the increase in peak emission intensity as the pulse width is increased are shown in Figure 2-16 and Figure 2-17. In all these pictures, the oxide thickness had reached its final value before the pulse width was varied and this data was collected.

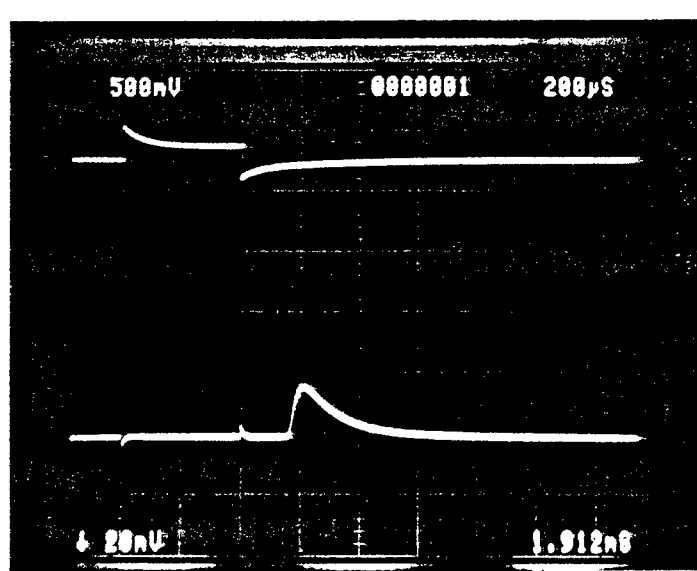
Figure 2-18 is a plot of the measured delays to the onset of emission as a function of pulse width. We observed that the delay began to saturate for pulse widths greater than 2000 μ s.

PAL for Electrically Isolated Sample

Two samples were prepared with different contact schemes to study the impact of electrical isolation of the p-side of the wafer on PAL. Contact to the first sample was made using the contact scheme shown in figure 2-19. In this contact scheme, the n-surface and the edges of the semiconductor wafer were isolated from the electrolyte using a mask. In this way, current was only allowed to flow through the p-surface of the semiconductor wafer. Figure 2-20 is a plot that displays the amplitude of the trailing edge current on the left ordinate axis and the integrated spectral counts on the right ordinate axis. This data was collected once the oxide growth and PAL emission had saturated. Care was taken during this experiment to guarantee that the oxide thickness remained at ~1000 \AA as the pulse width was varied. In order to maintain the oxide thickness at ~1000 \AA , the pulse width was increased to 1000 μ s after the emission data at each pulse width was collected.

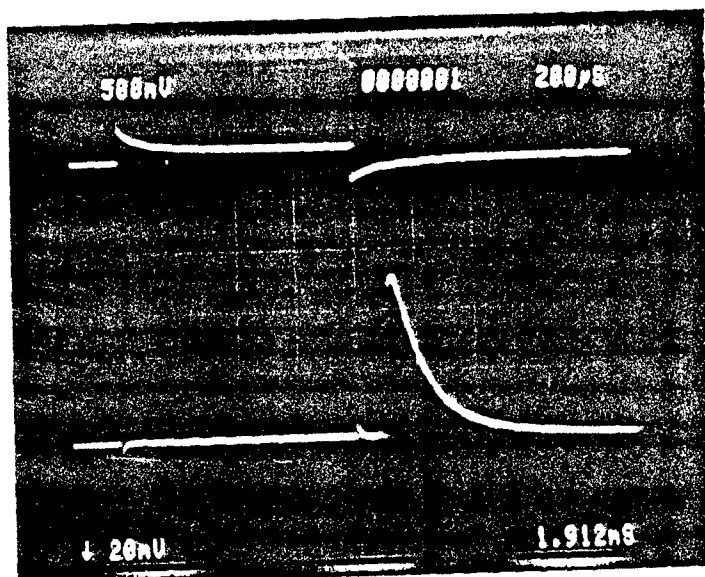


(a)

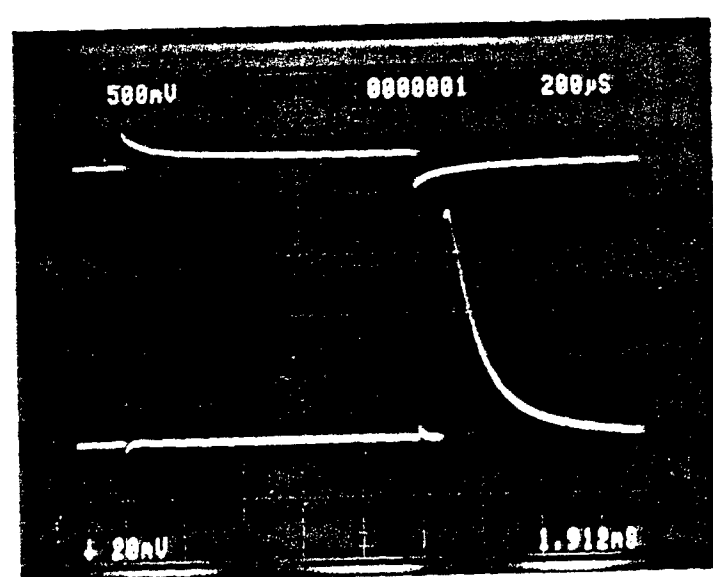


(b)

Figure 2-16. Oscilloscope traces obtained during PAL. The top curve on the trace shows the current flowing in the $10\ \Omega$ resistor as a function of time. The bottom curve on the trace shows photodetector response as a function of time. (a) Pulse width = $200\ \mu s$. (b) Pulse width = $400\ \mu s$.



(a)



(b)

Figure 2-17. Oscilloscope traces obtained during PAL. The top curve on the trace shows the current flowing in the 10Ω resistor as a function of time. The bottom curve on the trace shows photodetector response as a function of time. (a) Pulse width = $800 \mu\text{s}$. (b) Pulse width = $1000 \mu\text{s}$.

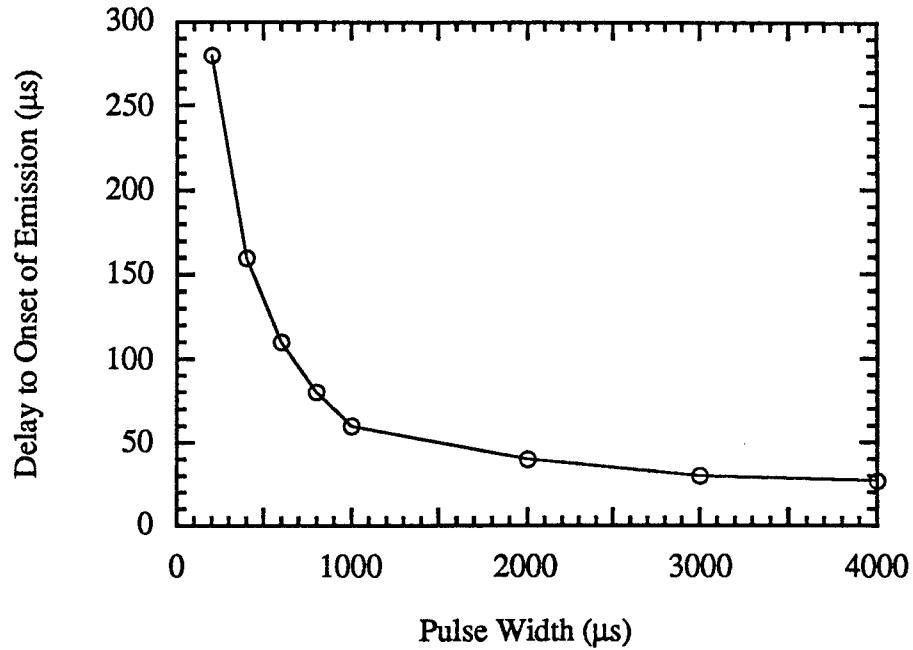


Figure 2-18. Experimental data for the delay from the end of the anodization pulse to the onset of light emission as a function of pulse width. The final oxide thickness was reached before the pulse width was varied.

Data was taken as explained above and the amplitude of the trailing edge current and integrated spectral counts are shown as a function of pulse width.

Examining Figure 2-20, one can see that the amplitude of the trailing edge current decreases rapidly as the pulse width is increased and saturates for pulse widths longer than 300 μs . At the same time, the integrated spectral counts increases and also saturates for pulse widths longer than 300 μs . We conjecture that the current pulse saturates as the capacitors become fully charged and thus an upper limit is placed on the light generating capability of PAL. It is also evident from the plot that there is a pulse width threshold for PAL emission, i.e. the anodization pulse width has to exceed a certain length before light

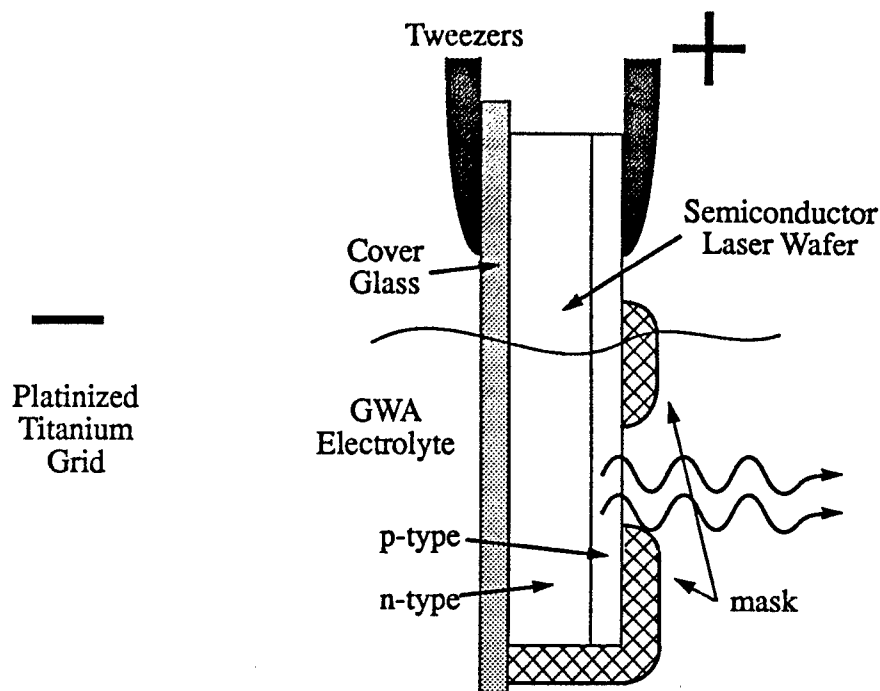


Figure 2-19. Side view of the contact scheme used for PAL testing with the n-surface and the edges of the semiconductor wafer isolated from the electrolyte. The electrolyte is contained in a beaker.

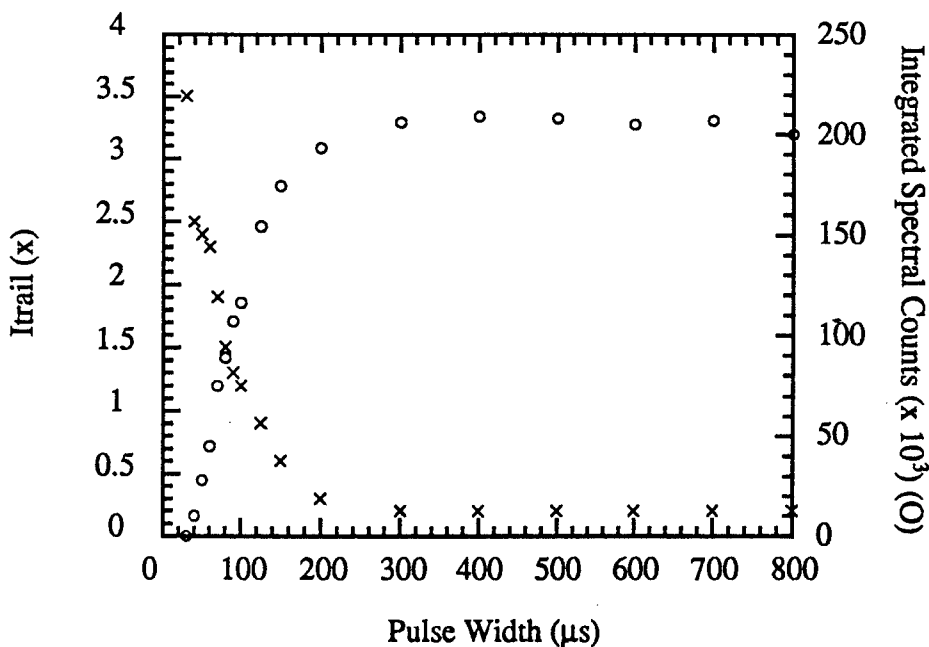


Figure 2-20. Amplitude of the trailing edge current and integrated spectral counts vs. pulse width for a PAL sample with the back of the wafer isolated from the electrolyte.

is emitted. This feature will be discussed at the end of this section when modeling results are presented.

PAL for Electrically Exposed Sample

Contact to the second sample was made using the contact scheme shown in Figure 2-21. The p-surface of the semiconductor laser wafer sample was masked with photoresist and was partially submerged in a beaker containing GWA electrolyte and a platinized titanium grid. The n-surface and the wafer edges were not masked and were exposed to the electrolyte.

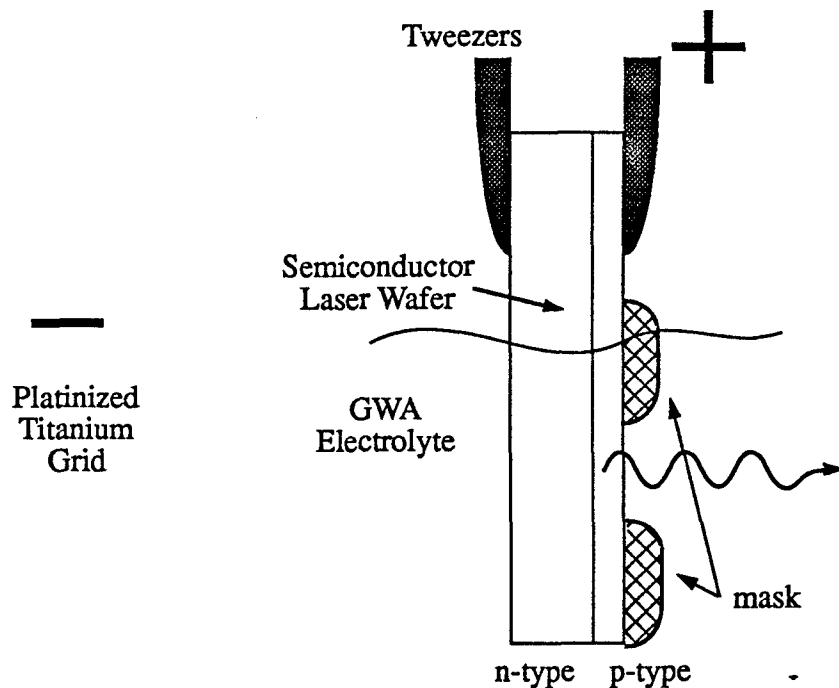


Figure 2-21. Side view of the contact scheme used for PAL testing with the n-surface and edges of the semiconductor wafer exposed to the electrolyte. The electrolyte is contained in a beaker.

Figure 2-22 is a plot of the amplitude of the trailing edge current vs. pulse width for the sample with the n-side and edges exposed to the electrolyte.

Differences between this data and data obtained with the previous contact scheme are evident. The saturation behavior for both the amplitude of the trailing edge current

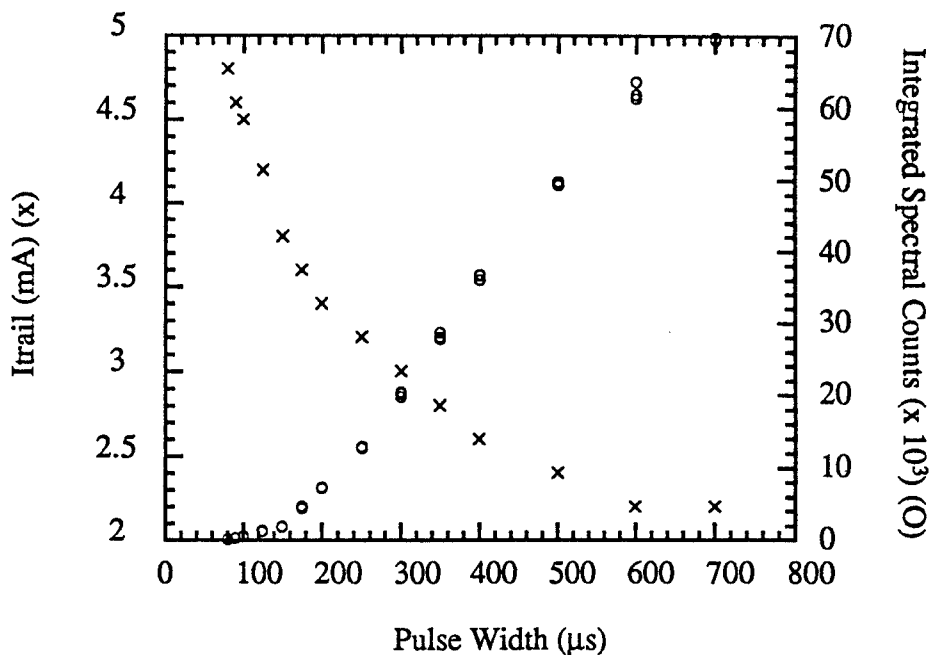


Figure 2-22. Amplitude of the trailing edge current and integrated spectral counts vs. pulse width for a PAL sample with the back of the wafer exposed to the electrolyte.

and the integrated spectral counts is not as pronounced as before. Additionally, the minimum amplitude of the trailing edge current is much greater for this case, in which a traveling oxide is formed on the n-side of the wafer. Finally, the pulse width threshold is greater in this case, most likely due to the anodization current flowing through the n-side of the wafer.

Modeling of Light Emission and Delay

Modeling was performed to determine if the model developed in section 2.7 would reproduce the experimental results obtained by varying the anodization pulse width after the oxide growth process had terminated. The oxide thickness was fixed at 1000 Å and simulations were run in which the pulse width was varied from 70 μs to 2000 μs. Figure 2-23 shows the results of these simulations.

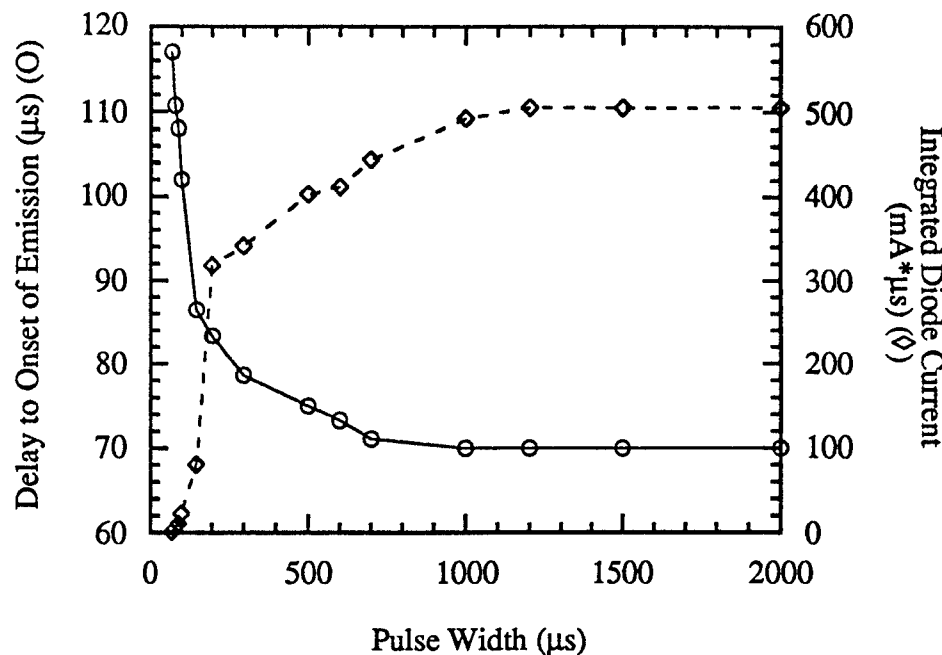


Figure 2-23. Delay to onset of light emission and integrated diode current vs. pulse width. Oxide thickness was fixed at 1000 Å.

On the left axis, the delay from the end of the anodization pulse to the onset of light emission is plotted vs. pulse width. The delay drops quickly as the pulse width is increased and saturates when the pulse width exceeds 1000 μs. This behavior compares favorably with the experimental results shown in Figure 2-18. Although the saturation of the experimental delay occurs at a lower delay level and around 2000 μs, the trend is closely followed. On the right axis, the estimated area under the diode current is presented vs. the pulse width. The variation in the integrated diode current data results from the fact that the PSPICE program used to model the circuit produces only current traces and therefore, the integration was performed manually. Because the diode current produces the light emission, this integrated current should correlate with the integrated spectral count

presented in Figure 2-20. In fact, there is a strong correlation between these two plots, as the integrated current rises sharply and saturates at longer pulse widths.

Finally, in the plot of integrated diode current vs. pulse width, the pulse width threshold previously discussed is evident. Although this behavior is not fully understood, it is possible that this experiment may be useful to electrochemists in determining the formation time for the double layer.

In conclusion, the circuit model developed to improve our understanding of the PAL process served its purpose. It allowed us to extend our understanding of the PAL process from qualitative descriptions to quantitative calculations. Not only did it reproduce the characteristics seen during the PA process, but it correctly reproduced data collected by varying the anodization pulse width after the oxide growth process had terminated.

CHAPTER 3

LIQUID CONTACT LUMINESCENCE

Recently, during experiments related to the fabrication of visible semiconductor lasers, we have developed a novel technique that generates bright emission from semiconductor wafers using a liquid contact. Using this technique, diode laser material can be forward biased using a liquid electrolyte to contact the standard p⁺-cap layer [Zory95]. We have named this technique, liquid contact luminescence (LCL). LCL has proven to be useful for material characterization and shows potential for diagnostic and display applications. We believe that LCL is new as both an optoelectronic wafer characterization technique and as a photoelectrochemical technique. In this work, the liquid electrolyte was transparent or semitransparent to the spontaneous emission emitted from the buried quantum well (QW) active layers so that one could easily measure the spectrum of the emitted light as a function of current through the wafers. As a consequence, one can use this LCL technique to measure wafer qualities such as peak emission wavelength, spectral linewidth and relative light emission capability versus current density. Additionally, LCL can be used to determine relative values of internal quantum efficiency (η_i) for laser material.

In this chapter, the results of a literature search on liquid contacts to semiconductors demonstrate that LCL is the first work to utilize liquid contacts to electrically excite semiconductor materials with p-n junctions, opening up new avenues for material characterization and new opportunities for luminescent applications. The fundamental processes

occurring in LCL are explained including current injection at the semiconductor electrode-liquid electrolyte interface. Experiments demonstrating that LCL is a Lambertian source and that LCL occurs during pulsed anodization of the n-type wafer substrate in certain contacting configurations are reported. Finally, some applications of LCL are introduced.

3.1 Literature Search Results

Liquid contacts have been used extensively by electrochemists [Kova92]. Liquid contacts to semiconductors have been used to fabricate liquid junction solar cells, to study the semiconductor electrode-liquid electrolyte interface, and to make electrical contact to porous silicon. Much of this research was performed in the early 1970s when interest in solar energy conversion produced significant development in the area of liquid junction solar cells, often referred to as photoelectrochemistry. These photoelectrochemical cells have some common links to photoelectric solar cells. Solar energy is absorbed and results in the generation of electron-hole pairs. Utilizing a built-in bias in the semiconductor, the electron-hole pairs are separated and used to generate useful current flow that is delivered to elements outside the electrochemical cell. Applications of these concepts to LCL will be covered in Chapter 5.

Based on the literature about photoelectrochemistry and liquid junction solar cells, we expected that some researcher would have used liquid contacts to study solid state photoelectric solar cells. Instead of operating the solar cell in the usual manner of absorbing light and producing current, it would be possible to contact the solar cell with a liquid electrolyte and characterize the cell by injecting current and measuring the light output. There has been a report of the use of electroplated contacts to perform electroluminescent

characterization of p-n junction solar cells using transparent contacts [Turn79]. In this work, the researchers found that electroluminescence was an effective diagnostic tool for characterizing polycrystalline solar cells. In fact, they found that the intensity and uniformity of the electroluminescent emission from forward-biased cells was correlated with improved photovoltaic response. However, we found no reference in which this technique was extended to the use of liquid contacts with p-n junction material for the purposes of light generation.

In investigating the semiconductor electrode-liquid electrolyte interface, both photoluminescence and electroluminescence have been used as characterization techniques. Experiments have used the luminescence produced at the interface to study surface modifications and coating, as well as interfacial energetics including surface minority carrier-capture velocities. Additionally, determination of flat band potentials and the types of surface states present at the interface have been accomplished. In this early work, the focus was placed on the chemistry of the semiconductor/liquid interface and was not extended to include processes occurring in the active region of p-n junction devices. In using these techniques, researchers have been only interested in recombination of electron-hole pairs occurring at the interface. In fact, we have found no reference in which liquid contacts were used with p-n junction semiconductor material. Because the recombination in these experiments is occurring at the semiconductor electrode-liquid electrolyte interface, it is claimed that use of the electroluminescence technique can only produce low quantum yields (10^{-4} - 10^{-5}) [Kova92]. In fact, the poor efficiency of light emission due to recombination at the surface of the semiconductor can be overcome if the recombination occurs at a p-n junction inside the semiconductor material.

Additionally, liquid contacts have received the attention of researchers in the field of light emission from porous silicon [Mull93]. In an attempt to make electroluminescent devices, liquid contacts have been utilized to provide a means of current injection into a material in which the fabrication of standard electrical contacts is difficult. The poor luminescent efficiency and brightness of porous silicon devices are issues which still require a considerable amount of research. As with the earlier work on electroluminescence at the semiconductor electrode-liquid electrolyte interface, a significant difference between the work related to porous silicon and the work reported here is that in the case of LCL, the electron-hole recombination occurs inside the epitaxial structure of the semiconductor material at the p-n junction. Therefore, in LCL, we utilize well developed semiconductor laser material systems in which the emission mechanisms are well understood and highly efficient. The considerable developments in metal organic chemical vapor deposition (MOCVD) and molecular beam epitaxy (MBE) that have made the epitaxial growth of high quality laser wafers routine can be utilized, allowing us to focus on other technical issues.

Therefore, based on our review of the pertinent literature, we believe that this is the first work to utilize liquid contacts to electrically excite semiconductor materials with p-n junctions. This use of liquid contacts opens up new avenues for material characterization and new opportunities for luminescent applications.

3.2 Liquid Contact Luminescence Process

The schematic diagram of the circuit used to generate pulsed LCL is shown in Figure 3-1. This electrochemical setup is similar to that used in PAL experiments as described in Chapter 2. A by-product of the LCL process using the GWA electrolyte is the

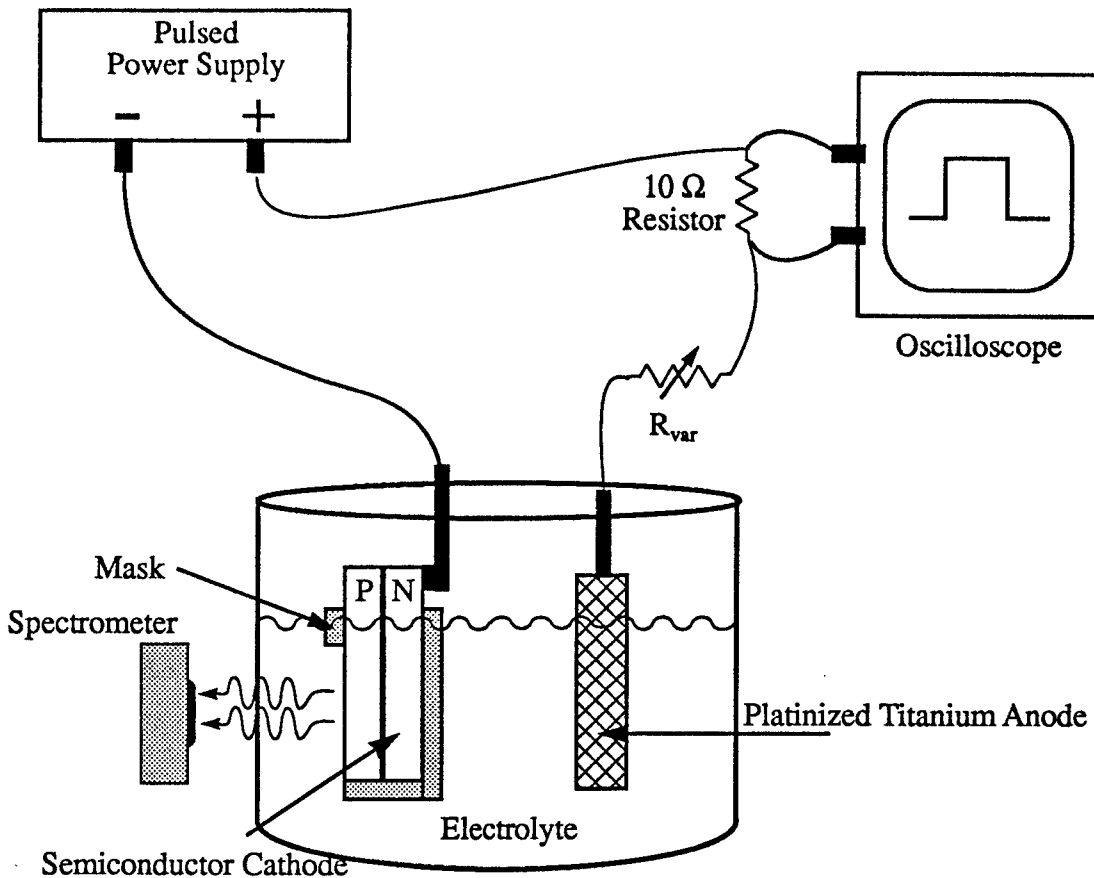


Figure 3-1. Schematic of the experimental setup used for pulsed liquid contact luminescence (LCL). The cathode had an epitaxial structure similar to that shown in Figure 3-4.

electrolysis of water as will be seen in the following paragraphs. Because it was the first electrolyte used in the LCL experiments, the LCL process using the GWA electrolyte will be described here.

The semiconductor laser wafer is placed in an electrochemical cell as the cathode. A platinized titanium grid is used as an anode and a pulsed or cw voltage is applied to the cell by a pulse generator or DC power supply. When voltage above a certain level is applied to the cell, light is emitted from the semiconductor wafer. In the pulsed LCL case, shown in Figure 3-1, the voltage drop across a 10Ω resistor is measured using an oscilloscope and the current flowing in the circuit is then calculated. In the cw LCL case, shown

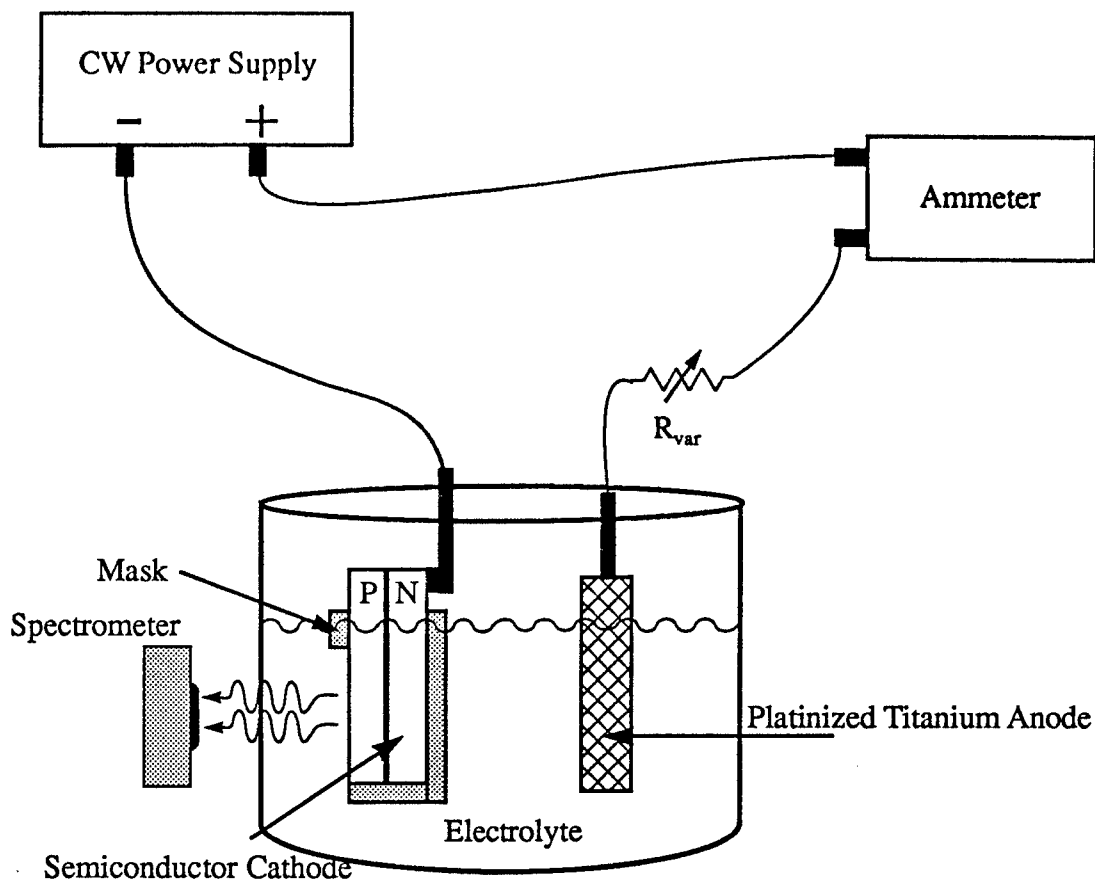


Figure 3-2. Schematic of the experimental setup used for cw liquid contact luminescence (LCL). The cathode had an epitaxial structure similar to that shown in Figure 3-4.

in Figure 3-2, an ammeter is used to measure the current flowing in the circuit. In both cases, a spectrometer facing the p-type surface of the wafer measures the spectrum of the light coming through the wafer surface.

As shown in Figure 3-3, positive hydrogen ions are attracted to the p⁺ surface of the semiconductor when voltage is applied to the cell. In order for current to flow, these hydrogen ions capture electrons from the p⁺-cap layer, thereby creating holes in the valence band. Since this process is essentially hole injection into the p⁺-cap layer, the liquid electrolyte serves as an electrical contact. Meanwhile, as shown in Figure 3-4, electrons are injected into the n-substrate from the n-contact. The injected holes and electrons

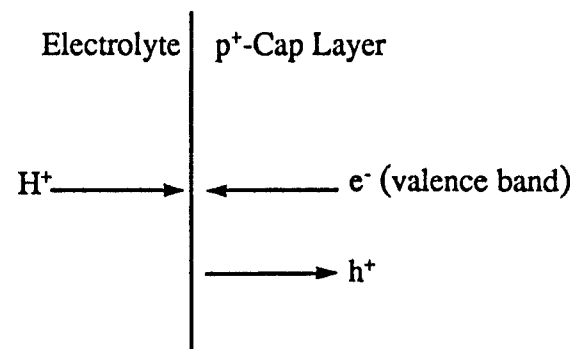


Figure 3-3. Basic LCL current injection mechanism using aqueous electrolytes.

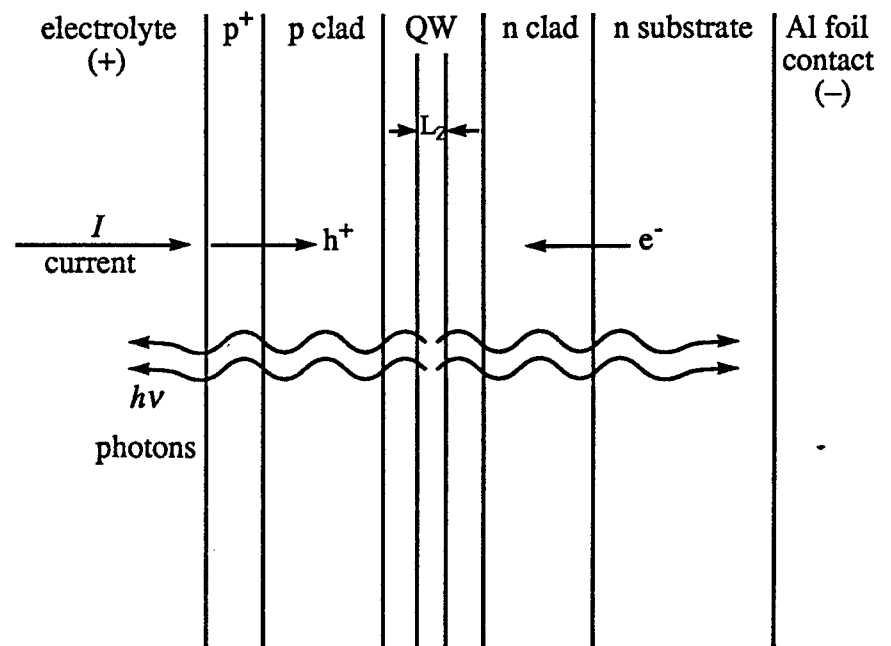
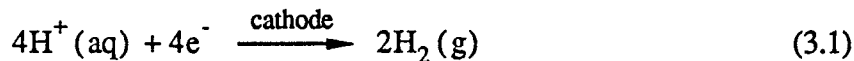


Figure 3-4. Electron and hole injection into a QW laser wafer using LCL.

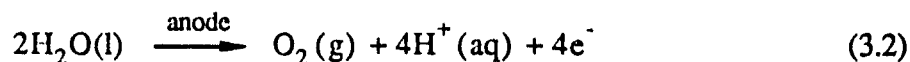
then drift toward the QW layer where some fraction of them recombine. If we define this fraction to be the internal quantum efficiency η_i , then $\eta_i I$ is the QW recombination current. Measurement of internal quantum efficiency will be discussed in section 4.2.

Another way to look at the current flow process is to use energy band diagrams. Figure 3-5 is a band diagram showing the current flow mechanisms active in LCL. As before, electrons are injected from the negative terminal of the power supply into the conduction band of the semiconductor (n-type region) on the left of the figure. Moving to the right in the figure, we know that radiative recombination occurs in the active region of the semiconductor structure. Because this recombination process requires holes in the valence band, we reason that holes must be injected into the valence band of the semiconductor (p-type region) from the electrolyte. Hole injection from the electrolyte is just another way of saying that an electron moves from the valence band of the semiconductor material into the electrolyte.

The movement of the hydrogen ion is responsible for current flow through the glycol:water:acid electrolyte [McQu84]. At the semiconductor/electrolyte interface (cathode), the hydrogen ions in solution extract electrons from the valence band of the p-type material and are reduced, resulting in the production of H₂ gas.



The extraction of electrons from the valence band is equivalent to the injection of holes as previously required for radiative recombination. Simultaneously at the anode, water molecules are oxidized to form O₂ gas, hydrogen ions, and electrons. This is shown in Eq. 3.2.



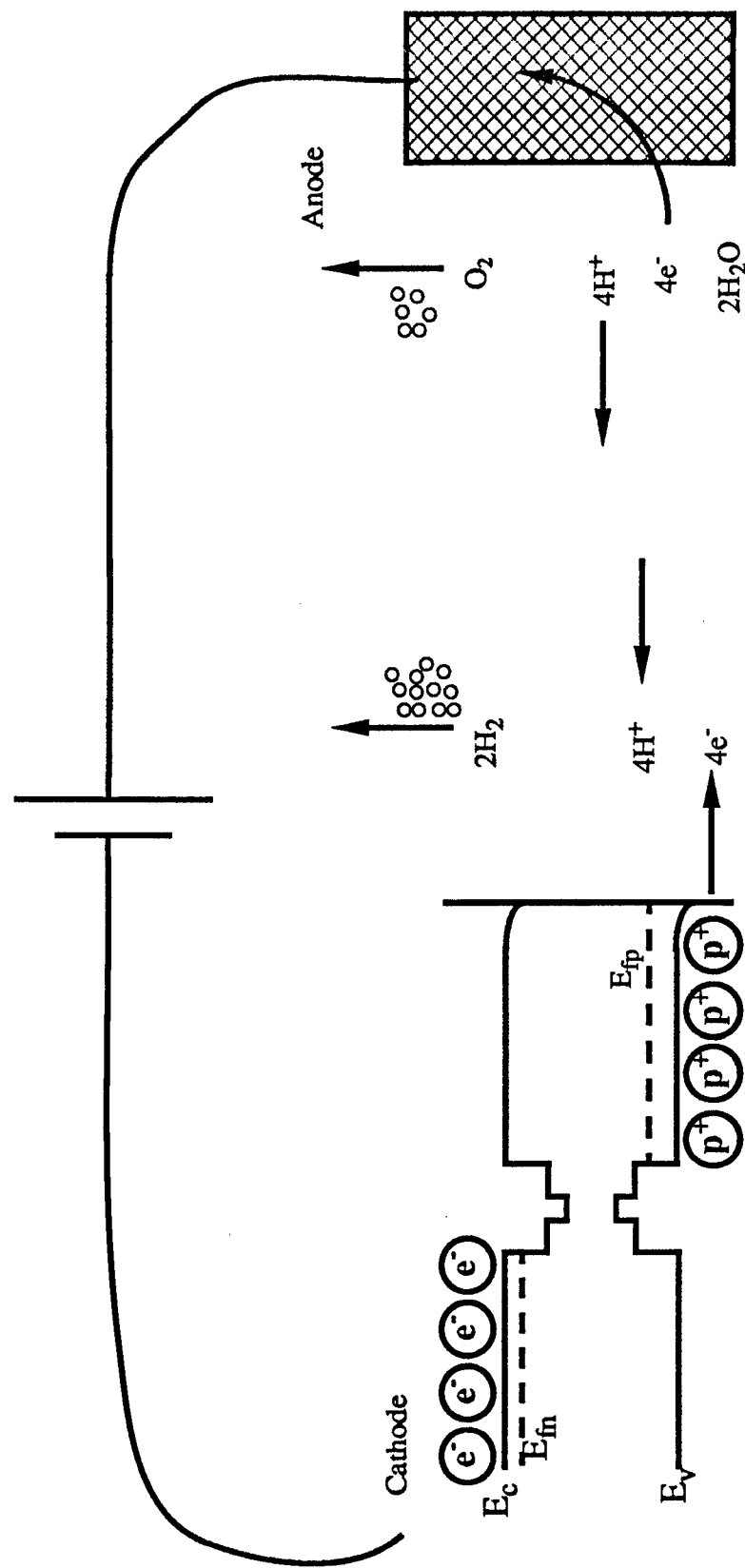
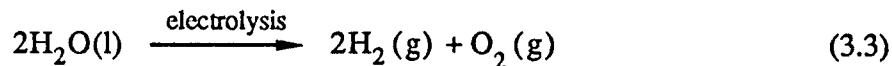


Figure 3-5. Band diagram for n/p/electrolyte under forward bias. Current flow mechanism results in the electrolysis of water.

The electrons which are produced at the anode/electrolyte interface move toward the power supply, where they complete the circuit. The production of hydrogen ions at the anode replaces those reduced at the cathode, bringing the system back to the original state except for the loss of two water molecules. The net chemical process can be described by adding Eq. 3.1 to Eq. 3.2 to obtain the electrolysis of water as shown in Eq. 3.3



3.3 LCL as a Lambertian Source

A Lambertian source has emission that is uniform across the surface area. For a Lambertian source of fixed area, the power measured relative to the surface normal decreases as $\cos(\theta)$. This reduction in power as the observer moves away from the normal is related to the decrease in the projected area of the source, which falls off as $\cos(\theta)$. Because the emission is uniform across most of the state-of-the-art epitaxial semiconductor laser material used in our experiments, we anticipated that LCL should be a Lambertian source. In this section, we describe the experiment we used to determine that LCL is, in fact, a Lambertian source.

Figure 3-6 shows a representative radiation pattern for a Lambertian source as a function of angle from the normal. This figure assumes that the source of emission is small (a point source) in relation to the measurement system, an assumption that was valid for our setup. The amplitude of the emission at a given angle is represented by the distance from the origin to the intersection of the circle and the angular line. Amplitudes are normalized to the amplitude of the light normal to the surface.

To determine the angular dependence of the emission and whether or not luminescence from the laser material was Lambertian, an LCL sample was held with clamping

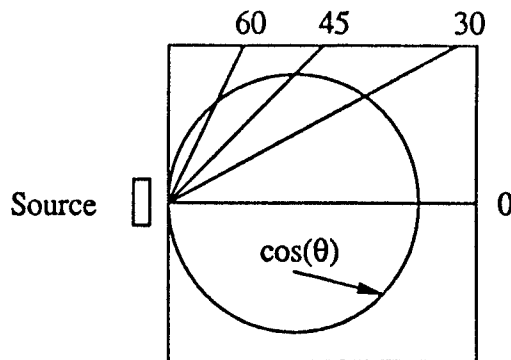


Figure 3-6. Radiation pattern for a Lambertian source, representative of the semiconductor laser wafers used in these experiments.

tweezers and partially submerged at the center of a beaker half filled with the GWA electrolyte. The grid was placed at the back of the beaker. An HP214B pulsed power supply was used to drive the sample in the LCL configuration (negative lead to the sample and positive lead to the grid). The sample was moved from the typical position near the edge of the beaker to the center to remove errors due to refraction at large angles from the normal. At the center, all of the light emitted from the sample at all angles was normal to the sides of the beaker and experienced no refraction. As mentioned before, the size of the sample (~1 cm in width) in relation to the size of the beaker (~10 cm in diameter) allowed us to consider the sample as a point source.

The beaker and sample were placed on a large piece of paper on which a polar grid had been constructed. The position of the sample was adjusted so that the surface of the sample was normal to the 0° markings on the polar grid. Placing the silicon p-i-n detector on the paper 20 cm from the sample, the power emitted during the LCL pulse was measured and recorded. The detector was moved in an arc centered on the circle and several sets of detector angle vs. power data were collected.

Figure 3-7 is a plot of the emitted power as a function of the emission angle. A curve corresponding to the cosine of the emission angle times the average of the values of the power at 0° ($\cos(\langle P(0^\circ) \rangle)$) is plotted along with the data. The angular emission data

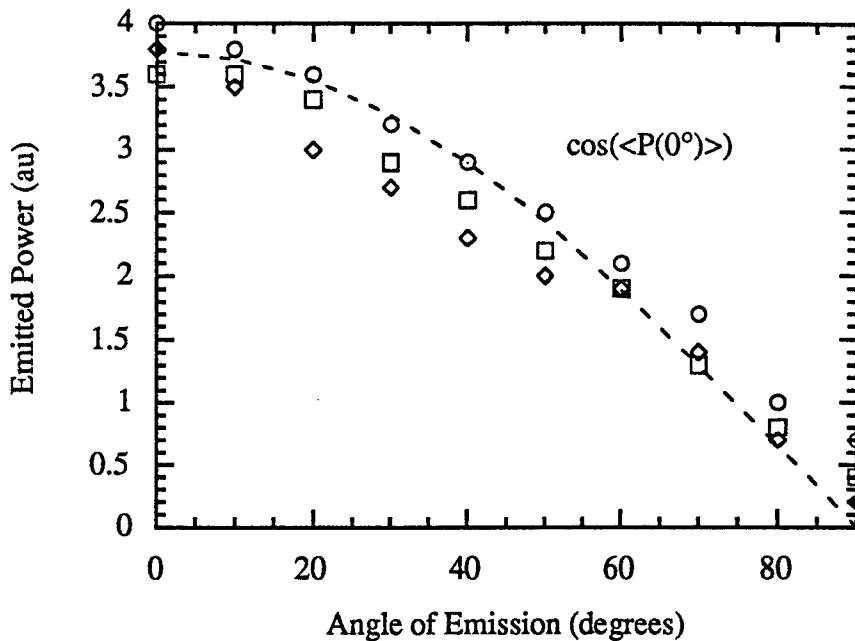


Figure 3-7. Emitted power during LCL as a function of the angle from the normal of the sample to the detector. Dashed line corresponds to $\cos(\langle \text{Int}(0^\circ) \rangle)$.

tracks with the cosine curve with larger than expected values at the highest angles. We believe that the additional light measured near 90° is due to scattering in the electrolyte and from the grid and beaker. Light generated in the sample was reflected off of the beaker and subsequently scattered off the grid, producing a background signal that was measured at and beyond 90° .

Based on the results of this experiment, we concluded that the LCL emission from laser wafers in LCL situations is a Lambertian source. This is typical of many LEDs and some materials used for display applications.

3.4 LCL during Substrate Anodization

Initial uses of PA were for formation of insulating layers on p-type epitaxial layers. PAL experiments followed these PA experiments and oxides were formed on the p-type layers during PAL. As shown in Figure 3.1 and Figure 3.2, LCL experiments with the negative contact to the n-type substrate resulted in forward biasing of the sample and light emission. In this section, we describe an experiment in which the semiconductor sample was forward biased, but with the positive contact to the p-type layers in an anodization setup. The sample was mounted on a cover glass slide and the p-type surface of the epitaxial wafer was contacted using aluminum foil and silver paint as shown in Figure 3-8. Leaving a window exposed on the n-type substrate of the wafer, the remainder of the wafer was electrically isolated using a masking material. In this manner, current flow was only allowed down the aluminum foil wire, through the semiconductor junction, and out the n-type substrate. Pulsed current was monitored through a $10\ \Omega$ resistor in the usual fashion and the optical power was measured using a PIN 10-D photodetector from Universal Detectors, Inc. Both of these parameters were monitored on an oscilloscope.

In many GaAs-based lasers, the wavelength of the light is strongly absorbed in the substrate material, which only allows for characterization of the emission from the p-type surface of the material. The reason for this is that the emission from a GaAs QW, which depends on QW width, will have a wavelength around 850 nm, which is strongly absorbed by the GaAs substrate. The semiconductor laser material used in this experiment utilized an InGaAs QW under strain, i.e. strained-layer InGaAs, producing emission at 950 nm, which is outside the absorption band of GaAs. In this way, any light emitted from the

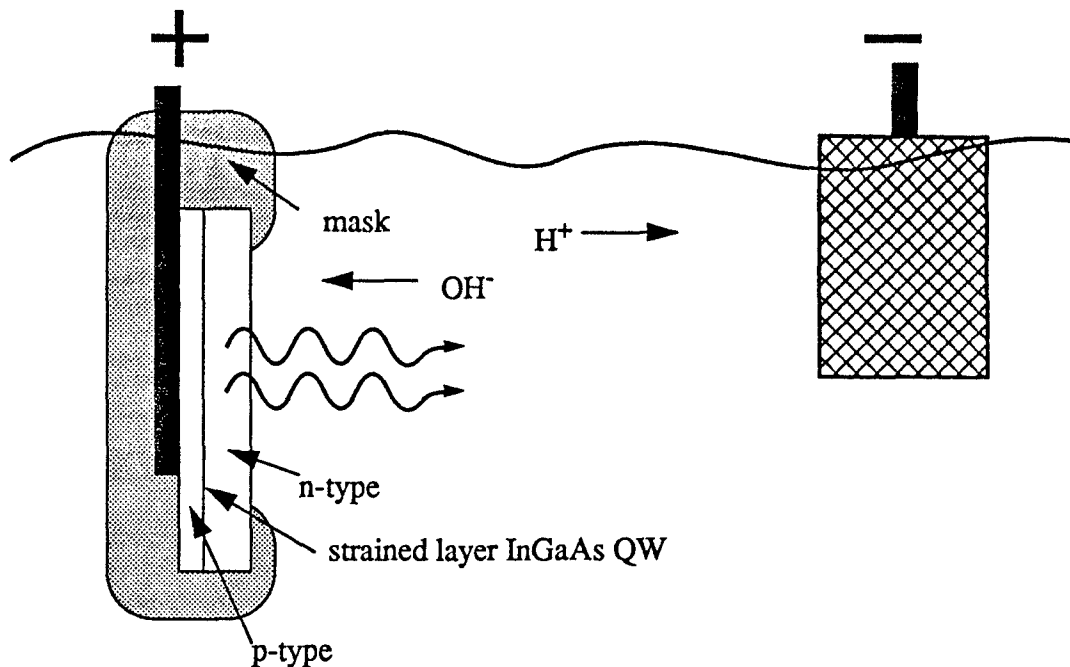
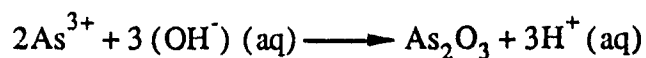
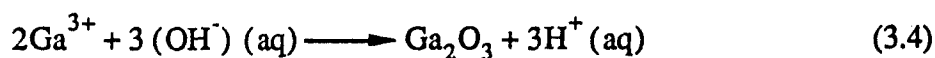


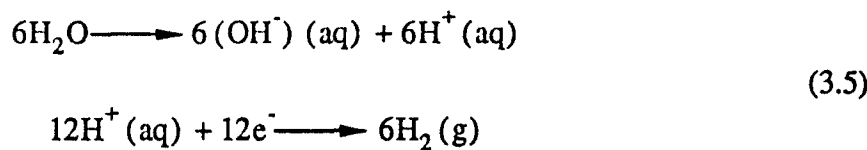
Figure 3-8. Experimental setup for LCL using p-contact. Both anodic oxidation and light emission were observed.

active region could pass through the GaAs substrate material without attenuation and be observed as it exited the n-type substrate.

In order to better understand the experimental results, it is instructive to predict the current flow mechanism for this contacting scheme. Because the contact scheme for this semiconductor laser wafer sample was anodic (the semiconductor was positive with respect to the electrolyte and grid), one would expect that the sample would become anodically oxidized. The reactions that produce oxidation at the anode are [Grov94]:



and the reactions that occur at the cathode are:



Combining these two sets of equations, the overall reaction for anodization is:



Therefore, we would expect that there will be charge transfer from the semiconductor sample resulting in oxidation of the GaAs as it reacts with the hydroxide ions in solution. At the cathode, water will dissociate into hydrogen and hydroxide ions. The hydrogen ions will extract electrons from the grid and hydrogen gas will be produced in the usual fashion.

During the anodization process, the p-n junction is forward biased as the positive lead is attached to the p-type material. Therefore, one would expect that initially, the forward bias current flow would generate emission from the active region. This was the motivation for using 950 nm material, so that if emission did occur, we could view it through the substrate.

When the circuit was connected to the pulse generator, both current flow and light generation were observed. Figure 3-9 presents oscilloscope traces of the current and optical power profiles as a function of time. In this figure, the current and light profiles are shown at two times, t_1 and t_2 , with $t_2 > t_1$, so that the development of the profiles with time can be presented. When voltage was applied to the circuit in the typical top-hat profile, the current pulse shape rapidly (on the order of 10 seconds) decayed to a profile similar in

shape to the one marked t_1 in the figure. Simultaneously, light was emitted from the substrate side of the sample. The onset of light emission coincided with the initial current flow in the circuit, behavior one would expect for a forward biased junction. Finally, bubbles were formed at the grid, in agreement with Eq. 3.5.

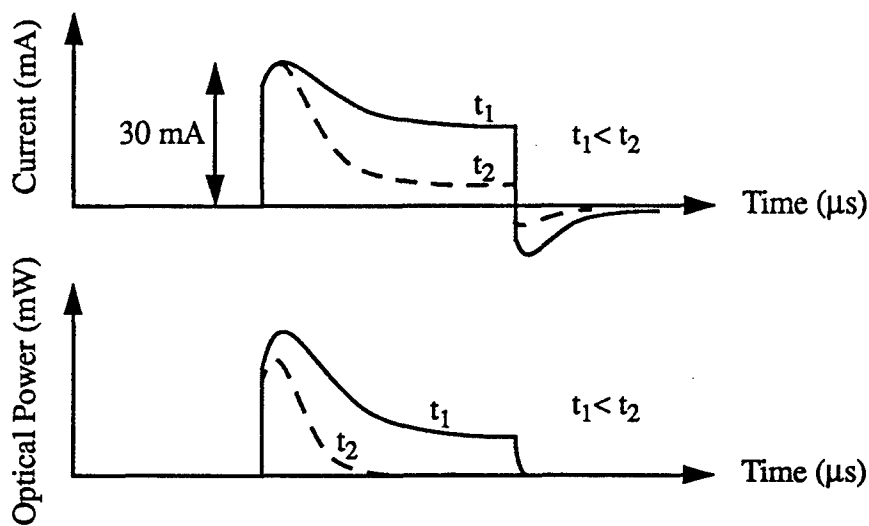


Figure 3-9. Current and optical power profiles for anodically biased LCL sample.

As the anodic current continued to flow, the oxide growth process continued to influence the current and light emission profiles. As the oxide layer thickened, the current profile decayed further as shown at time t_2 in Figure 3-9. Consistent with the decreased current flow, the emitted power dropped off as well.

After several minutes, the current flow was reduced to a profile typically associated with anodic oxidation. Because the oxidation of GaAs materials travels into the semiconductor material, we expected the current flow associated with the growth and dissolution of the oxide layer to produce a uniform emission pattern across the exposed portion of the substrate. Instead, the light emission pattern, when viewed with an infrared viewer, was found to be quite non-uniform with the light generated from bright pin-points

on the substrate. We do not currently have an explanation for the non-uniform emission observed during this experiment.

Although we do not currently have an explanation for this unusual emission pattern, it may prove useful to investigate this phenomenon further. It is possible that the light emission pattern may enable us to improve our understanding of the oxide growth process. Specifically, the lateral character of the oxide growth and dissolution may be measurable using this technique. We believe that oxide growth starts at the edges of the wafer and progresses into the center. Verification of this lateral growth characteristic may be possible by using this technique and ultimately lead to the optimization of the lateral growth characteristics.

3.5 Applications of LCL

LCL has applications that can be classified into two broad categories: diagnostics and displays. In the next two chapters, both of these applications are discussed and experiments are used to quantify and improve the LCL process. As a diagnostic tool, LCL can provide a variety of useful information about the quality of the epitaxial wafer prior to laser fabrication. Temporal stability of the light emission and injection efficiency measurements are discussed in Chapter 4. The luminescent properties of LCL naturally lead to applications for light emitting displays. A key requirement for displays is to reduce or eliminate the hydrogen bubbles generated at the semiconductor surface so an improved electrolytic solution has been developed and is presented in Chapter 5.

CHAPTER 4

LIQUID CONTACT LUMINESCENCE - DIAGNOSTIC

LCL has been proven useful as a semiconductor laser wafer characterization technique. As a diagnostic tool, LCL can provide much useful information about the quality of the epitaxial laser wafer prior to laser fabrication. It is a quick, inexpensive, and non-destructive process that measures a variety of material parameters. Comparison of relative light emission capabilities at a given input current can be used to provide wafer to wafer characterization information. The peak emission wavelength, spectral linewidth, and wafer uniformity map of a sample can be determined. In this chapter, some of the diagnostic techniques developed using LCL will be described along with data obtained by this method. The first subject covered is the decay of light emission observed in some LCL experiments. The explanation for this decay phenomenon and a sample contacting scheme which prevents emission decay is described. The application of LCL to the measurement of relative internal quantum efficiency is discussed. A theoretical model is proposed for LCL at both low and high injection levels. Experimental data is used to verify the model and demonstrate that the relative internal quantum efficiency can be measured at high injection levels. Finally, the design of a sample holder employed to obtain repeatable LCL measurements is described.

4.1 Luminescence Temporal Stability (LTS) Problem

During LCL testing of wafer samples, it was observed that in some cases, the luminescence produced by the semiconductor laser wafer would diminish as a function of time.

If LCL is to be used as a semiconductor laser wafer diagnostic technique, then it is important that the luminescence from a sample is either not a function of time or varies slowly with time in comparison to the time required to perform the wafer characterization. In order to relate the optical emission to the drive current or voltage, the light emission needs to be constant throughout the measurement process. To determine whether or not the luminous efficiency was a function of time, several experiments were performed.

Standard Contact and GWA Electrolyte

For the first experiment, a wafer sample was placed in the standard LCL beaker setup as described in Chapter 3. The sample was contacted as shown in Figure 4-1.

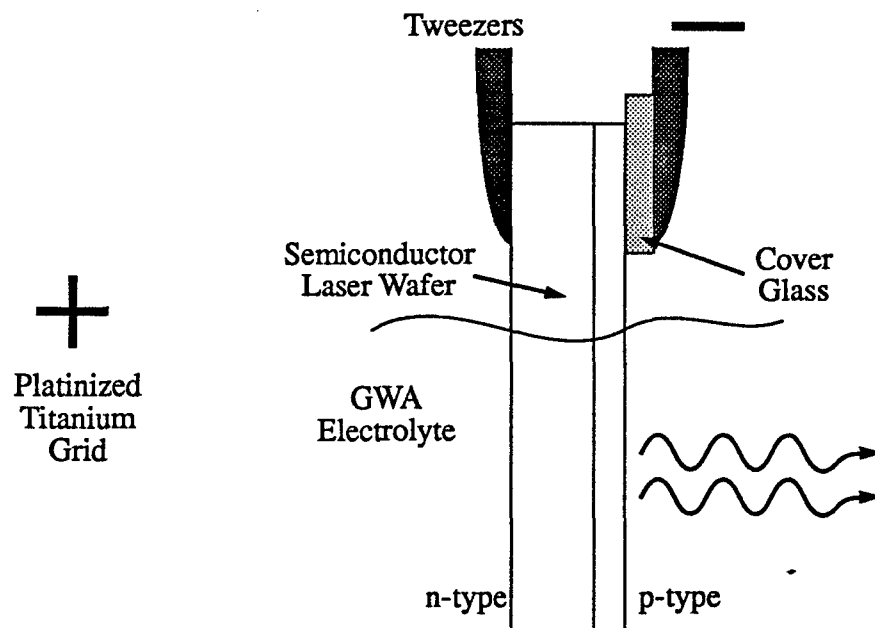


Figure 4-1. Side view of the standard contact scheme for LCL testing of sample in a beaker. Contact is made to the n-type side of the wafer while the p-type side is insulated by the cover glass. The sample is exposed to the GWA electrolyte on both the n-type and p-type sides.

Using this contact scheme, current can flow through either the p-side or the n-side of the wafer. Current does, in fact, take both of these paths and hydrogen bubbles are observed both on the front and back of the semiconductor sample. A plot of the light

emission intensity, represented by the integrated spectral counts measured on the OMA along with the current flowing in the LCL circuit as a function of time are shown in Figure 4-2. In this figure, there are three data points for each measurement time. The integrated spectral count and the current were measured and remeasured two additional times in order to obtain an averaged value. In some cases, the consecutive measurements were identical, which produced less than three data points for a given time.

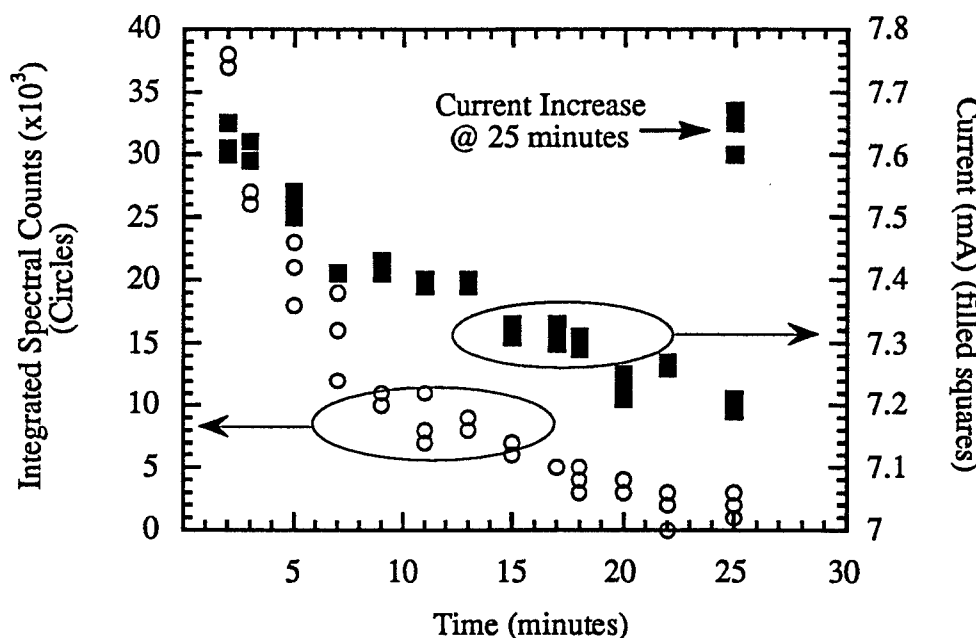


Figure 4-2. Light emission decay as a function of LCL time. The sample is exposed to the GWA electrolyte on both the n-type and p-type sides.

Both the integrated spectral counts and the current dropped during the 25 minutes that data was collected. In order to determine if this decrease in current by less than 10% resulted in the decrease in light emission, the voltage of the cw power supply was increased at 25 minutes (16 V to 16.4 V) to increase the current back to the original 7.7 mA that was flowing in the circuit at the beginning of the test. The light emission intensity

from the sample did not increase, but stayed near zero. Therefore, the light emission intensity does, in fact, decrease to zero as a function of time in this contact scheme using a GWA electrolyte.

The sample was removed from the GWA electrolyte, cleaned using deionized water, and dried with N₂. When the cleaned sample was placed back in the LCL beaker in the configuration shown in Figure 4-1, the light emission intensity returned to the values found at the beginning of the plot shown in Figure 4-2. Therefore, we believe that a thin film forms on the surface of the semiconductor sample that impedes current flow through the p-side of the sample. As the current flow through the p-type material decreases, the current flowing through the junction and the light emission intensity decrease as well. The current path through the n-type material to the cathode continues to carry current and, by the 25 minute point (when the emission equals zero), all of the current is flowing through the n-type material.

Standard Contact and EDTA Electrolyte

For comparison, this experiment was repeated using 0.25 M ethylenediamine tetraacetic acid (EDTA) as an electrolyte. EDTA is used as an electrolyte in capacitance-voltage profilometers for semiconductor material characterization. The experiment was performed as it was with the GWA electrolyte but with the current kept constant at 100 mA.

The plot of integrated spectral counts vs. time is presented in Figure 4-3. As one can see, the light emission intensity does decay slightly over the 30 minute duration of this test. This slight decrease in light emission led us to believe that the standard contact

scheme is not a suitable method if the goal of uniform emission as a function of time is to be obtained.

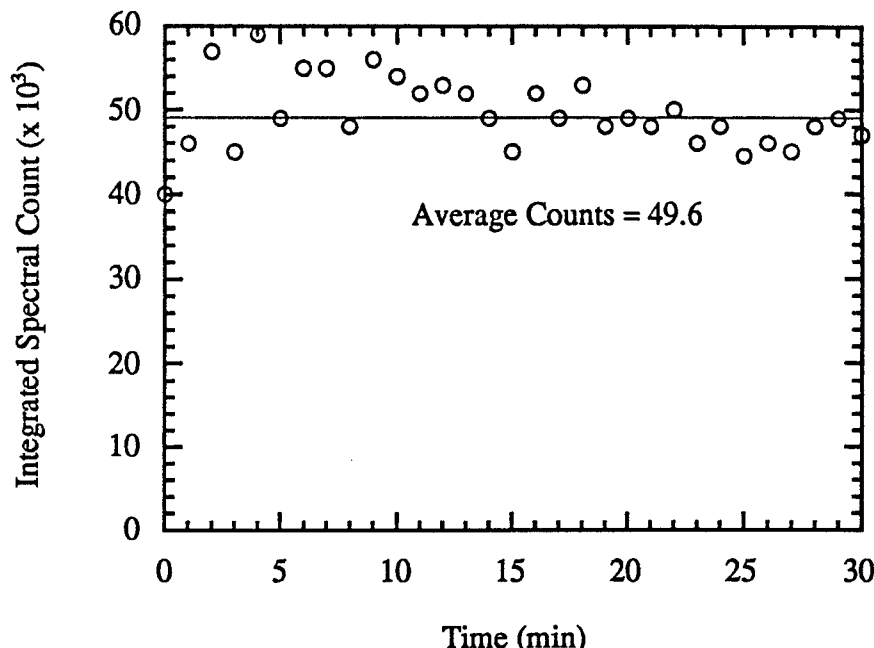


Figure 4-3. Light emission decay as a function of LCL time. The sample is exposed to the EDTA electrolyte on both the n-type and p-type sides.

Insulated Contact and GWA Electrolyte

One possible solution to this problem of light emission decay is to coat the sides and back of the wafer using a suitable mask. Historically, photoresist has been used as a current blocking mask for pulsed anodization and gold plating of laser material. However, we found that photoresist is slowly dissolved in the GWA electrolyte. Therefore, although photolithography can be used to fabricate a well defined opening on the p-side of a laser wafer, over time it will be dissolved and a current path will be opened to the n-side of the wafer. The end result would be similar to that obtained with the n-side of the wafer exposed to the electrolyte.

Therefore, we have required another current blocking mask that would act as a good current blocking layer and yet be easily removed after LCL testing so that the testing process is non-destructive. We found that nail polish meets these requirements because it has good current blocking characteristics and is easily dissolved in acetone. One benefit that photoresist provides is the ability to define precise areas on the p-side of the wafer. Using nail polish, this precise area definition is difficult. To make contact to the n-side of the wafer, aluminum foil and silver paint were used. The wafer was mounted on a glass slide and the sides of the wafer and the exposed portion of the aluminum foil lead were covered with additional nail polish as shown in Figure 4-1. Although the exact areas used for these lifetime experiments could not be identical, as explained above, the sample areas exposed to the electrolyte were comparable at $\sim 0.5 \text{ cm}^2$.

Using this insulated contact scheme, the sample was operated to produce LCL. As before, several current and light emission samples were collected at each measurement time. The data collected using this contact scheme is presented in Figure 4-5.

As one can observe, the light emission experienced no decay after 30 minutes of LCL operation, reinforcing our belief that the decay is related to the opening or enhancement of a current flow path through the n-side of the wafer. The use of an appropriate current blocking mask and insulation of the n-side of the wafer can prevent the light emission decay from occurring. It should also be noted that the total number of integrated spectral counts is much greater for the case in which the n-side of the sample was insulated from the liquid electrolyte. This increase in emission was obtained while the current flowing in the LCL circuit was reduced in the insulated case.

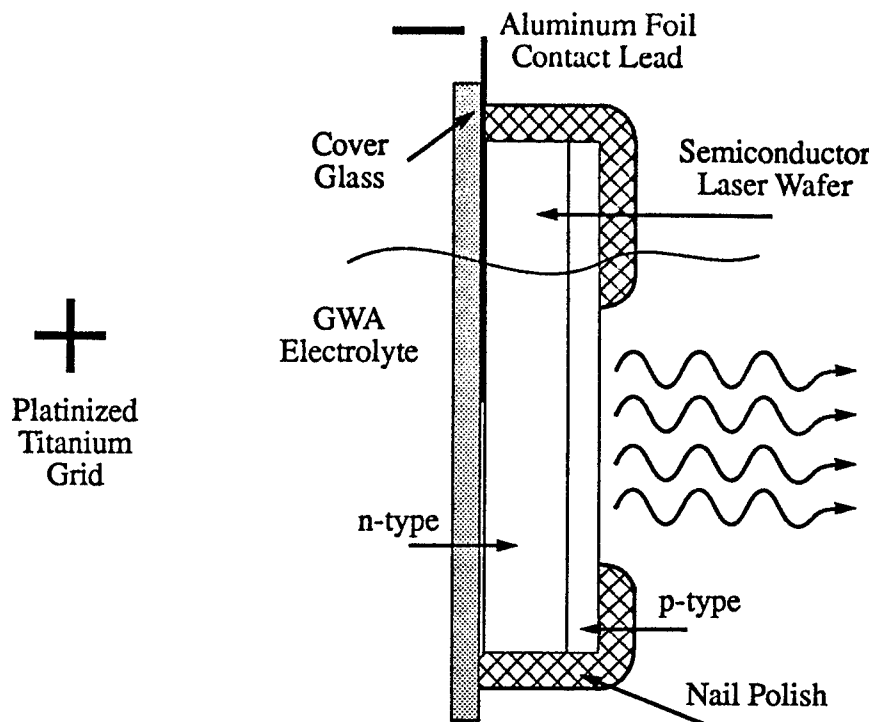


Figure 4-4. Side view of the insulated contact scheme for LCL testing of sample in a beaker. Contact is made to the n-type side of the wafer through the aluminum foil lead, which is insulated, along with the n-type material, from the GWA electrolyte.

Although prevention of the emission decay was obtained by using the insulated contact scheme shown in Figure 4-1, there were several problems inherent in the design which required solutions. First and foremost, the lack of the ability to precisely define an area on the p-type surface of the wafer through which the LCL current was injected created problems in calculating the current density flowing through the wafer. Because the current density flowing through a device allows for easy comparison between devices of different area, obtaining this number is quite important. Additionally, the time required to prepare an insulated sample holder is a drawback. Application of the aluminum foil contact and repeated applications of nail polish are obviously not an ideal solution to the LCL

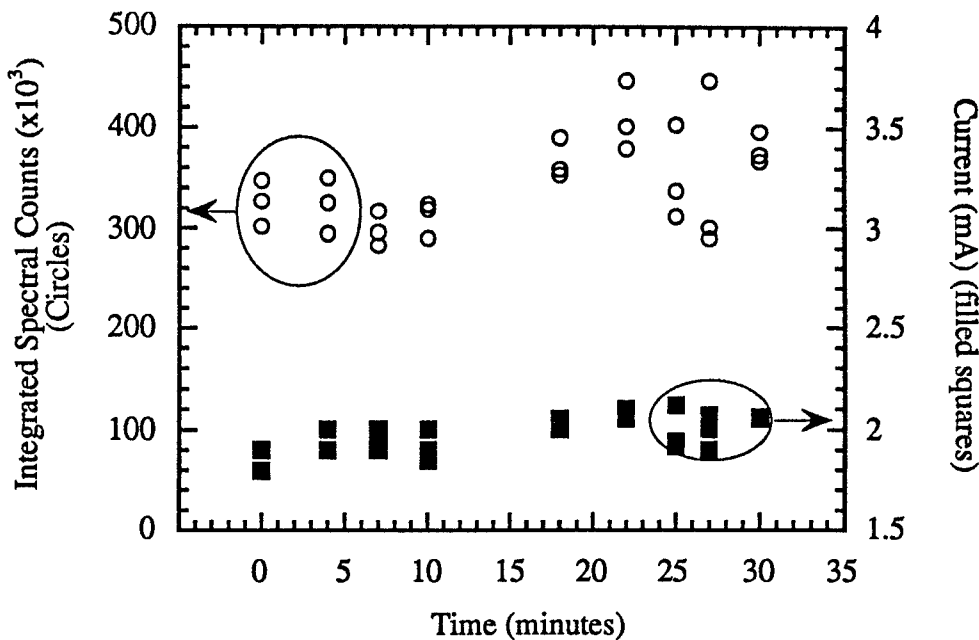


Figure 4-5. Light emission decay as a function of LCL time. The sample is insulated from the GWA electrolyte except for a portion of the p-type surface.

testing problem. Therefore, a new sample holder was required for these LCL experiments. Section 4.3 describes the requirements for, and the design and fabrication of this new sample holder.

A future experiment that would shed light on the increased current flow through the n-side of the wafer would be to illuminate the p-side with short wavelength light during LCL in order to generate electron-hole pairs. With additional conduction band electrons created in the p-type material in this manner, the electron transfer mechanism for the p-type and n-type material to the hydrogen ion would be comparable. The impact of illumination on the LTS problem and the electron transfer mechanism at the semiconductor electrode-liquid electrolyte interface might be studied in this way.

4.2 Relative Internal Quantum Efficiency Measurements

The parameter η_i , usually called internal quantum efficiency, is one of the key parameters used to quantify the performance of semiconductor lasers. The conventional method for determining η_i involves the fabrication and pulse-testing of at least three sets of wide-stripe lasers with different cavity lengths. From the measured slope efficiencies (η_s), one then extracts η_i .

Assuming the output power vs. current (P_o - I) curve of a diode laser is linear, one can define a slope efficiency η_s :

$$\eta_s = \frac{P_o}{(I - I_{th})} = \left(\frac{P_o / (hv)}{(I - I_{th}) / e} \right) \left(\frac{hv}{e} \right) = (\eta_d) (V_c) \quad (4.1)$$

In this equation, the parameter η_d is called the differential quantum efficiency and the parameter V_c is the characteristic voltage. The parameter η_d can be broken into two parts as indicated below:

$$\eta_d = \eta_i \eta_o \quad (4.2)$$

where η_i is the internal quantum efficiency and η_o is the output efficiency. The expression for η_o is:

$$\eta_o = \frac{\frac{1}{2L} \ln \frac{1}{R_o}}{\alpha_i + \frac{1}{2L} \ln \frac{1}{R_o R_b}} \quad (4.3)$$

where α_i is the internal mode loss, L is the laser cavity length, and R_o and R_b are the mode power reflectivities of the facets ($R_o=R_b$ in our experiment).

From the above three equations, one can obtain an expression for η_s ,

$$\frac{1}{\eta_s} = \left(\frac{2}{V_c \ln \frac{1}{R_o}} \left(\frac{\alpha_i}{\eta_i} \right) \right) L + \frac{1}{\eta_i V_c} \left(1 + \frac{\ln \frac{1}{R_b}}{\ln \frac{1}{R_o}} \right) \quad (4.4)$$

The parameter η_i can be determined from the intercept of a plot of $1/\eta_s$ vs. L.

$$\eta_i = \frac{1}{V_c(1/\eta_s)_{L=0}} \left(1 + \frac{\ln \frac{1}{R_b}}{\ln \frac{1}{R_o}} \right) \quad (4.5)$$

Since this determination of η_i involves a substantial amount of work and uses up laser material, it is interesting to ask if there is some simple, nondestructive method which can be used at the unprocessed wafer level to predict the η_i value for the wafer. In this section we report on the use of LCL to address this question and show that LCL can be utilized to predict the relative η_i for a laser wafer.

As will be seen, although the LCL technique used here is somewhat similar to the well-known photoluminescence (PL) technique routinely used to evaluate diode laser material, it is intrinsically superior to PL in that the current density J is easily measured. Since the performance of diode lasers is determined in large part by the dependence of light emission on J , the ability to easily measure J is a very important part of the evaluation process. In PL experiments, it is very difficult to estimate the effective J since it depends on the wavelength of the pump source, the reflectivity, absorption and transmission characteristics of the material at that wavelength, and the nature of the minority carrier transport processes in the material. With LCL, this problem is avoided since the liquid contact acts like a metal contact in providing majority carrier injection to pump the material.

In general, QW electron-hole recombination processes can be subdivided into non-radiative (R_{nr}), spontaneous (R_{sp}), and stimulated (R_{st}) [Cold95]. These three types of recombination mechanism are related by the following equation:

$$\eta_i \frac{I}{e} = R_{nr} + R_{sp} + R_{st} \quad (4.6)$$

The physical meaning of this equation is that a given number of carriers per second ($\frac{I}{e}$) are injected with some efficiency (η_i) into the active region, resulting in a certain number of recombinations per second via various mechanisms. For these LCL experiments, Eq. 4.6 and the corresponding physical phenomenon are considered at injection levels for which no stimulated emission events are considered (operation well below lasing threshold). Therefore, only spontaneous and non-radiative recombination events will be considered.

The recombination rates for non-radiative and spontaneous emission can be related to the carrier density as follows:

$$\begin{aligned} R_{nr} &= AN \cdot V && \text{Non-radiative recombination rate} \\ R_{sp} &= BN^2 \cdot V && \text{Spontaneous emission recombination rate,} \end{aligned} \quad (4.7)$$

where A and B are the non-radiative and spontaneous emission recombination coefficients, respectively, N is the carrier density in the active region, and V is the volume of the active region. Neglecting the stimulated emission term, substituting these relations into Eq. 4.6, and dividing both sides by the volume ($V = wld$), one obtains a relationship between the current density, J , and the carrier density, N :

$$\eta_i \frac{J}{ed} = AN + BN^2. \quad (4.8)$$

Using the substitution

$$j = \frac{J}{ed} \quad (4.9)$$

Eq. 4.8 can be rewritten as:

$$BN^2 + AN - \eta_i j = 0 \quad (4.10)$$

Using the quadratic equation to solve for N , one obtains

$$N = \frac{1}{2} \left[-\frac{A}{B} \pm \sqrt{\left(\frac{A}{B}\right)^2 + 4\left(\frac{\eta_i}{B}\right)} \right] \quad (4.11)$$

Examining only the solution for $N > 0$,

$$\begin{aligned} N &= \frac{1}{2} \left[\sqrt{\left(\frac{A}{B}\right)^2 + 4\left(\frac{\eta_i}{B}\right)} - \frac{A}{B} \right] \\ &= \frac{1}{2} \left(\frac{A}{B} \right) \left[\sqrt{1 + 4\left(\frac{B}{A}\right)^2 \left(\frac{\eta_i}{B}\right)} - 1 \right] \\ &= \frac{1}{2} \left(\frac{A}{B} \right) \left[\sqrt{1 + 4\left(\frac{B}{A^2}\right) \eta_i} - 1 \right] \end{aligned} \quad (4.12)$$

For low current injection levels (low β), the binomial expansion can be used to expand the term inside the square root

$$\begin{aligned} (1+x)^p &\approx 1+px \\ \therefore \sqrt{1+4\left(\frac{B}{A^2}\right)\eta_i} &\approx 1+2\left(\frac{B}{A^2}\right)\eta_i \end{aligned} \quad (4.13)$$

to obtain the following approximation for N at low current levels:

$$N \approx \frac{\eta_i \beta}{A} \quad (4.14)$$

Since only the spontaneous emission recombination events result in light emission, the optical power emitted during LCL is proportional to BN^2 . Using either Eq. 4.12 for the general case or the approximation found in Eq. 4.14 for the low current level case, the relationship between the emitted power and the injection current can be found.

For the general case:

$$\begin{aligned} P &= KBN^2 \\ &= KB \left[\frac{1}{2} \left(\frac{A}{B} \right) \left(\sqrt{1 + 4\left(\frac{B}{A^2}\right) \eta_i} - 1 \right) \right]^2 \\ &= \frac{KA^2}{4B} \left[1 + 4\left(\frac{B}{A^2}\right) \eta_i \beta + 1 - 2\sqrt{1 + 4\left(\frac{B}{A^2}\right) \eta_i} \right]^2 \\ \therefore P &= \frac{KA^2}{2B} \left[1 - \sqrt{1 + 4\left(\frac{B}{A^2}\right) \eta_i} + 2\left(\frac{B}{A^2}\right) \eta_i \beta \right]^2 \end{aligned} \quad (4.15)$$

For the case of low level injection, the approximation for N found in Eq. 4.14 can be used to find the relationship between emitted power and the injection current:

$$\begin{aligned} P &= KBN^2 \\ &\approx K \frac{B}{A^2} \eta_i^2 j^2 \end{aligned} \quad (4.16)$$

Therefore, for low injection levels (assuming that η_i is constant), the emitted power is proportional to the square of the current density:

$$P \propto J^2 \quad (4.17)$$

Using a visible laser wafer (X847), power vs. current data was collected using the LCLSH described in section 4.3. Data was collected at both low and high current levels to verify the theoretical model proposed above.

Low Level Injection

Figure 4-6 is a plot of the measured LCL spectra obtained from wafer X847 at current levels that varied from 0.2 to 2 mA. The scan time of the optical multichannel analyzer was 20 ms. Since the size of the emitting area was 0.125 cm^2 , the current density ranged from 1.6 to 16 mA/cm^2 .

Examining the LCL for this wafer, the spectrum of the emission does not shift with drive current and asymmetries are preserved as drive current increases. In order to obtain the emitted power from these spectral measurements and compare the experimental power vs. current data with theory, these spectral profiles were integrated. The total photon count N_{ph} for a given J is obtained by adding up the total number of counts under the spectral envelope and subtracting the number of counts outside the spectral window in which the emission is contained. For example, for wafer X847, the spectral window of emission is

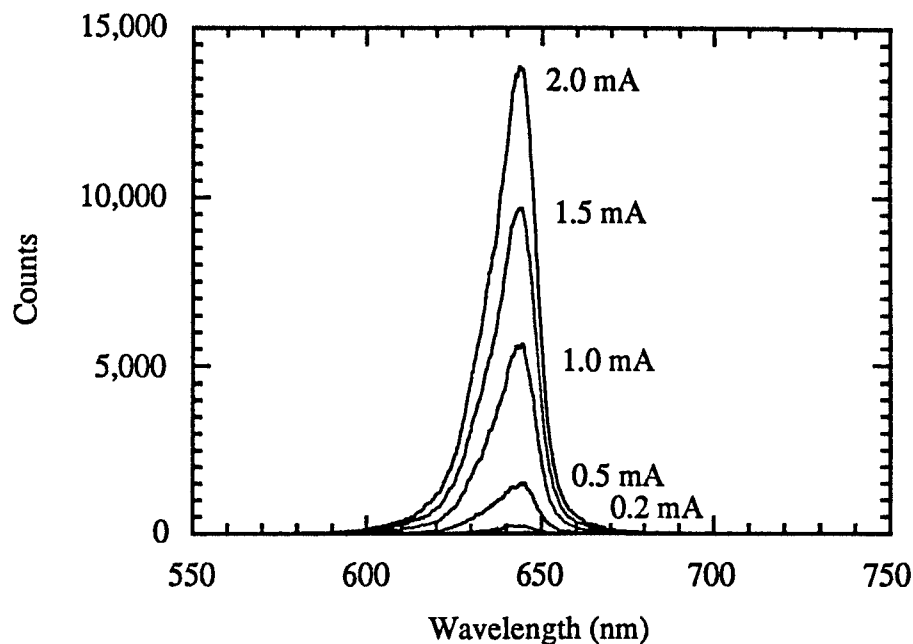


Figure 4-6. Spectral data for wafer X847 from 0.2 mA to 2 mA. Sample size is 0.125 cm^2 .

600 to 680 nm. N_{ph} vs. J for wafer X847 is plotted in Figure 4-7. In this figure, the N_{ph} data points for the wafer is represented by circles.

Examining this plot, one can see that the relationship between the power and the low level injection current density is obviously not linear. In order to determine if the power is proportional to the square of the current density as derived in Eq. 4.17, it is necessary to determine the values for the A and B coefficients used in Eq. 4.16.

The power measured by a detector is equal to the total emitted power (the spontaneous emission power) minus the power required for the detector to register a signal above the noise floor. We refer to this last power value as the threshold power, P_{th} . Using these parameters, the detected power can be represented by

$$\begin{aligned} P_{det} &= P_{sp} + P_{th} \\ &= KBN^2 + P_{th}, \end{aligned} \tag{4.18}$$

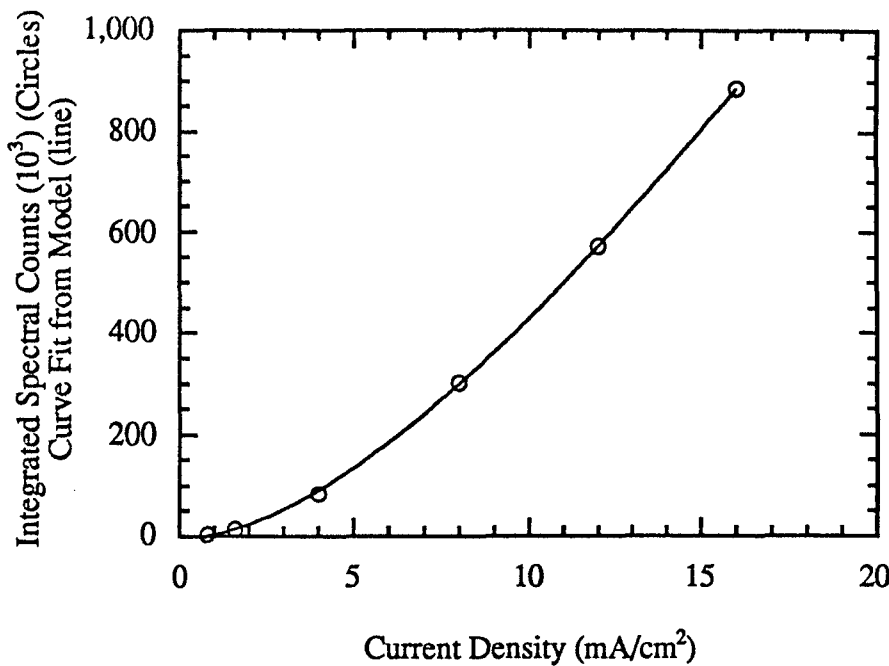


Figure 4-7. Integrated spectral counts N_{ph} vs. J for wafer X847. Circles represent experimental data and line represents curve fit derived from a theoretical model with $J_{th} = 0.7 \text{ mA/cm}^2$ and $x = 0.2$.

where the spontaneous emission collection efficiency has been included as K .

Considering the point where the detector threshold is reached, the detected power, P_{det} , will be zero and the current density, J , will be J_{th} . For this condition, Eq. 4.18 can be solved for P_{th} , using Eq. 4.12 for the value of N to obtain

$$P_{th} = K \frac{A^2}{4B} \left[\sqrt{1 + \frac{4B\eta_i}{A^2 ed} J_{th}} - 1 \right]^2 \quad (4.19)$$

Using Eq. 4.18, the detected power can be found.

$$P_{det} = K \frac{A^2}{4B} \left[\left\{ \sqrt{1 + \frac{4B\eta_i}{A^2 ed} J} - 1 \right\}^2 - \left\{ \sqrt{1 + \frac{4B\eta_i}{A^2 ed} J_{th}} - 1 \right\}^2 \right] \quad (4.20)$$

$$P_{det} = K \frac{A^2}{4B} \left[\frac{4B\eta_i}{A^2 ed} (J - J_{th}) - 2 \left\{ \sqrt{1 + \frac{4B\eta_i}{A^2 ed} J} - \sqrt{1 + \frac{4B\eta_i}{A^2 ed} J_{th}} \right\} \right] \quad (4.21)$$

$$P_{det} = K \frac{\eta_i}{ed} \left[(J - J_{th}) - \frac{A^2 ed}{2B \eta_i} \left\{ \sqrt{1 + \frac{4B \eta_i}{A^2 ed} J} - \sqrt{1 + \frac{4B \eta_i}{A^2 ed} J_{th}} \right\} \right] \quad (4.22)$$

P_{det} can be rewritten in a simplified form if a substitution is made for

$$\frac{4B \eta_i}{A^2 ed} \equiv x. \quad (4.23)$$

$$P_{det} = K \frac{\eta_i}{ed} \left[(J - J_{th}) - \frac{2}{x} \{ \sqrt{1 + xJ} - \sqrt{1 + xJ_{th}} \} \right] \quad (4.24)$$

Using this equation for P_{det} , relations for P_1 and P_2 can be calculated for two different current densities, J_1 and J_2 . These two relations for P_1 and P_2 can be divided into each other and one can numerically solve for the x value for each (J_1, P_1) and (J_2, P_2) pair as shown in Eq. 4.25.

$$\frac{P_1}{P_2} = \frac{(J_1 - J_{th}) - \frac{2}{x} \{ \sqrt{1 + xJ_1} - \sqrt{1 + xJ_{th}} \}}{(J_2 - J_{th}) - \frac{2}{x} \{ \sqrt{1 + xJ_2} - \sqrt{1 + xJ_{th}} \}} \quad (4.25)$$

The values determined for x for each wafer were averaged ($\bar{x} = 0.2$) and plugged back into Eq. 4.24 to obtain P_{det} in terms of J . This curve was normalized to match the experimental power valued at the highest current density and is plotted with the experimental data in Figure 4-7. The data obtained using wafer X847, which was a high quality laser wafer, was fit by the model extremely well.

High Level Injection

Having discussed the theory and experiments at low current levels, the remainder of this section is devoted to a discussion of the relationship between power and current density at high injection levels. In high quality red laser material, one expects that $R_{sp} \gg R_{nr}$ and R_{st} at current densities of a few A/cm². In this case, Eq. 4.6 simplifies to:

$$\eta_i \frac{I}{e} \approx R_{sp} \quad (4.26)$$

If current is run for time Δt , the number of photons generated will be $R_{sp}\Delta t$. However, only a fraction (F) of these photons will be collected by the spectrometer. Defining this photon number as N_{ph} , we can write,

$$N_{ph} = R_{sp}\Delta t F = \frac{F\Delta t}{e}\eta_i I = K\eta_i I \quad (4.27)$$

where $K = \frac{F\Delta t}{e}$ is a constant. If η_i is independent of I and the assumptions made to obtain Eq. 4.26 are correct, then a plot of N_{ph} vs. I will be linear. If so, then the ratio of the slopes for two wafers will be equal to the ratio of their internal quantum efficiencies.

In order to verify that the emitted power is linear with drive current, the wafer used earlier was driven at higher current densities. Figure 4-8 is a plot of the integrated spectral counts as a function of drive current. As one can observe from the plot, the emitted power becomes linear with drive current at currents over 2 mA (16 mA/cm²), as predicted. Sample size, as before, was 0.125 cm².

For additional information about internal quantum efficiency measurements of GaInP quantum well laser material using LCL, the reader is referred to a paper recently presented by another student in our research group [Hsu96]. In this work, LCL at high injection levels was used to measure the ratio of internal quantum efficiencies for two red laser wafers with identical epitaxial structures except for differences in the thickness of the QW active region (7 or 8 nm). It was found that the measured ratio was in agreement with the internal quantum efficiency ratio as determined from conventional slope efficiency vs. cavity length measurements. In conclusion, the LCL method is a good way to predict relative η_i values for diode laser wafers.

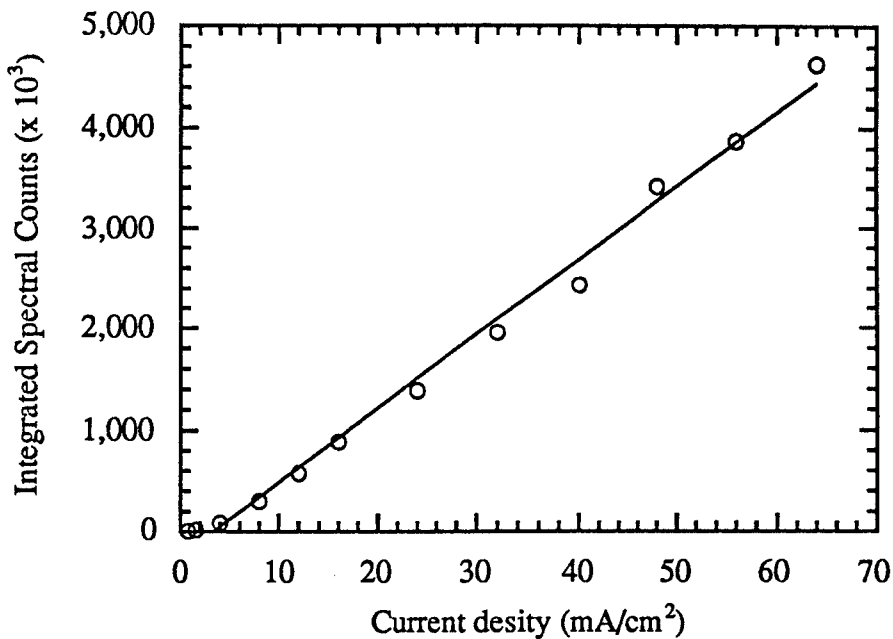


Figure 4-8. Integrated spectral count vs. current density for wafer X847. Emitted power is linear with current at high injection levels. Line is a linear curve fit to data.

4.3 LCL Sample Holder

In order to perform luminescence experiments in a repeatable fashion, we needed a sample holder that would meet several requirements. The sample holder should provide a way for the samples being tested to be exchanged in and out of the sample holder in an easy manner. It should precisely position the sample in the same location in front of the measurement equipment each time it is used. This precise placement will allow for consistent coupling to the measurement devices, such as the optical multichannel analyzer (OMA). Also, the sample holder should have a precise area of the semiconductor sample in contact with the electrolyte each time, so that a given current level always results in the same current density, a parameter upon which many semiconductor properties depend in a functional manner. Because some of the redox couples used in LCL experiments become

colored liquids upon dissolution, the distance between the front of the semiconductor sample and the emission window should be small. Finally, the sample holder should not interact with the liquid electrolyte or the sample in a manner which would impact the testing.

Based on these requirements, we designed and built a spring loaded sample holder, which we have simply named the liquid contact luminescence sample holder (LCLSH), as shown in Figure 4-9 and Figure 4-10.

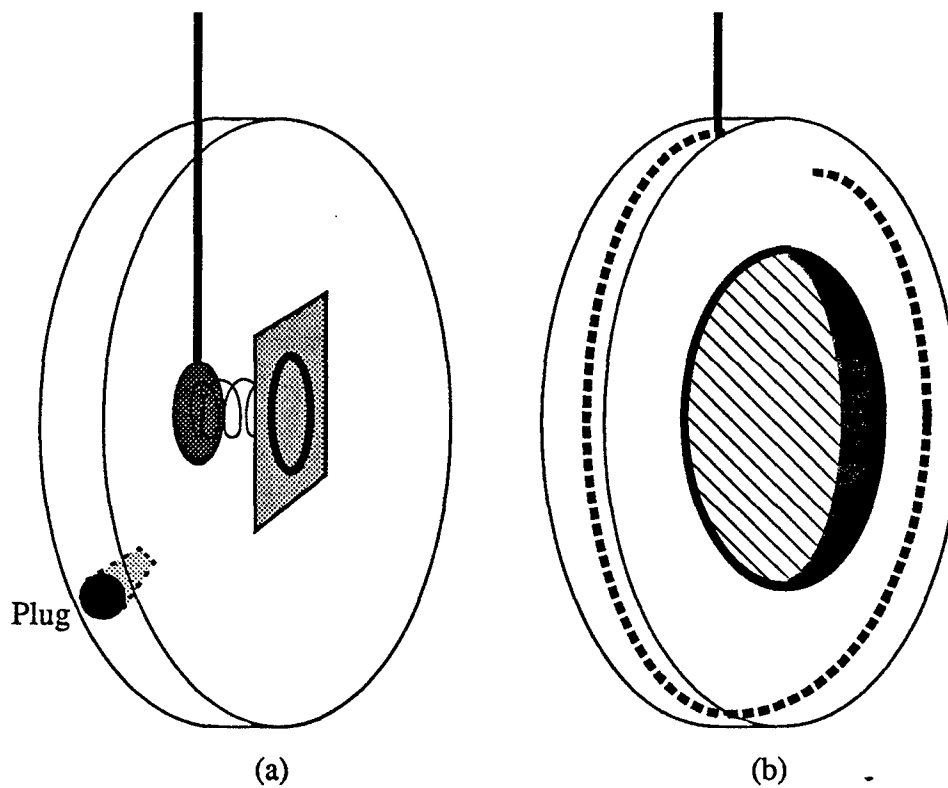


Figure 4-9. Perspective drawing of the LCL sample holder (LCLSH). Pieces (a) and (b) are bonded together for final assembly.

The LCLSH pictured in Figure 4-9 and Figure 4-10 was designed and constructed using two plastic petri dishes. The design can best be understood by separately examining the left and right portions (Figure 4-9(a) and (b)) of the dish, which correspond to the cathode and anode of the electrochemical cell, respectively.

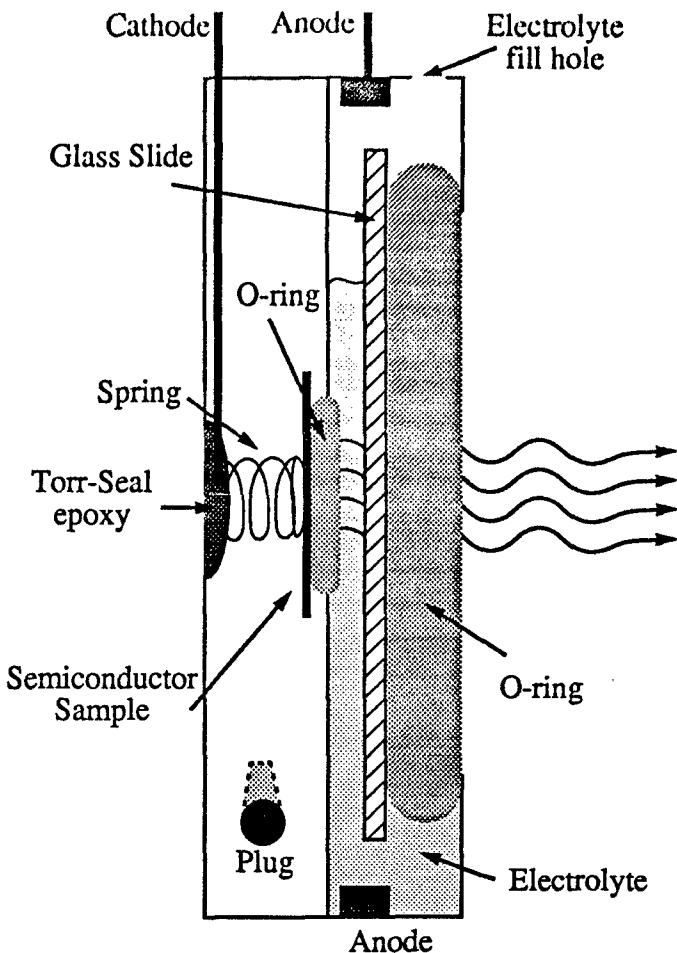


Figure 4-10. Side view of the LCLSH during LCL testing.

The left portion of the LCLSH held the semiconductor sample, which served as the cathode in LCL experiments. The bottom of the petri dish, on which the cathode wire and a metal spring were mounted, was detached from the top of the dish. The semiconductor sample to be tested was placed on a buna (nitrile) O-ring mounted at the center of the top petri dish. The inside diameter of the O-ring was $5/32"$. Contact was made to the back of the semiconductor sample by the metal spring mounted on the back of the cathodic petri dish when the two pieces of the dish were reassembled and held together with two plugs. In this picture, the p-type surface of the semiconductor laser wafer was facing to the right.

The right (front) portion of the LCLSH was designed to hold the liquid electrolyte and provide an emission window close to the p-type surface of the semiconductor sample. The cathode wire was run through the top of the front petri dish and looped around the inside edge of the dish. The center of the right petri dish was removed and a glass microscope slide was attached as the emission window, recessed from the front of the dish by use of a thick buna O-ring. Electrolyte was added to the cell via the fill hole at the top of the sample holder to a level above the position of the semiconductor sample.

A section of laser wafer GE-88-1 was tested to determine if the sample holder produced repeatable results. In order to determine the repeatability, the sample was tested, the sample holder was removed from the OMA, the GWA electrolyte was drained from the sample holder and the sample was re-prepared and retested. Each spectrum was taken three times and the averages are presented. Results for the six tests are presented in Table 4-1.

Table 4-1. Data collected to test the repeatability of the LCLSH using section #1 of wafer GE-88. The test number, drive current, and the integrated spectral count are shown. All data was collected at a drive voltage of 16 V.

Test #	Current (mA)	Average Integrated Spectral Counts (Thousands)	Procedure Performed after each Test
1	2.3	160	Drained and refilled GWA
2	2.2 & 2.3	162	Drained GWA, removed bubbles, refilled GWA. Increased resolution of multimeter.
3	2.36	162	Drained GWA, removed bubbles, refilled GWA.
4	2.37	163	Drained GWA, removed bubbles, refilled GWA.
5	2.29	160	Drained GWA, removed bubbles, refilled GWA.
6	2.30	154	

Based on this test, we determined that the LCLSH produced repeatable results as designed. We have used this LCLSH extensively during experiments reported on in both this chapter and Chapter 5.

CHAPTER 5

LIQUID CONTACT LUMINESCENCE - DISPLAYS

Because of the bright emission properties of LCL, it has been proposed that displays incorporating LCL as the light emission source would be possible. If this is to be the case, then several problems inherent in the early LCL results needed to be solved. Chief among these problems were bubble formation and low cell efficiency. Unfortunately, as was described in Chapter 3, the electrolysis of water (which produces H₂ bubbles at the semiconductor cathode) is the LCL current flow mechanism using the GWA electrolyte. Simultaneously, the conductivity of the GWA electrolyte is low, resulting in low LCL power efficiency. In order to solve these problems, we performed a literature search to obtain more information about electrolytes used in electrochemistry. This chapter explores the electrochemistry of the semiconductor electrode-liquid electrolyte interface and photoelectrochemistry experiments that sought to employ reactions at this interface to generate chemical fuels and electrical power from sunlight. Based on these chemical processes occurring in the electrochemical cell, we redesigned our electrolyte and tested these new electrolytes, which demonstrated improved characteristics over the standard GWA electrolyte. Using these non-aqueous electrolytes, we have accomplished the first demonstration of light emission from semiconductor laser materials using non-aqueous liquid contacts. Resistance measurements for new solvent/electrolyte/redox couple solutions are discussed and comparisons of the light emission characteristics of several non-aqueous electrolytic solutions as a function of supporting electrolyte molarity are presented.

Finally, lifetests were performed using some of these non-aqueous solutions and we report on these results and conclusions drawn from the experimental data.

5.1 Photoelectrochemical Introduction

In order to improve the LCL process for possible display applications, we performed a literature search into previous research employing liquid contacts and semiconductor materials. We found that there was a significant body of work related to the development of photoelectrochemical cells useful for solar energy conversion [Tan94]. Funded largely in the 1970's and early 1980's, this research had promised to use liquid junction solar cells to generate either electricity or chemical fuels.

In photoelectrochemical (PEC) cells, two electrodes, one metallic and one semiconducting, are immersed in a liquid and exposed to sunlight. The incident sunlight is absorbed near the surface of the semiconducting electrode, creating electron-hole pairs. In order to obtain useful current flow in the circuit, the electron-hole pairs need to be separated before they can recombine. It is surreptitious that a large electric field is created at the interface between the semiconductor and the liquid electrolyte. This field develops spontaneously when two material phases with different chemical properties are brought into contact. For electrical engineers, a widely used example of this phenomenon is an n-type and p-type semiconductor brought into intimate contact.

As is well known, charge carriers will redistribute after intimate contact to equalize the chemical potential throughout the semiconductor, resulting in band-bending and a built-in electric field. A similar situation is obtained in an electrochemical cell as shown in Figure 5-1. In this figure, E_c and E_v represent the conduction band and valence band edges in the semiconductor, respectively. E_f represents the Fermi level in the semiconduc-

tor and $E(A/A^-)$ represents the solution electrochemical potential, which is analogous to the Fermi level. The symbols A/A^- are used by chemists to represent a redox couple, a concept which will be described in section 5.3. When the semiconductor and liquid are brought into contact, charge transfer across the interface occurs as the chemical potential throughout the system becomes constant, i.e. $E_f = E(A/A^-)$. In the example shown in the figure, it is assumed that the solution electrochemical potential is lower than the Fermi level in the semiconductor, so electrons are transferred from the semiconductor to the solution. Because the distance from the Fermi level to the conduction band edge is related to the concentration of electrons, the energy bands bend up as the electron concentration decreases near the semiconductor/solution interface.

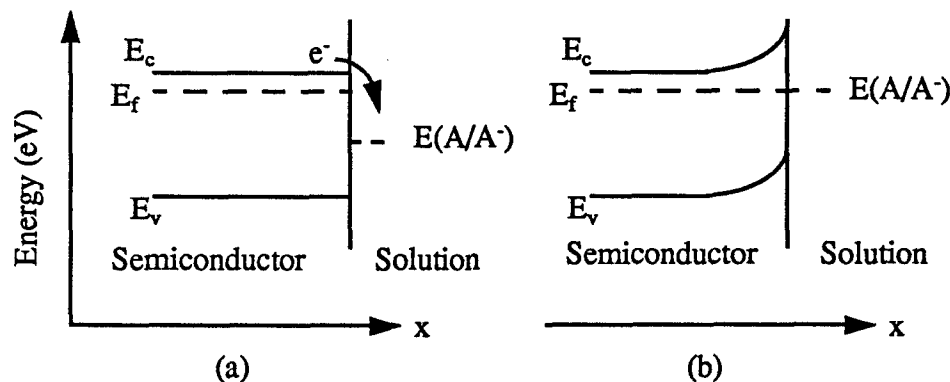


Figure 5-1. Energy band diagrams for n-type semiconductor/liquid junction at equilibrium. (a) Prior to contact and before charge equilibrium occurs. (b) After charge equilibrium has occurred. The electrochemical potential is constant at all points, $E_f = E(A/A^-)$.

The built-in electric field that is developed at the semiconductor/liquid interface separates the electron-hole pairs created by the absorption of incident light as mentioned above. These electron-hole pairs, which could recombine if they were not separated, produce current flow in the external circuit, in a fashion similar to photoelectric devices.

An application of photoelectrochemical cells, which will be discussed briefly here, is the ability of these cells to generate chemical fuels [Lewi95]. This is a capability not available using semiconductor photoelectrics, which can only produce electrical energy, but cannot directly convert incident photon energy into chemical fuels, which can be easily stored. A representative fuel-forming cell with water as the electrolyte is shown in Figure 5-2. In such a cell, electrons are injected into the water from the metal electrode to

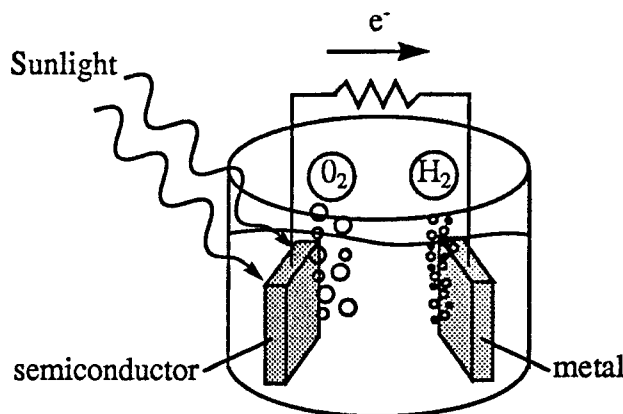


Figure 5-2. Fuel generating photoelectrochemical cell. Absorbed sunlight produces current flow and the photoelectrolysis of water into hydrogen and oxygen. These gases can be stored for future energy generation.

combine with H^+ ions and produce hydrogen (H_2) gas. The circuit is completed by the extraction of electrons from the liquid at the semiconductor, resulting in the production of oxygen (O_2) gas. These gases can be stored and later burned to produce energy. Unfortunately, most semiconductor electrodes are oxidized during this process and the resulting corrosion causes the conversion efficiency to drop rapidly. In fact, Si and GaAs, which are readily available and are nearly ideal candidates because their absorption profiles are closely matched to the solar spectrum, oxidize readily and form insulating layers that stop current flow. At the same time, semiconductors with large bandgaps, which can sustain the photoelectrolysis of water without corrosion, do not absorb an appreciable portion of

the incident sunlight. As a result, fuel generating photoelectrochemical cells have not found applications in solar energy conversion.

One approach that has been used to circumvent the corrosion problem discussed above is to utilize non-aqueous electrolytic solutions that eliminate water from the cell [Gron82], [Gron83a], [Gron83b], [Lang82], [Rose84]. In these cells, the charges generated by light absorption are transferred to a chemical species (sometimes called a stabilizer) in the electrolyte that accepts an electron at one electrode and donates an electron at the other electrode. As will be seen in section 5.2, the stabilizers are also referred to as a redox couple. In this manner, current is allowed to flow in the circuit without producing corrosion of the semiconductor electrode. One should note that the use of a non-aqueous electrolyte and the resulting lack of chemical reactions precludes the fabrication of a fuel-forming cell as the stabilizers are almost universally not useful as fuels.

Taking a step back and looking at the LCL process, it is somewhat analogous to the PEC cells discussed above. These cells are similar in the sense that the main components and ingredients are light, charge carriers, and gas production. It is ironic that an issue that is a problem for us, namely the production of H₂ gas, is a desired outcome for fuel-forming cells. Figure 5-3 is a comparison between PEC and LCL cells. One can observe that the two cells feature similar processes in reverse order, almost like a semiconductor detector and a semiconductor laser. PEC fuel-forming cells use absorbed sunlight as the energy source to produce electron-hole pairs and current flow. LCL cells use an external bias provided by a battery as the energy source to produce current flow and electron-hole pairs that recombine to produce light. Therefore, the comparison between the two cells, sunlight → current or current → light generation are analogous in a mirror image fashion. In both

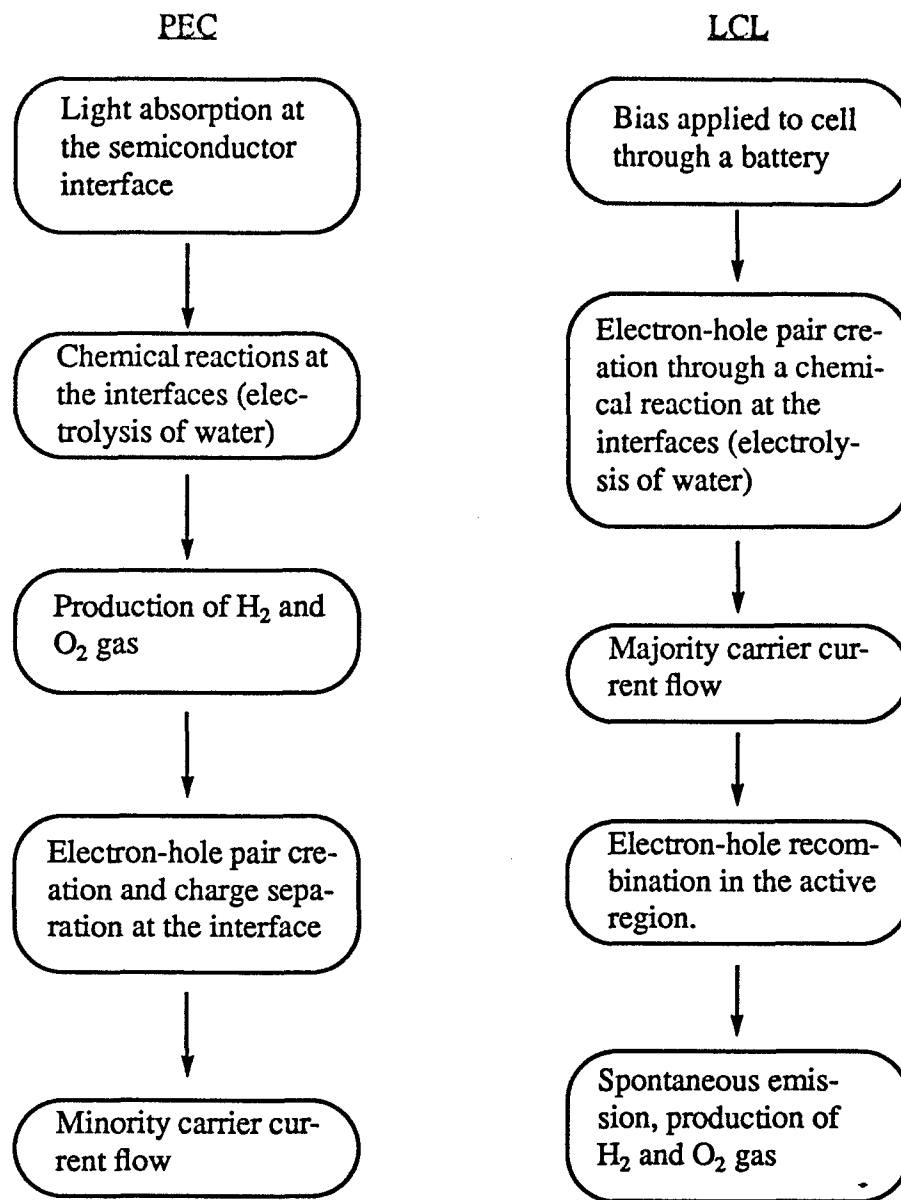


Figure 5-3. Comparison of PEC fuel-forming and LCL cells. Similarities are found in common components: light, charge carriers, current flow, and electrolysis of water.

cases, the non-aqueous electrolytes and stabilizers contribute to current flow and many of the lessons learned in PEC cells can be applied to LCL cells.

5.2 Solvents, Supporting Electrolytes, and Redox Couples

Up to this point, the liquids used for LCL electrochemistry have been referred to as electrolytes. Although this is acceptable terminology, it is now useful to more clearly define the components of the liquid electrolytic solution.

Liquids in electrochemistry are made up of a solvent, a supporting electrolyte, and a redox couple. The solvent provides a liquid medium in which the supporting electrolyte and the redox couple are dissolved. The supporting electrolyte, which can also be referred to as a salt, is an inert substance that does not participate in the electrode reactions, but increases the conductivity of the solution and thereby decreases the ohmic potential drop. Finally, a redox couple, referred to earlier in this chapter as a stabilizer, provides for electron transfer at the electrodes. All of the chemicals used for the solvent/supporting electrolyte/redox couple solutions in this work are described in detail in the appendix.

Solvents

An important aspect of a solvent's properties is the protic character (acid-base properties) of the solvent. Protic solvents are strong hydrogen bond donors, exchange protons rapidly, and have hydrogen bound to more electronegative atoms (such as fluorine, oxygen, and nitrogen). Aprotic solvents, on the other hand are poor hydrogen bond donors as they generally have hydrogen bound to carbon. They are weakly acidic and proton exchange occurs slowly. The most common non-aqueous solvents are aprotic solvents.

The use of an aprotic solvent tends to simplify the possible chemical reactions relative to those in protic solvents. This allows for the study of stable radical cations or anions that are produced by the removal or addition of an electron (simple electron trans-

fer). In our experiments, aprotic solvents were used to reduce the likelihood of hydrogen reacting at the semiconductor/liquid electrolyte interface and producing H₂ gas.

Supporting Electrolytes

The use of an inert supporting electrolyte (also referred to as a salt or an electrolyte) is indispensable in electrochemistry and affects the solvent medium in several ways:

1. Reduces cell resistance and impacts mass transport by electrical migration.
2. Largely determines the structure of the double layer.
3. May impose positive or negative voltage limits because of its redox properties.

Although technically, an electrolyte is the substance that dissociates into ions in solution, thereby becoming an electrical conductor, often the entire conducting solution is referred to as an electrolyte. In this work, electrolyte is used in both senses and the context should be used to distinguish between the dissociating substance and the general solution.

Pure organic solvents are essentially nonconductors. Without the addition of some electrolyte, their resistance is so great that passing even small currents requires impractical voltages. Therefore, the primary function of the supporting electrolyte is to provide a conducting medium. The solvent-supporting electrolyte combination should be chosen to give resistance values that are small as possible and thereby minimize *iR* drop.

When an electric field is imposed on an electrolyte solution, the ions will tend to migrate - the cations moving toward the cathode and the anions moving toward the anode. This migration of ions constitutes current flow in the cell, and each kind of ion carries a fraction of the current proportional to its mobility and concentration. For a particular value of the current, the addition of an inert electrolyte will reduce the solution resistance,

which in turn will decrease the electric field according to Ohms's law, $V=IR$. Therefore, the mass transport of an ionic electroactive species (these are the chemical species reacting at the electrodes) that is caused by migration in an electrical field can be reduced to a negligible level by "swamping" the solution with an inert electrolyte. This will result in most of the current being carried by the ions of the supporting electrolyte.

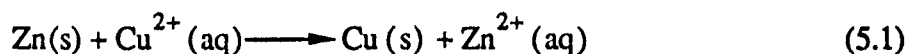
In voltammetry, the customary practice is to make the supporting electrolyte concentration at least 50 times the concentration of the electroactive species, so that electrical migration will be suppressed. In our experiments, we used lower concentrations, but we still had more electrolyte than redox couple (our electroactive species).

Redox couples

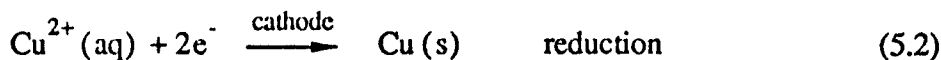
The redox couple, also referred to as a stabilizer, provides for electron transfer at the electrodes. The next section describes the redox reactions that occur at the electrodes in electrochemical cells.

5.3 Oxidation-Reduction (Redox) Reactions

All chemical reactions can be classified in two groups: reactions that involve a transfer of electrons from one reactant to another during the reaction and reactions without electron transfer. Chemical reactions in which electrons are transferred from one species to another are called oxidation-reduction reactions, commonly called redox reactions. An example of a redox reaction is the reaction between zinc and $\text{Cu}^{2+}(\text{aq})$ ions in aqueous solution:



In this reaction, the copper ion is said to be "reduced" to solid copper because of the addition of electrons:



In a complimentary fashion, the solid zinc is said to be "oxidized" as it has lost electrons:

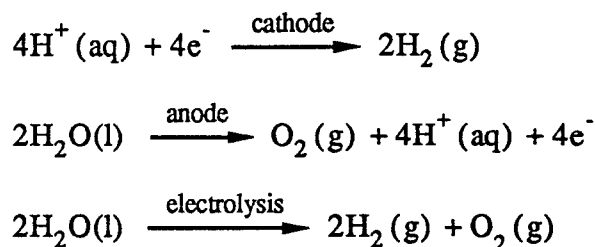


As one can see from the above reactions, the redox reaction in Eq. 5.1 can be obtained by the addition of Eq. 5.2 and Eq. 5.3. These simultaneous reduction and oxidation reactions are called half-reactions. Note that the oxidation half-reaction supplies electrons used in the reduction half-reaction. The overall chemical reaction in an electrochemical cell is really the combination of two half-reactions, which are occurring at the two electrodes in the cell. Because our interest is in the reaction occurring at the semiconductor, specifically the hydrogen bubbles being produced during the LCL process, this electrode is referred to as the working electrode, while the platinized titanium grid is referred to as the counter-electrode. In order to focus on the working electrode, standardization is accomplished by use of a reference electrode, either the normal hydrogen electrode (NHE) or the saturated calomel electrode (SCE), which has a potential of 0.242 V vs. NHE and the potential of the working electrode is measured with respect to the reference. If the working electrode is biased to negative potentials with respect to the NHE, the energy of the electrons within the electrode is raised and they will eventually flow from the electrode to the solution, resulting in a reduction current. The potential at which this current begins to flow is related to the standard potential, E^0 , for the specific chemical substances in the system.

When the potential of an electrode is biased to negative potentials, the substance that will be reduced first (assuming all possible electrode reactions are rapid) is the couple with the most positive E^0 . For example, for a platinum electrode immersed in an aqueous

solution containing 0.01 M each of Fe^{3+} , Sn^{4+} , and Ni^{2+} , in 1 M HCl, Fe^{3+} will be reduced first, since the standard potential, E^0 , for this couple is the most positive (Fe^{3+} is the easiest to reduce). On the other hand, for an electrode biased positively, the oxidation reaction will occur with the couple having the least positive E^0 . For example, for a gold electrode immersed in an aqueous solution of 0.01 M each of Sn^{2+} and Fe^{2+} , the Sn^{2+} will be oxidized first, as it has the least positive E^0 [Bard80]. Figure 5-4 presents energy diagrams for the reduction and oxidation reactions discussed above.

In the case of the initial LCL experiments, in which the electrolyte consisted of ethylene glycol, phosphoric acid, and deionized water, the reduction of hydrogen ions and the oxidation of water molecules occurred, resulting in the electrolysis of water as shown in the following equations:



At high enough voltages, the supporting electrolyte will start being reduced or oxidized and will not be inert as it reacts at the electrodes. In both polarographic and preparative electrochemistry in aprotic solvents, it is customary to use tetraalkylammonium salts as supporting electrolytes [Sawy74]. The tetrabutylammonium salts are more difficult to reduce than the tetraethylammonium salts and are preferred when maximum cathodic range is needed. For maximum anodic range, the perchlorate or tetrafluoroborate counter ions are preferred because they are not readily oxidized. In fact, the tetrafluoroborate ion

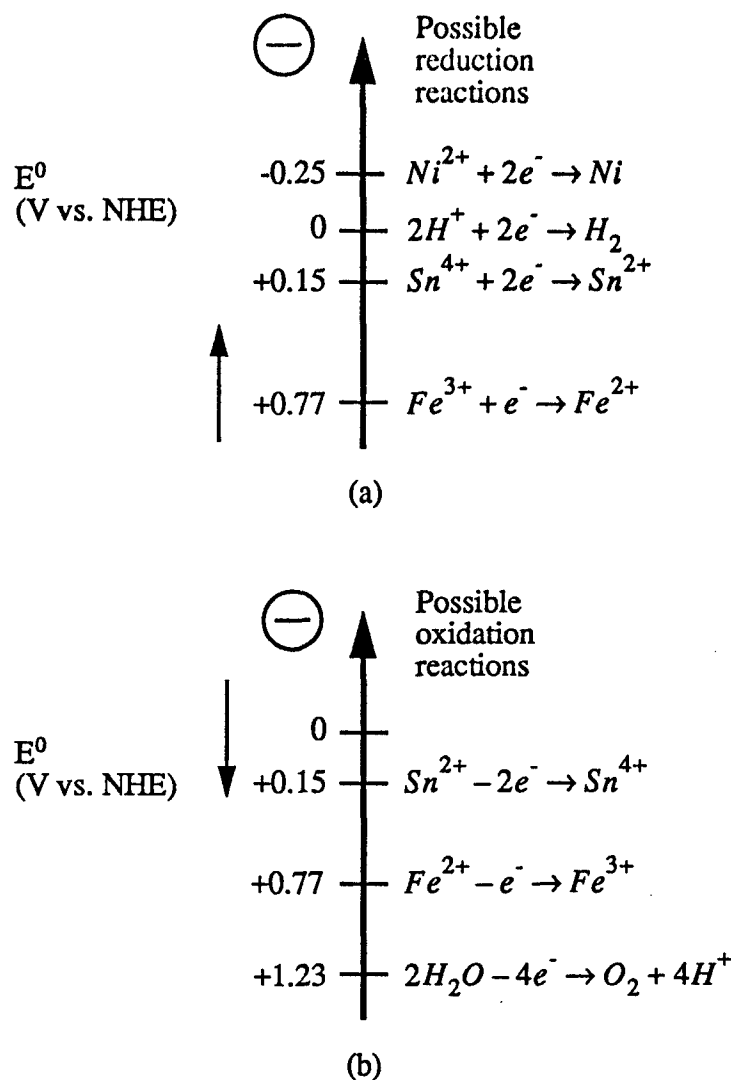


Figure 5-4. (a) Potentials for possible reductions at a platinum electrode in an aqueous solution containing 0.01 M each of Fe^{3+} , Sn^{4+} , and Ni^{2+} , in 1 M HCl. (b) Potentials for possible oxidation reactions at a gold electrode immersed in an aqueous solution of 0.01 M each of Sn^{2+} and Fe^{2+} .

gives slightly greater anodic range than the perchlorate ion. We have found that during LCL, the perchlorate ion is not inert (see section 5.8), verifying this fact.

5.4 Light Emission using Non-aqueous Solvents

Based on our improved understanding of electrochemistry, it became apparent that the GWA electrolyte, which was initially developed for pulsed anodization, was not ideal

for LCL. The protic solvent, deionized water, also served as the redox couple, resulting in H₂ bubbles. The phosphoric acid, which served as some sort of supporting electrolyte, only increased the H⁺ ion concentration, thereby increasing the probability of electrolysis.

In order to reduce or stop the electrolysis of water, two approaches were possible:

1. Use redox couples in the electrolyte solution that will react at lower potentials than hydrogen and water, or
2. Use non-aqueous electrolytes that do not contain water.

Therefore, based on this reasoning, we attempted the second option and prepared cells with a non-aqueous solvent, a supporting electrolyte, and a redox couple [Casa91], [Kohl79a], [Kohl79b]. The LCL cells were similar in geometry to the cells used for pulsed anodization and power was provided by a cw power supply. To verify that the setup was in good working order, we tested the sample (X971, $\lambda=630$ nm) for LCL emission using the GWA electrolyte. We subsequently cleaned and dried the grid and sample using DI water and N₂, a process that was repeated after each combination.

Based on the literature regarding photoelectrochemistry, several non-aqueous solvents were possible candidates. Acetonitrile (methyl cyanide) is widely used with several electrolytes. However, the lack of suitable vent hoods in our laboratories which contained the equipment required for the collection of spectral, efficiency, and other optical and electrical data, precluded my testing solutions with acetonitrile. Two other solvents, dimethylsulfoxide (DMSO) and N,N-dimethylformamide (DMF), were rejected because they are either toxic or easily absorbed into skin (producing exposure to any toxic substances dissolved in the solvent), respectively. Two non-aqueous solvents which are non-toxic and readily available are methanol and propylene carbonate (PC). These solvents were

obtained and utilized in this experiment. Initially, we used combinations as described in Table 5-1.

Table 5-1. Solvent/electrolyte/redox couple combinations and light emission results. Abbreviations used in the table: TMPD = *N,N,N',N'* tetramethyl-*p*-phenylene diamine; TBAP = tetrabutylammonium perchlorate, TBAI = tetrabutylammonium iodide.

Solvent	Electrolyte (Molarity)	Redox Couple (Molarity)	Solution Resistance (Ω)	Bubble Formation	Light Emission
Methanol	LiClO ₄ (0.5)	Ferrocene (0.1)	200	Yes	No
Methanol	LiClO ₄ (1.0)	Ferrocene (0.05)	100	Yes	No
Methanol	LiClO ₄ (1.0)	Acetyl Ferrocene (0.1)	160	Yes	No
Methanol	LiClO ₄ (1.0)	TMPD (0.05)	†	Yes	No
Propylene Carbonate	TBAP (0.2)	Ferrocene (0.05)	300	Few at edges	Yes
Propylene Carbonate	TBAP (0.1)	TMPD (0.05)	5333*	No	Yes
Propylene Carbonate	TBAI (0.05)	Ferrocene (0.025)	4571*	No	Yes
Propylene Carbonate	TBAI (0.05)	TMPD (0.05)	6667*	No	Yes
Propylene Carbonate	LiClO ₄ (0.5)	TMPD (0.05)	2133*	Yes, small number	Initially, but quickly extinguished
† Resistance was non-linear. At 8 Volts, the current was 100 mA ($R=80 \Omega$). However, attempts to increase the voltage above 8 V resulted in additional current flow with no increase in voltage.					
* Sample holder was changed to the LCLSH.					

In all of the cases for which methanol was the solvent, a large number of bubbles were produced. In the fifth case, which used PC as the solvent, tetrabutylammonium perchlorate as the supporting electrolyte, and ferrocene as the redox couple, light emission was observed with few bubbles. This result was subsequently obtained with other supporting electrolyte/redox couple combinations dissolved in PC.

We believe that this is the first demonstration of light emission from semiconductor laser material using non-aqueous liquid contacts. Greatly reduced bubble formation and lower resistances compared to the GWA electrolyte were achieved. In the next few sections, systematic studies of the solution resistance and light emission efficiency as a function of electrolyte/redox couple combinations are described.

A finding from this experiment was that the redox couples used were not clear, but dark in color, upon dissolution in the solvent, PC, which is clear. The electrolytic solutions do not have a high extinction coefficient in the visible portion of the spectrum, but are quite absorbing if the path lengths are too long. For example, dissolution of 0.1 M ferrocene in PC produces a liquid that is translucent and has a rusty red-orange color. In lower concentrations (0.05 M), PC with ferrocene has a yellow color. Acetyl ferrocene produces a much darker red liquid and TMPD produces a purple liquid in low concentrations and becomes an almost black liquid at higher concentrations. This finding led to a redesign of the electrochemical cell geometry. In the setup used to test the initial non-aqueous solutions presented in Table 5-1, which was inherited from PA, the long optical path through the liquid absorbed light in the visible spectrum. Therefore, we redesigned the cell to minimize the distance that light traversed as it left the cell (see section 4.3).

5.5 Solution Resistance vs. Supporting Electrolyte Concentration

In order to measure the resistance of various solvent/supporting electrolyte combinations, two platinized titanium grids were placed in a beaker, which was filled with 150 ml of propylene carbonate. Leads from a pulse generator were connected to the two grids and the current flowing through the electrolyte was monitored using a $10\ \Omega$ resistor. In these resistance experiments, 0.9 g (0.05 M) of ferrocene (as a redox couple) was added to the solvent prior to the addition of any supporting electrolyte. Measurements were made of the voltage applied to the cell and the current flowing through the cell to calculate the cell resistance. The cell resistance was then tabulated as a function of supporting electrolyte molarity. Several supporting electrolytes were tested in this manner.

Lithium Chloride - LiCl was added to the cell in 0.1 g increments (16 mM increments). A plot of the resistance between the two electrodes vs. the molarity of the LiCl in solution is shown in Figure 5-5. At a molarity of approximately 50 mM, the LiCl was not totally dissolved in the solvent. As additional LiCl was added beyond this point, only a fraction of the added LiCl was dissolved, with the remainder of the salt settling in the bottom of the beaker.

Sodium Chloride - NaCl was used as the supporting electrolyte in a fashion similar to the LiCl. Figure 5-6 shows the plot of resistance of the cell vs. the molarity of NaCl in solution. At a low molarity, the salt was not totally dissolved in the PC with a large fraction of the salt settling in the bottom of the beaker.

Lithium perchlorate - LiClO_4 was dissolved in the PC and ferrocene solution in increments of 0.3 g (19 mM increments). Figure 5-7 shows the plot of the cell resistance vs. the molarity of LiClO_4 in solution.

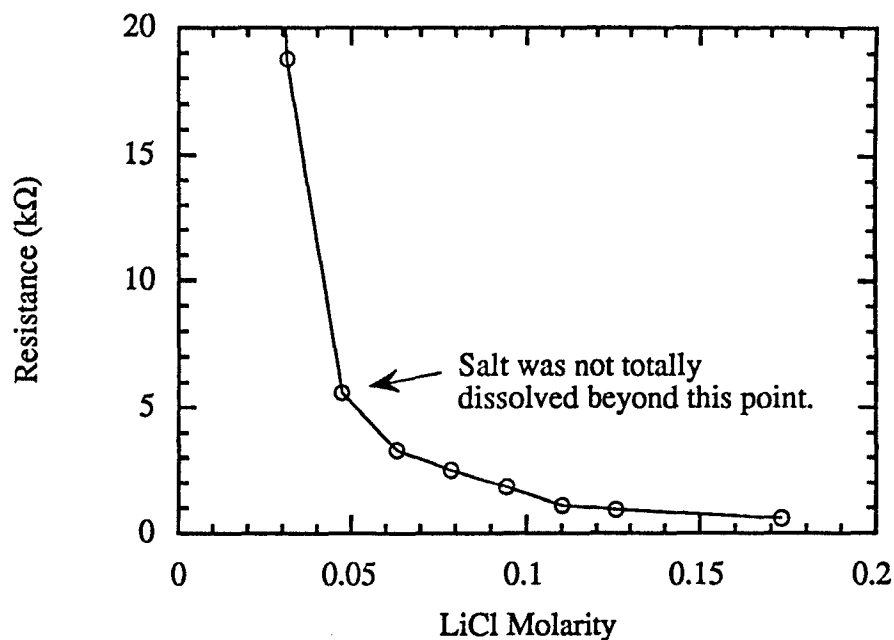


Figure 5-5. Resistance of an electrochemical cell as a function of LiCl molarity. The solvent is propylene carbonate and the redox couple is ferrocene (0.9 g).

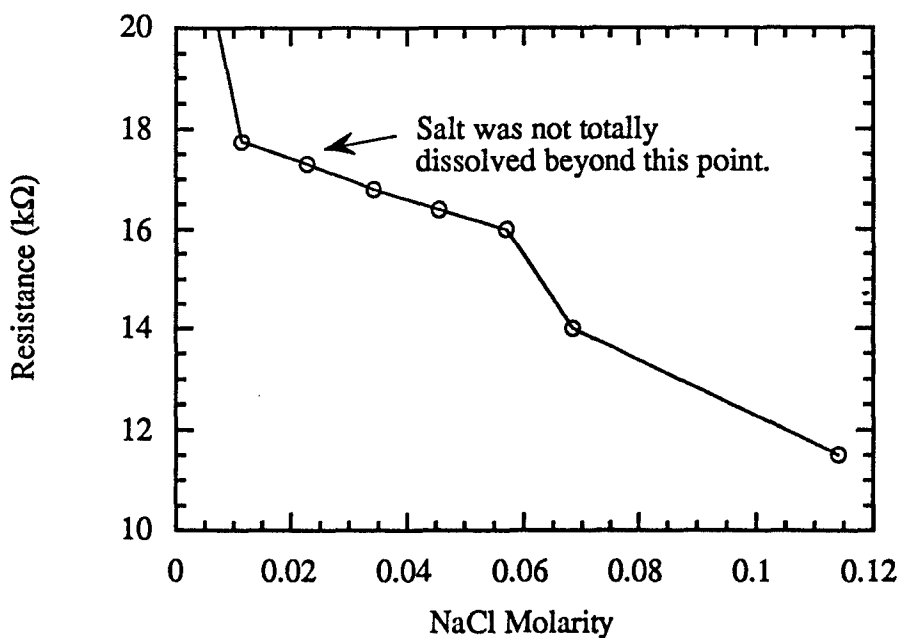


Figure 5-6. Resistance of an electrochemical cell as a function of NaCl molarity. The solvent is propylene carbonate and the redox couple is ferrocene (0.9 g).

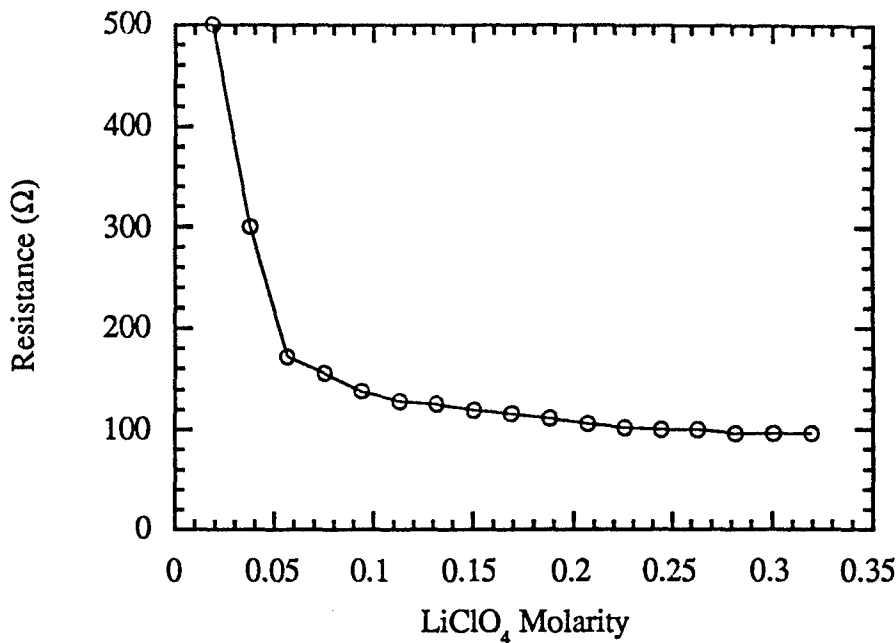


Figure 5-7. Resistance of an electrochemical cell as a function of LiClO_4 molarity. The solvent is propylene carbonate and the redox couple is ferrocene (0.9 g).

In contrast to the previous two supporting electrolytes, LiClO_4 dissolved easily in the solvent. The addition of LiClO_4 was stopped once the resistance saturated at 100Ω . It should be noted that the cell resistance obtained using this electrolyte was lower than that obtained using either LiCl or NaCl .

Tetrabutylammonium perchlorate - TBAP was dissolved in the PC and ferrocene solution in increments of 0.2 g (4 mM increments). Figure 5-8 shows the plot of resistance of the cell vs. the molarity of TBAP in solution.

Similar to the previous supporting electrolyte, LiClO_4 , TBAP dissolved easily in the solvent. Once again additional supporting electrolyte was not added once the resistance saturated at 200Ω .

Figure 5-9(a) is an overlay of the four solvent/supporting electrolyte/redox couple resistances vs. supporting electrolyte molarity. Because of the high resistance of the NaCl

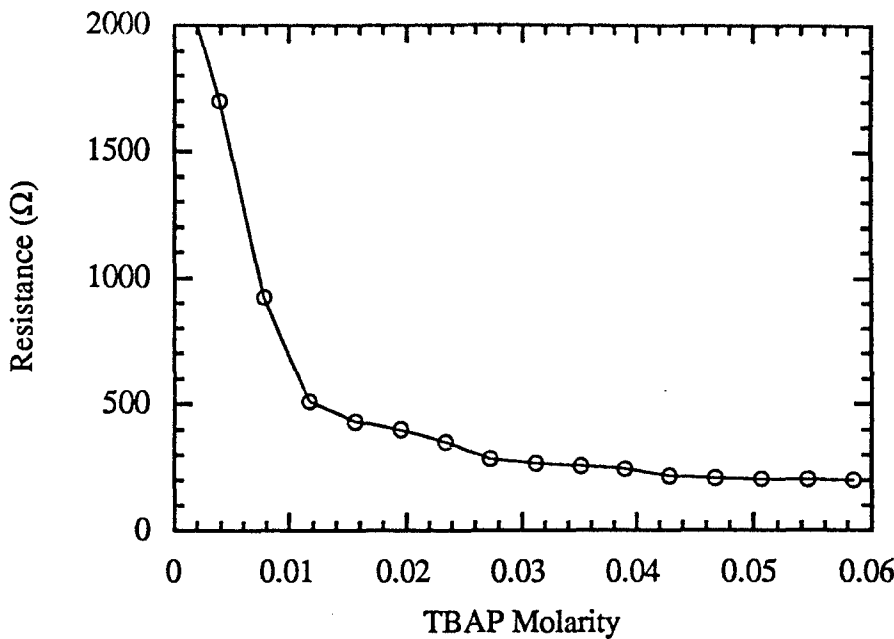
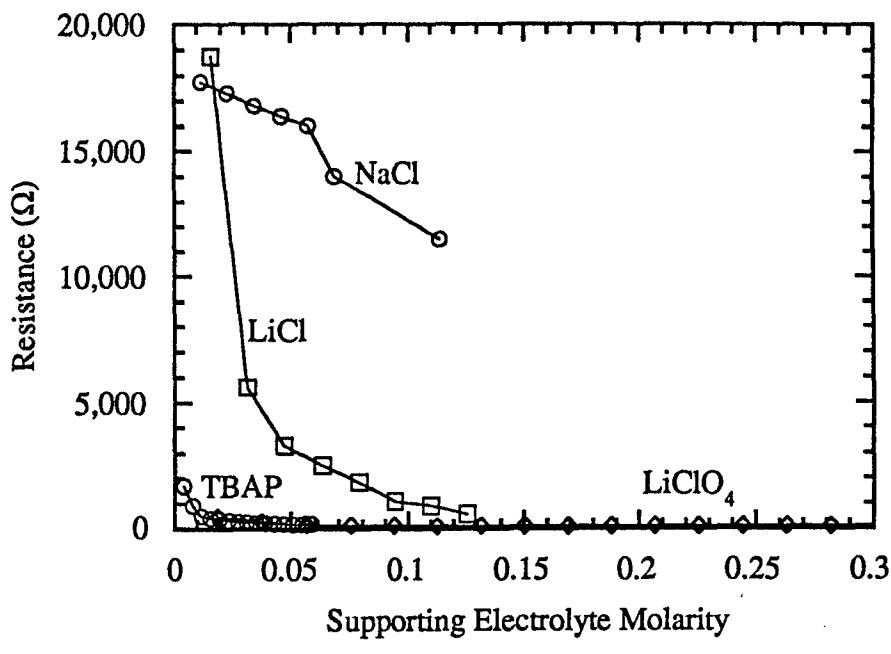


Figure 5-8. Resistance of an electrochemical cell as a function of TBAP molarity. The solvent is propylene carbonate and the redox couple is ferrocene (0.9 g).

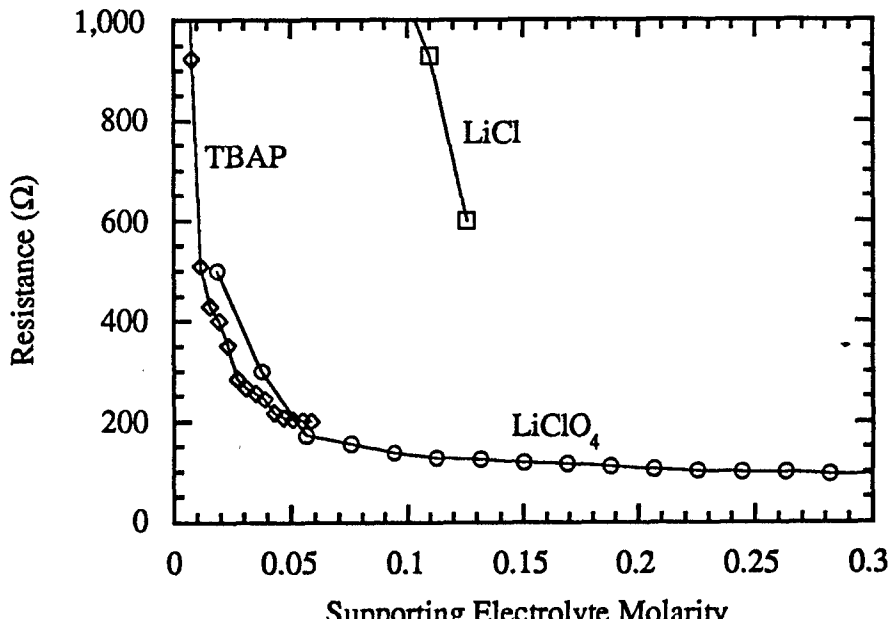
solution, it is dropped from the plot shown in Figure 5-9(b) in order to focus on the data from the LiClO₄ and TBAP cells.

5.6 Solution Resistance vs. Redox Couple Concentration

In the last section, experiments were described in which the solution resistance was decreased by the addition of supporting electrolytes. In this section similar experiments are described which determined that unlike increases in supporting electrolyte molarity, increases in redox couple molarity resulted in only minor reductions in solution resistance. Redox couples were added in 0.03 g increments to 75 ml of the solvent PC. No supporting electrolytes were added to the PC so that changes in the resistance of the cell would depend solely on the addition of the redox couples. A setup similar to that used for the resistance measurements in the previous section was used. The voltage from the



(a)



(b)

Figure 5-9. (a) Resistance of an electrochemical cell containing propylene carbonate and 0.1 g ferrocene as a function of four different supporting electrolyte molarities.
 (b) Same data except for the deletion of NaCl.

pulsed power supply was set to 6 V and the variable resistor was set to $1\text{k}\Omega$. Table 5-2 shows the results of the experiment.

Table 5-2. Resistance as a function of redox couple concentration.

Redox Couple	Initial Values		Final Values		Comments
	Current (mA)	Resistance ($\text{k}\Omega$)	Current (mA)	Resistance ($\text{k}\Omega$)	
Ferrocene	.08	74	.08	74	No change
Acetyl Ferrocene	.12	49	.18	32	Drop in resistance at 0.03 g
TMPD	.1	59	.15	39	Steady decrease

In the case of ferrocene, no changes were observed in the current flow in the cell as the redox couple was added to the cell. In the cases of acetyl ferrocene, a decrease in the resistance to $32 \text{ k}\Omega$ was observed after the initial 0.03 g of the redox couple was added. Additional increase in the molarity of the redox couple resulted in no additional decrease in resistance. In the case of TMPD, the results were slightly different from the first two cases. In this case, the resistance dropped slowly as the redox couple was added as shown in Figure 5-10.

One should note that the differences in the initial resistance values are not as significant as they may seem. In collecting this data, the initial current values were less than half a division using the smallest setting on the oscilloscope. Because the calculated resistance was inversely proportional to the measured current, small changes in current flow resulted in large differences in the calculated resistance. Additionally, all of the resistance values shown here are over two orders of magnitude larger than the resistance values

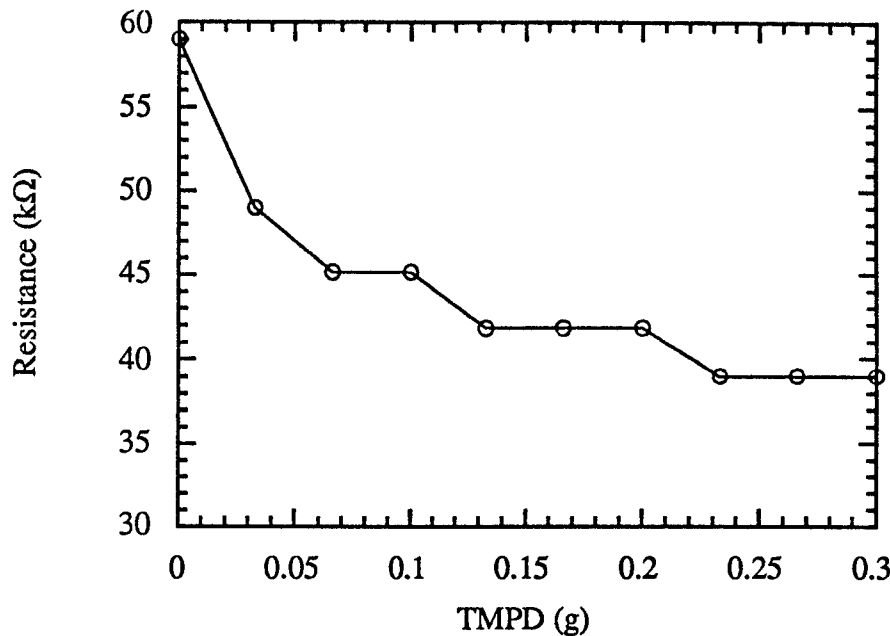


Figure 5-10. Resistance of the electrochemical cell as a function of the amount of TMPD added to the cell. Solvent is 75 ml PC.

obtained using supporting electrolytes. Therefore, the conclusion that can be drawn from this experiment is that an increase in redox couple concentration has little impact on the solution resistance. However, increasing the redox couple concentration does result in a darkening of the liquid in the cell. Because this cell darkening may result in light absorption and decreased LCL efficiency at high redox couple concentrations, it is advisable to use the smallest redox couple concentration possible.

5.7 Electrolyte Comparison

Based on the demonstration of light emission using non-aqueous electrolytes that was discussed in section 5.4 and the solution resistance measurements presented in section 5.5, we undertook a systematic study of the relationship between light emission and the composition of the non-aqueous electrolytic solution. Various combinations of supporting

electrolytes and redox couples were studied using PC as the non-aqueous solvent. Table 5-3 lists the various combinations of supporting electrolytes and redox couples tested.

Table 5-3. Supporting electrolyte/redox couple combinations used for systematic study of light emission as a function of supporting electrolyte molarity.

Supporting Electrolyte	Maximum Supporting Electrolyte Molarity	Redox Couple	Redox Couple Molarity
TBAP	0.06	Ferrocene	0.05
TBAP	0.15	TMPD	0.05
TBAI	0.06	Ferrocene	0.05
TBAI	0.04	TMPD	0.05

The first solution combination that was studied used TBAP as the supporting electrolyte and ferrocene as the redox couple. The electrolytic solution was prepared using 100 ml of PC as the solvent and 0.9 g (0.05 M) ferrocene. TBAP was then added incrementally to the solution and the light emission properties and current flow under cw LCL conditions using a constant current supply (150 V, 82.5 kΩ external resistor) were measured at each TBAP molarity. The LCLSH described in section 4.3 was drained and refilled with solution after each incremental addition. For each TBAP molarity, the current flowing in the LCL circuit was measured and three spectral profiles were measured using the OMA. These spectra were integrated using software resident in the OMA in order to obtain the integrated spectral counts. This data is presented in Figure 5-11.

As the TBAP molarity was increased, the light emission intensity, represented by the integrated spectral counts, increased. The current flowing in the cell, represented by

filled squares in the figure, also increased and began to saturate. The current increase and saturation tracks closely with the drop in resistance as shown in Figure 5-8.

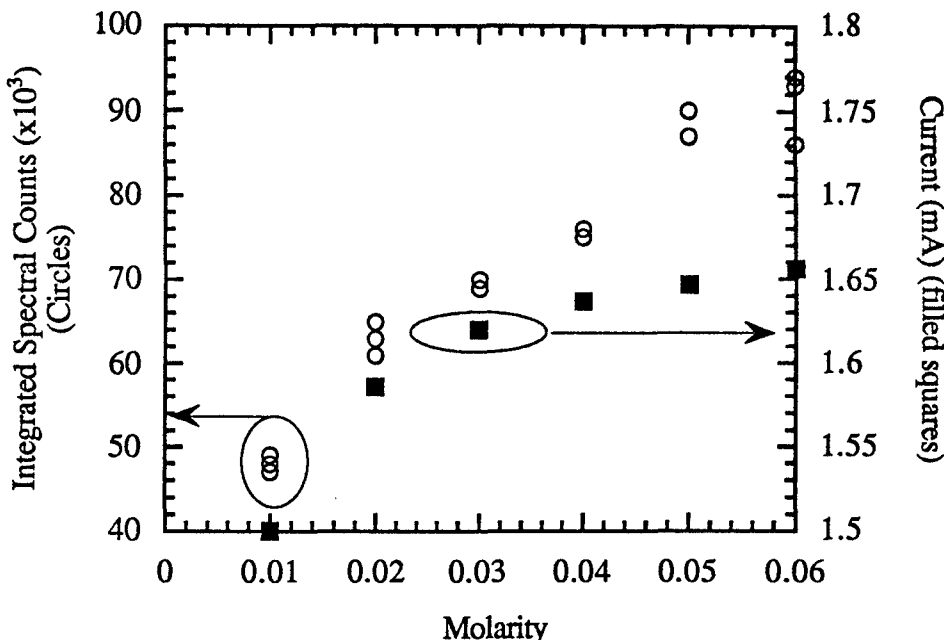


Figure 5-11. Integrated spectral counts and cell current vs. TBAP molarity in PC. The redox couple is 0.05 M ferrocene.

In addition to the use of ferrocene as the redox couple, TMPD was also employed as a redox couple with TBAP as the supporting electrolyte. Data was collected in the same manner as that described above. Figure 5-12 is a plot of the data collected for the TBAP/TMPD combination. As with TBAP/ferrocene, the emission intensity and the cell resistance decreased as the TBAP molarity was increased.

TBAI was also used as a supporting electrolyte with both ferrocene and TMPD as the redox couple. Figure 5-13 is a plot of the light emission and cell current vs. TBAI molarity with ferrocene as the redox couple, and Figure 5-14 is a plot of similar data for TMPD as the redox couple.

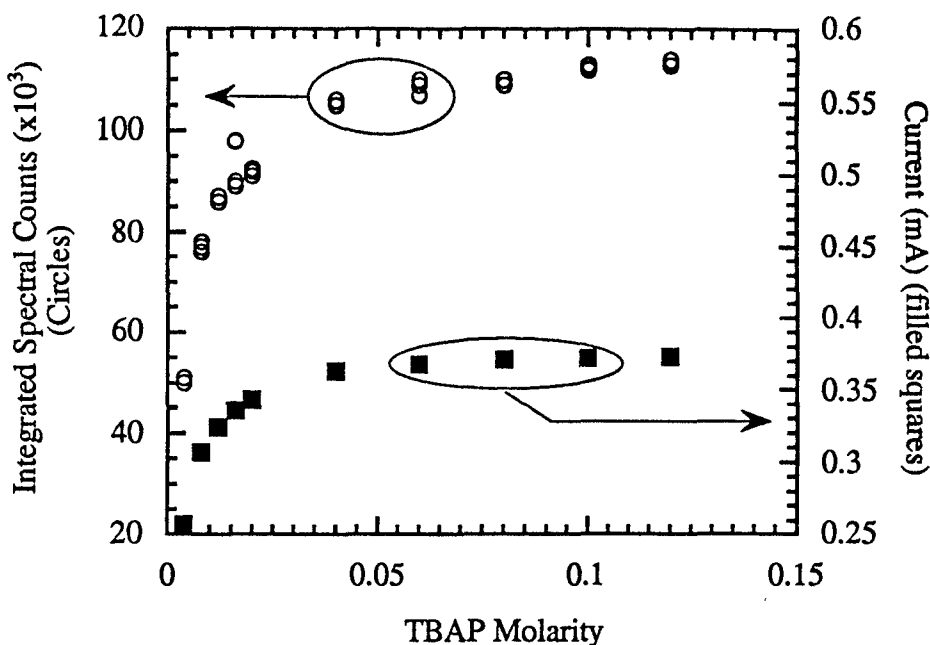


Figure 5-12. Integrated spectral counts and cell current vs. TBAP molarity in PC. The redox couple is 0.05 M TMPD.

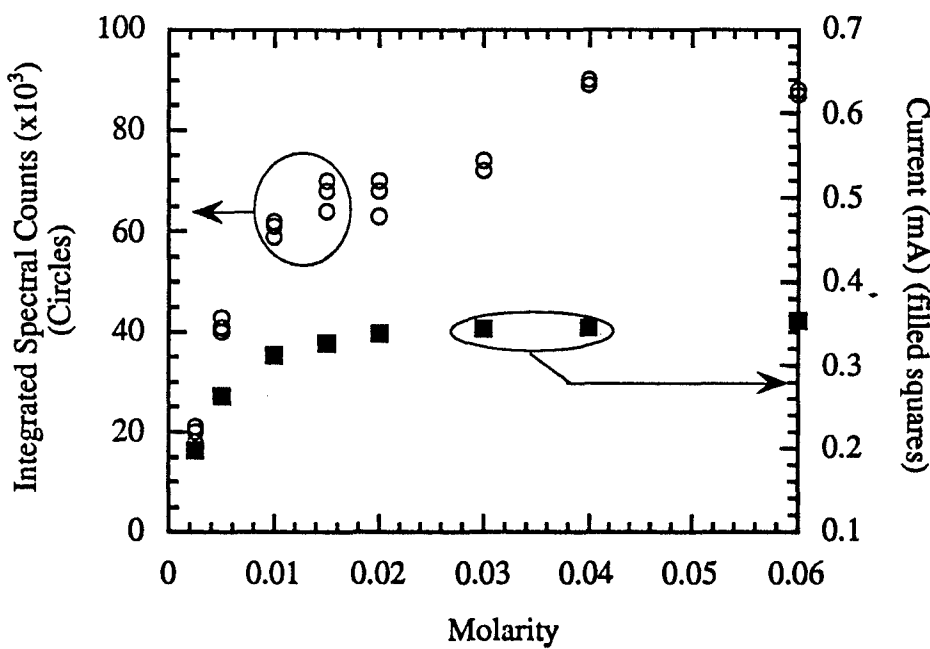


Figure 5-13. Integrated spectral counts and cell current vs. TBAI molarity in PC. The redox couple is 0.05 M ferrocene.

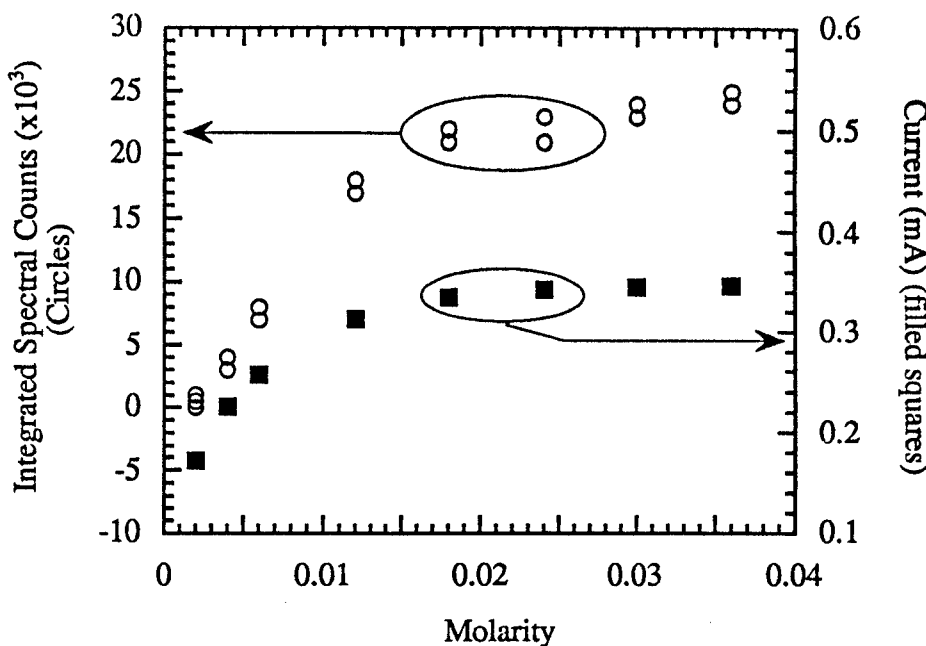


Figure 5-14. Integrated spectral counts and cell current vs. TBAI molarity in PC. The redox couple is 0.05 M TMPD.

Based on these experiments, we determined that using PC as the non-aqueous solvent, the light emission properties and electrolytic cell resistance values saturated for supporting electrolyte concentrations over 0.06 M. All of the combinations used in the systematic study produced bright luminescence and were optimized at redox couple molarities of 0.05 M and supporting electrolyte molarities equal to or slightly greater than 0.05 M.

5.8 Non-aqueous Electrolyte Lifetime Experiments

In section 4.1, the issue of luminescence temporal stability (LTS) was addressed from the point of view of diagnostics. In potential display applications using liquid contacts, this temporal stability of the emission process is also important. In fact, the temporal stability requirement for displays will be more stringent than diagnostics because of the long lifetimes expected of displays.

Using the LCLSH, samples from wafer X847 were tested under constant current LCL conditions using several supporting electrolyte/redox couple combinations dissolved in PC. In addition, the sample holder was used to test sample #3 from wafer GE88 using the GWA electrolyte.

Figure 5-15 and Figure 5-16 show the integrated spectral counts and current as a function of time for TBAP with ferrocene (Figure 5-15) and TMPD (Figure 5-16), respectively. Figure 5-17 and Figure 5-18 show the integrated spectral counts and current as a function of time for TBAI with ferrocene and TMPD, respectively. Finally, Figure 5-19 is the integrated spectral counts and current as a function of time using the GWA electrolyte.

In Figure 5-15 (TBAP/ferrocene), both the integrated spectral count and the current drop off as the LCL time increases. One can observe that after 15 minutes, the current has only decreased 3%, but the light intensity has decreased by over 20%. At the 15 minute point, the voltage on the constant current supply was increased (from 31.5 V to 32.2 V) to force the current back to the original level of 0.25 mA. Although the current was increased back to the original level, the light emission increased only slightly to a value well below the original value and then began to decrease again.

At 20 minutes, the solution was drained from the sample holder and replaced with fresh solution. The solution change at the 20 minute point appears as an open triangle (integrated spectral counts) and a filled triangle (current) in Figure 5-15. Although the current was once more set at the original value of 0.25 mA, the light emission did return to the original value. Therefore, we conclude that using TBAP as the supporting electrolyte adversely affects the semiconductor sample. From Table 5-1, it was observed that the use

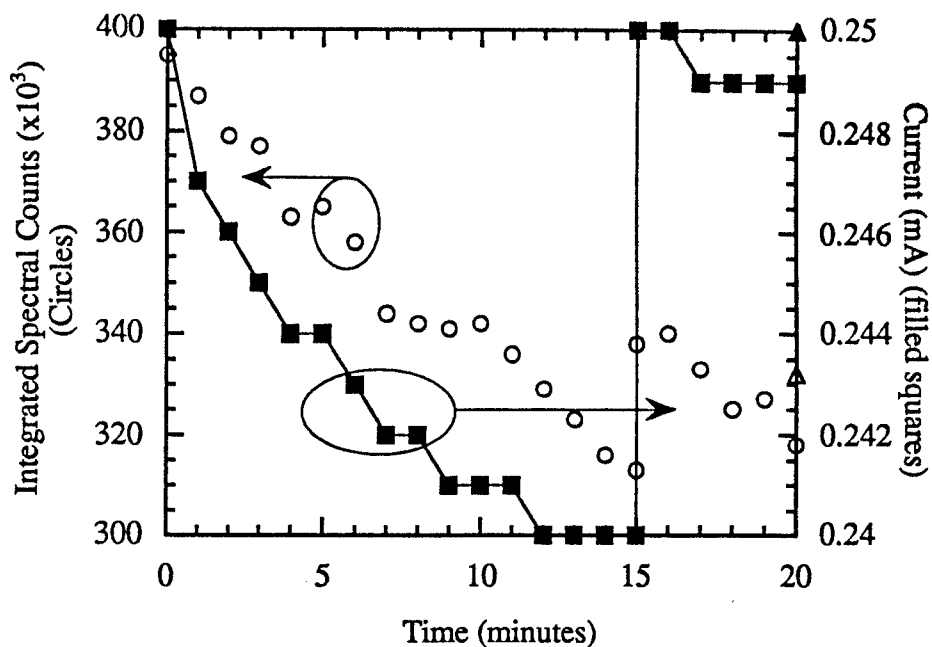


Figure 5-15. Integrated spectral counts and cell current vs. time for TBAP in PC.
The redox couple is 0.05 M ferrocene.

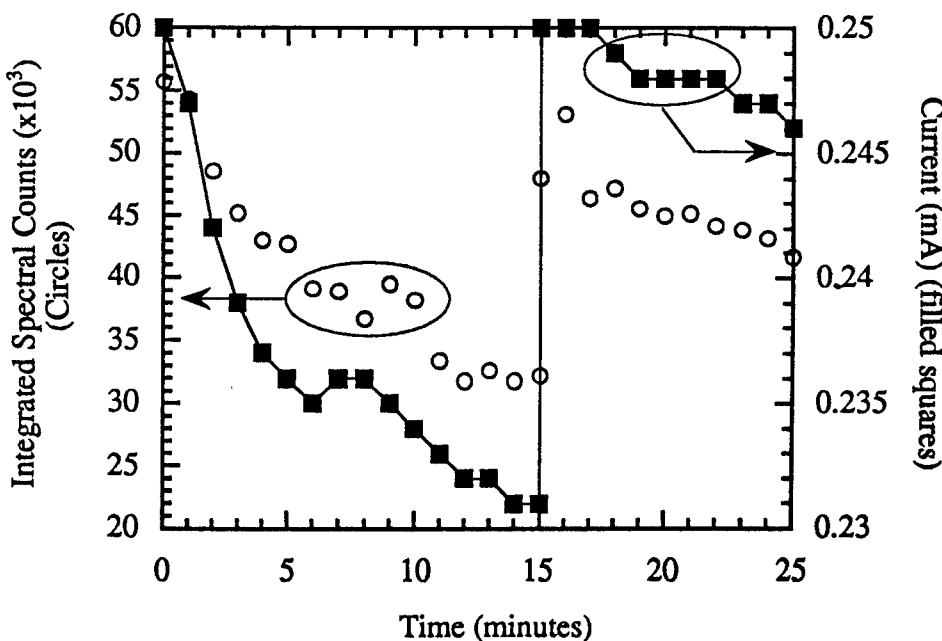


Figure 5-16. Integrated spectral counts and cell current vs. time for TBAP in PC.
The redox couple is 0.05 M TMPD.

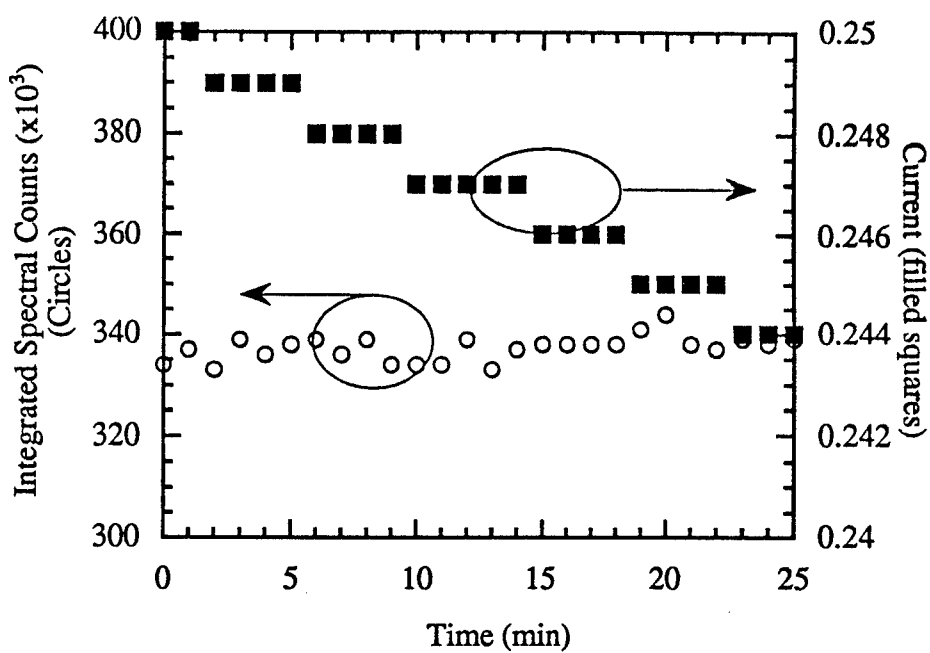


Figure 5-17. Integrated spectral counts and cell current vs. time for TBAI in PC. The redox couple is 0.05 M ferrocene.

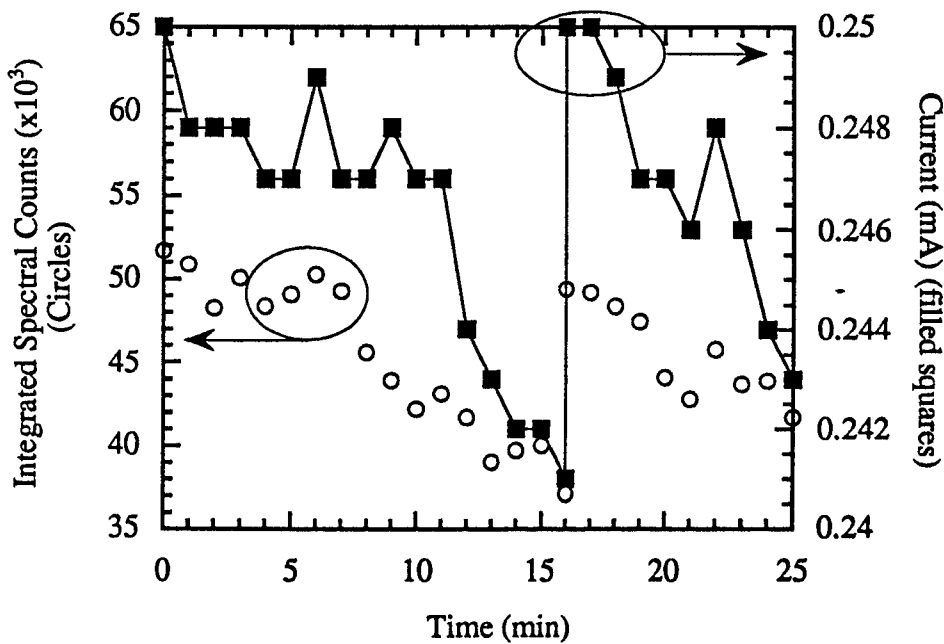


Figure 5-18. Integrated spectral counts and cell current vs. time for TBAI in PC. The redox couple is 0.05 M TMPD.

of LiClO₄ as a supporting electrolyte caused quick extinction the light emission, so one can conclude that the perchlorate ion is the source of the semiconductor degradation.

Using TMPD as the redox couple, a similar decrease in light emission and current was observed. In this case, the decrease was greater than that observed using ferrocene. The light intensity decreased by around 50% and the current decreased around 10%. At the 15 minute point, the voltage was increased from 32 V to 34 V to increase the current back to the original value of 0.25 mA. The light emission intensity increased, but once again, not back to the original level. Using TMPD as the redox couple, it was observed that a purple liquid was formed at the anode during LCL testing. This purple liquid is the oxidized form of TMPD and may have resulted in the decrease in conductivity as a function of time.

The lifetest using TBAI and ferrocene produced results different from that obtained using TBAP. In the case of TBAI/ferrocene, the light emission intensity did not decrease as a function of time. This constant light emission was observed despite the fact that the current flowing in the circuit decreased by 2% over the 25 minute test period. A variation of 2% in the light emission intensity would vary 7,000 counts on either side of the average of 337,000 counts. This variation from 330 to 343×10^3 could easily be obscured in the background noise, although no decreasing trend was observed in the data.

The results obtained for the TBAI/TMPD combination were similar to those obtained with TBAP/ferrocene. The light emission intensity decreased by about 20% while the current density decreased ~3%. At the 16 minute point, the voltage was increased from 32.2 V to 33 V, but although the current increased back to the original value, the light emission intensity did not return to the original value.

The following conclusions may be drawn from this experiment:

1. The use of supporting electrolytes containing the perchlorate ion (TBAP and LiClO₄) degrade the semiconductor sample.
2. The use of TMPD as a redox couple causes the light emission intensity and cell current to decrease as a function of time. This could be a result of the production of the oxidized form of TMPD, which has a dark purple color. The emission intensity could decrease as a result of absorption by the oxidized form of TMPD. Ideally, the oxidized form of TMPD would be reduced at the semiconductor cathode. It is possible that this reaction does not proceed in an ideal fashion, increasing the resistance of the cell and decreasing the cell current.
3. The use of the TBAI/ferrocene combination resulted in stable light emission with minimal decrease in the cell current. A possible explanation for the decrease in cell current could be that the reduced form of ferrocene (Fc⁺) is not fully oxidized at the platinumized titanium grid, resulting in an increase in cell resistance.

It was stated at the beginning of this section that these lifetime experiments were performed under constant current conditions. Due to the decrease in current measured during the tests, it appears that the current was not constant during the duration of the tests. Although the measured current varied slightly, we believe that these variations in current were due to measurement error. The current variations ranged from 100-200 μ A for these experiments, values that are below the measurement tolerance of our current test equipment. We believe that the use of a more accurate ammeter would demonstrate that the current, was, in fact, constant during these tests.

Finally, a sample (#3) from wafer GE-88 was tested to determine the impact of using GWA electrolyte in the sample holder. It was proposed in section 4.1 that proper masking of the n-side of a laser wafer would result in long lifetimes. The sample holder provided a means for testing this hypothesis as the n-side of the sample is isolated from the electrolytic solution by an O-ring. Figure 5-19 presents the integrated spectral counts and cell current as a function of time.

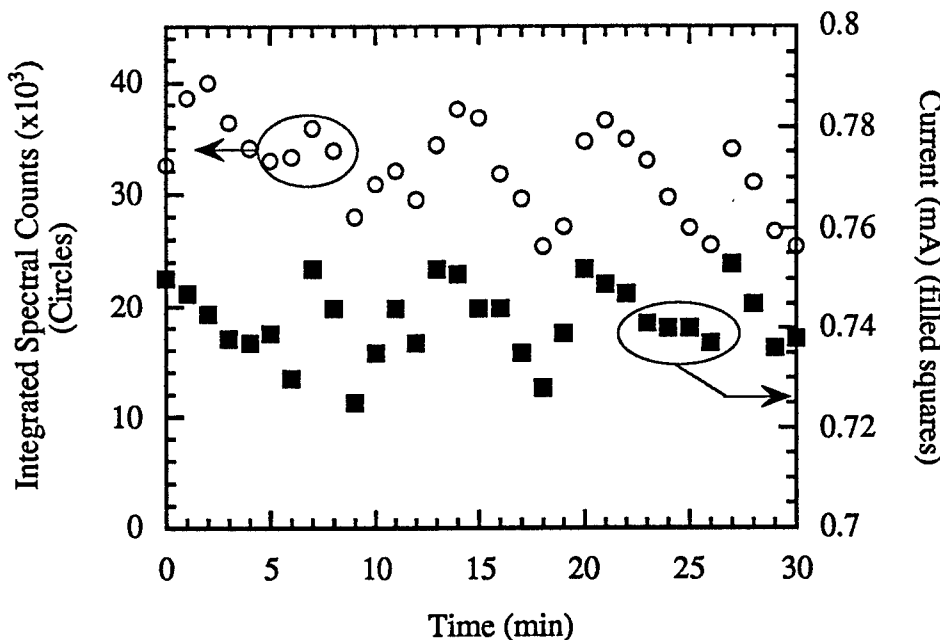


Figure 5-19. Integrated spectral counts and cell current vs. time for GWA electrolyte tested using the LCL sample holder. The voltage was fixed at 80 V for the duration of the experiment.

As predicted, the light emission and current are stable as a function of time. Variations in the emission intensity and current are believed to be due to the H₂ gas bubbles that form on the surface of the semiconductor during LCL. This effect is possibly exaggerated using the sample holder due to the fact that the bubbles tend to experience increased adherence to the sample as they are trapped at the upper lip of the O-ring.

CHAPTER 6 SUMMARY AND FUTURE DIRECTIONS

6.1 Summary

In Chapter 2, an introduction to the theory and practice of pulsed anodization (PA), a technique developed at the University of Florida that is useful for depositing native oxides on a variety of semiconductor laser materials, was provided. The first application of PA to form submicron diffraction gratings was described. Additionally, the characterization of a novel light emission mechanism, produced by electron-hole recombination in the quantum well active region, which we have named pulsed anodization luminescence (PAL), was described. Measurements of the temporal behavior of the PAL emission (the relationship between the timing of the PA current pulse and the emitted light) were used to develop a circuit model. We have used this circuit model to quantitatively describe the changes in current flow and light emission both during PA and after the termination of oxide growth.

In Chapters 3 and 4, we reported on the development and application of a novel technique that generates bright emission from semiconductor laser material using a liquid contact. We have named this technique liquid contact luminescence (LCL) and used it to characterize the material. The technique is quick, inexpensive, and nondestructive and provides information about a variety of epitaxial laser wafer material parameters, namely: peak emission wavelength, spectral linewidth, relative light emission capability versus current density, and relative values of internal quantum efficiency (η_i).

In Chapter 5, the design and testing of new electrolytic solutions based on non-aqueous solvents was described. Using these non-aqueous solutions, we accomplished the first demonstration of light emission from semiconductor laser materials using non-aqueous liquid contacts. A systematic study of these non-aqueous solutions was performed and promising lifetest results were obtained.

6.2 Future Directions - Diagnostic

Based on these successful experiments using LCL, there are several areas of research which we believe would produce profitable results upon further exploration. Foremost among the material characterization experiments is the use of LCL in a pulsed format to obtain information about the built-in charge at the p-n junction. To make the LCL sample holder more appealing for commercial applications, several improvements in the design and fabrication are proposed. Finally, the extension of the LCL technique to characterize light emitting diode (LED) materials, as well as laser materials, is proposed.

Pulsed LCL and Built-in Charge

During pulsed LCL at low current levels, it was observed that there was a temporal delay between the application of voltage to the LCL circuit and the emission of light. This observed emission delay, which could be up to 20 μ s, and capacitive effects observed in the shape of the current pulse flowing in the circuit, led us to conclude that charge rearrangement in the active region of the semiconductor laser material was occurring. Therefore, it may be possible to utilize pulsed LCL experiments to obtain useful information about the built-in charge in diode light emitters as well as information about charge traps, and the electrochemistry of the semiconductor electrode-liquid electrolyte interface.

New Cell Design

One problem encountered with the LCL sample holder during these experiments was that the cell resistance was high. Although the resistance of the solution was reduced by the addition of a supporting electrolyte, the cell geometry impeded the reduction of cell resistance. Specifically, the copper wire used for the anode in the cell had a small surface area. Additionally, it was removed from the sample by a distance equal to the radius of the petri dish, ~5 cm. In order to further reduce the cell resistance, several changes in the cell design are proposed. Incorporation of these changes may result in easier commercialization of these techniques.

The first improvement that may increase the cell conductivity would be to evaporate a layer of transparent conducting material on the glass slide directly opposite the semiconductor sample. An alternative to a transparent conductor would be the evaporation of a thin (<100 Å) layer of a noble metal such as platinum or gold. At this thickness, the losses due to absorption would be acceptable. This conducting layer would then be electrically connected to the anode and thereby significantly increase the anode surface area. Figure 6-1 is a schematic diagram that demonstrates the location of this evaporated contact. In addition to the increased anode area, additional improvement in cell conductivity would be realized due to the close proximity between the semiconductor sample and the anode.

An additional improvement in the LCL sample holder would be to machine the fixture out of a material such as Teflon®. This would require the upgrading of the O-ring from the current buna material to a Viton® or Teflon® O-ring. This inert sample holder

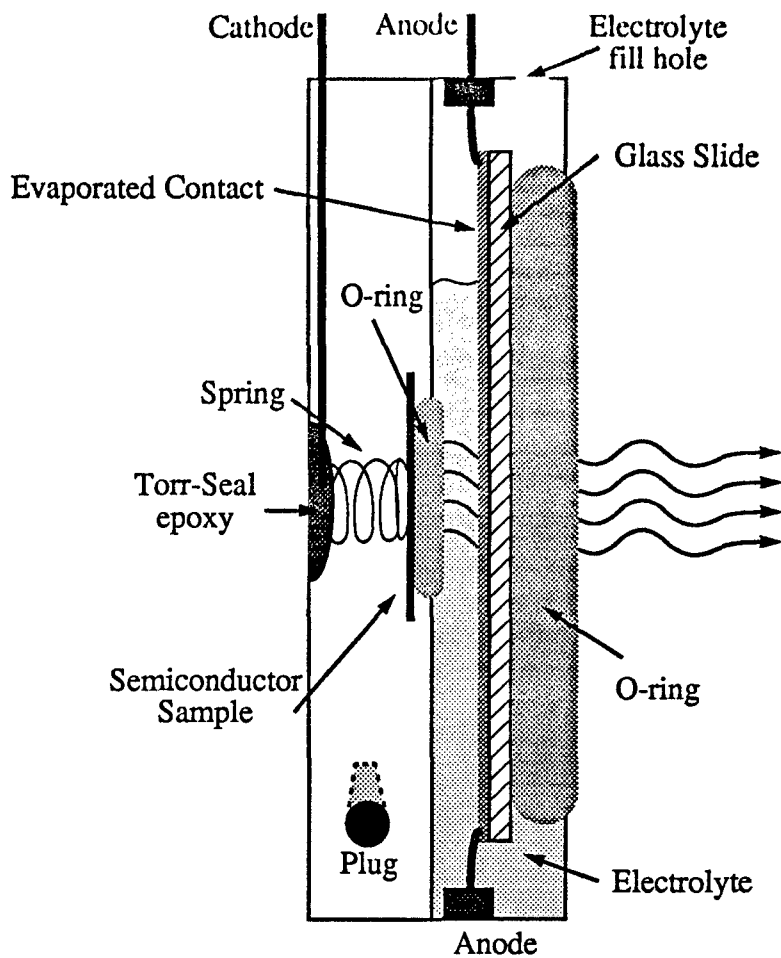


Figure 6-1. Side view of the LCL sample holder improved by the addition of a transparent contact to the glass slide.

would allow for the testing of electrolytic solutions that react with the plastic petri dish and/or O-ring currently used.

LED Material Evaluation

In these experiments, we have used state-of-the-art epitaxially grown laser materials. Since there is great commercial interest in the evaluation and improvement of materials used to fabricate LEDs, a natural extension of the LCL technique would be the evaluation of LED materials. Information similar to that obtained from semiconductor laser wafers could be obtained from LED materials. Characterization information useful

to LED material manufacturers would include spectral linewidth, peak spectral response, wafer uniformity, and wafer-to-wafer emission characteristics. This extension of LCL to include LED materials may provide a way to dramatically increase the use of LCL as a diagnostic technique.

6.3 Future Directions - Displays

If LCL is to prove useful for FPD applications, significant reductions in materials cost will be necessary. In addition, increases in luminescence lifetime and improvements in the electrolytic solution will also be required. Finally, practical FPD designs are required if LCL is to be used as the light generation mechanism used in displays.

Inexpensive LED Materials

In order to lower the cost of the materials used in the displays, LED materials could be examined for use as the light emitting component of the FPD. The relatively low cost of LED wafers in comparison to semiconductor laser wafers makes them a superior choice with respect to cost. Studies need to be performed to determine the trade-offs inherent in this change of luminescent materials. Comparisons of the luminescent efficiency of both laser and LED materials could be performed. Experiments to determine the spectral linewidth of various types of LED materials could be conducted. Additionally, the ability to obtain a wide range of peak emission wavelengths using LED materials should be examined. This variety of emission wavelengths could prove useful in the design and fabrication of full color displays.

Increased Luminescence Lifetime

In the lifetime experiments performed using non-aqueous solvents, several combinations of supporting electrolytes and redox couples resulted in emission decay as a func-

tion of time. At this time, we do not have a complete explanation for the observed emission decay. A goal for future research would be a complete understanding of these degradation mechanisms. On a fundamental level, an understanding of the processes leading to decreased light emission would be useful if one intends to fabricate long-lived cells. Additionally, knowledge of the underlying degradation mechanisms could lead to possible improvements in both the light emitting materials and the non-aqueous solutions.

Solution Improvements

As pointed out in the previous section related to improvements in the sample holder, a decrease in cell resistance is desirable. One method that may be used to decrease the cell resistance, and thereby improve the wall plug efficiency, would be to reduce the resistance of the electrolytic solution. In our experiments, supporting electrolytes were added until the solution resistance stopped decreasing. However, the number of supporting electrolytes we utilized was limited. A literature search could be undertaken to find additional supporting electrolytes that are soluble in non-aqueous solvents. Studies to determine the electrolyte solubility and solution resistance could then be performed.

An additional improvement in the electrolytic solution that would result in increased cell efficiency would be to use clear redox couples. In our experiments, the dissolution of the redox couples always resulted in coloring of the solution. Light absorption in the solution then led to decreases in light emission efficiency. Based on a literature search and experiments, it is possible that a redox couple that is clear upon dissolution could be found.

The first approach suggested in section 5.4 to reduce the hydrogen bubble production was to use a redox couple that would react at a lower potential than water. In this

approach, deionized water could be used as the solvent, a non-corrosive (inert) supporting electrolyte, like LiCl or NaCl could be dissolved to reduce the resistance of the liquid. A redox couple (Fc^+/Fc^0) that reacts with favorable kinetics and at low voltages, would provide a current flow mechanism at the electrodes to reduce the likelihood of the electrolysis of water occurring. Finally, the addition of KOH to the liquid would reduce the number of H^+ ions in solution and further discourage the electrolysis process. This reduction would occur because the equilibrium between hydrogen and hydroxide ions must always be maintained:

$$[\text{H}^+] [\text{OH}^-] = 10 \times 10^{14} \quad (6.1)$$

Initial attempts were made to utilize this proposed solution, but the redox couples we had available did not dissolve in water. An additional literature search to find redox couples that are soluble in water would allow for additional investigation of this area.

FPD Designs

Finally, the improvements in the display components described above would need to be combined with a display architecture to produce a practical FPD design. Based on the results using LED materials, it is possible that displays could be fabricated using inexpensive light emitting materials. The improved understanding of the degradation mechanisms would be combined with improvements in both the solution and cell design to produce a display design that would be characterized by long lifetimes and high efficiencies. The incorporation of these elements into a complete design would bring the LCL technique to the forefront as a viable candidate for FPD applications.

APPENDIX: CHEMICAL PROPERTIES

A.1 Non-aqueous Solvents

The solvents most widely used for dissolving organic compounds are the so-called dipolar aprotic solvents [Sawy74]. These solvents have large dielectric constants and low proton availability. This aprotic character simplifies the electrochemical reactions, producing stable radical cations or anions that are produced by the removal or addition of an electron.

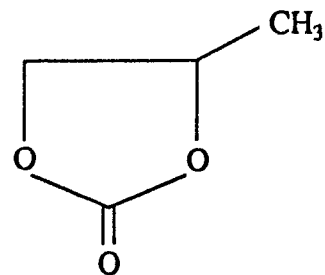
Although many solvents have been used by researchers, only a few are widely used and four solvents are employed in most applications. These four solvents are acetonitrile, propylene carbonate (PC), N,N-dimethylformamide (DMF), and dimethylsulfoxide (DMSO).

Acetonitrile

Acetonitrile has been widely used as a solvent since it resists both reduction and oxidation and is an excellent solvent for many organic compounds and some organic salts. It is stable on storage after purification and permits reasonably high conductivities. However, it is toxic and with a maximum recommended limit of 40 ppm, the vapor pressure is large enough for this to be a hazard. Due to the difficulty and inconvenience of performing all experiments under a fume hood in the microelectronics laboratory, this vapor toxicity led us to disqualify acetonitrile as a possible solvent.

Propylene Carbonate

Propylene Carbonate (4-methyldioxolane-2, 1,2 - Propanediol cyclic carbonate, PC, C₄H₆O₃).



PC has been widely used as a solvent for synthetic polymers and as a reaction medium. It is produced via a reaction of CO₂ and propylene. It is a clear, colorless liquid that readily dissolves many organic compounds and some inorganic salts. It is suitable for electrochemistry because of its resistance to oxidation and the fact that it is not hygroscopic to any great degree and is non-corrosive, although it is more viscous than acetonitrile. Both radical cations and anions are stable in the solvent and it has been widely used in battery research. A feature that has made PC attractive to us compared to some other electrochemical solvents is its low toxicity (a benefit not enjoyed by acetonitrile, DFM, or DMSO). The low toxicity has allowed for experiments to be performed without the use of a fume hood.

N,N-dimethylformamide

N,N-dimethylformamide (DMF) is a colorless liquid that has been widely used as an electrochemical solvent. The purified solvent cannot be stored for more than a day or so at room temperature without some decomposition and the vapor is toxic with exposure not recommended at concentrations greater than 10 ppm by volume. The instability and toxicity led us to disqualify DMF as a solvent option.

Dimethylsulfoxide

Dimethylsulfoxide (DMSO) has found use as an electrochemical solvent due to its high dielectric constant and resistance to oxidation and reduction. It is nearly odorless and is essentially nontoxic. However, it penetrates the skin rapidly, carrying any toxic solutes dissolved in it into the body. Because some of the supporting electrolytes that are dissolved in the solvent are strong oxidizing agents, DMSO was disqualified as a solvent.

A.2 Supporting Electrolytes

In some branches of electrochemistry using aprotic solvents, it has been customary to use tetraalkylammonium salts as supporting electrolytes. These supporting electrolytes have been chosen due to their resistance to reduction and oxidation. In these experiments, several supporting electrolytes have been used. They are Lithium Perchlorate, Lithium Chloride, Sodium Chloride, Tetrabutylammonium Perchlorate, and Tetrabutylammonium Iodide.

Lithium Perchlorate

Lithium Perchlorate (LiClO_4). White powder. Solubility in water @ 25° is 37.5%. Appreciably soluble in alcohol, acetone, ether, ethyl acetate. Soluble in PC. FW = 106.4.

Lithium Chloride

Lithium Chloride (LiCl) - White powder. Slightly soluble in PC. FW = 42.39.

Sodium Chloride

Sodium Chloride (NaCl) - Low solubility in PC.

Tetrabutylammonium Perchlorate

Tetrabutylammonium Perchlorate (TBAP), $[\text{CH}_3(\text{CH}_2)_3]_4\text{NClO}_4$. White powder. Soluble in PC. FW = 341.92.

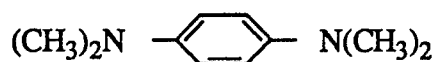
Tetrabutylammonium Iodide

Tetrabutylammonium Iodide (TBAI), $[CH_3(CH_2)_3]_4NI$. White powder. Soluble in PC. FW = 369.38.

A.3 Redox Couples

Tetramethyl-p-phenylenediamine

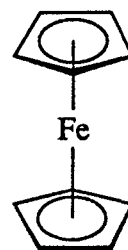
Tetramethyl-p-phenylenediamine (TMPD, N,N,N',N'-Tetramethyl-1,4-benzenediamine), $C_{10}H_{16}N_2$



TMPD is slightly soluble in cold water, more soluble in hot water, freely soluble in alcohol, chloroform, ether, and petroleum ether. Thin brown flakes. TMPD dissolves well in PC. FW = 164.25.

Ferrocene

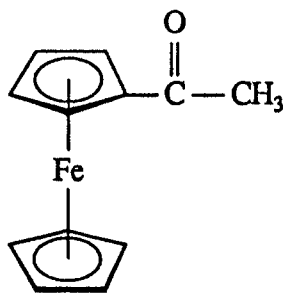
Ferrocene (cyclopentadienyliron, biscyclopentadienyliron), $C_{10}H_{10}Fe$



Practically insoluble in H_2O , 10% NaOH, and concentrated boiling HCl. Soluble in alcohol, ether, benzene. Soluble in PC. Rust colored powder. FW = 186.04.

Acetyl Ferrocene

Acetyl Ferrocene (acetylcylopentadienyliron), $C_{12}H_{12}FeO$



Acetyl Ferrocene is soluble in PC. Upon dissolution, it has a dark red color that is darker than dissolved ferrocene. Red powder. FW = 228.07.

REFERENCES

[Bard80] A.J. Bard, L.R. Faulkner, *Electrochemical Methods, Fundamentals and Applications*, John Wiley & Sons, New York, (1980).

[Bill91] S. Billat, A. Bsiesy, F. Gaspard, R. Herino, M. Ligeon, F. Muller, R. Romestain, and J.C. Vial, *Mater. Res. Soc. Fall Meeting I.T.C.*, eds. S.S. Iyer and R.T. Collins, **256**, 125 (1991).

[Bour94] D.P. Bour, R.S. Geels, D.W. Treat, T.L. Paoli, F. Ponce, R.L. Thornton, B.S. Krusor, R.D. Bringans, and D.F. Welch, *IEEE J. Quantum Electron.*, **30**, no. 2, 593 (1994).

[Casa91] L.G. Casagrande, B.J. Tufts, and N.S. Lewis, *J. Phys. Chem.*, **95**, No. 3, 1373 (1991).

[Come74] L. Comerford and P. Zory, *Appl. Phys. Lett.*, **25**, No. 4, 208 (1974).

[Ghan83] S. K. Ghandi, *VLSI Fabrication Principles*, John Wiley & Sons, New York, (1983).

[Gron82] C.M. Gronet and N.S. Lewis, *Nature*, **300**, 733 (1982).

[Gron83a] C.M. Gronet, N.S. Lewis, G. Cogan, and J. Gibbons, *Proc. Natl. Acad. Sci. USA*, **80**, 1152 (1983).

[Gron83b] C.M. Gronet and N.S. Lewis, *Appl. Phys. Lett.*, **43**, No. 1, 115 (1983).

[Grov94a] M.J. Grove, D.A. Hudson, P.S. Zory, R.J. Dalby, C.M. Harding, and A. Rosenberg, *J. Appl. Phys.*, **76**, 587 (1994).

[Grov94b] M.J. Grove, C.C. Largent, P.S. Zory, M.A. Emanuel, *Proceedings of LEOS '94*, Vol. 1, 113 (1994).

[Hase76] H. Hasegawa and H.L. Hartnagel, *J. Electrochem. Soc.*, **123**, 713 (1976).

[Hsu96] C.F. Hsu, C.C. Largent, J.S. O, C.L. Young, P.S. Zory, and D.P. Bour, *Laser Diodes and Applications*, Kurt J. Linden, Prasad R. Akkapeddi, Editors, Proc. SPIE **2682**, 136 (1996).

- [Huds94] D.A. Hudson, M.J. Grove, C. Wu, P.S. Zory, M.A. Emanuel, and R.J. Beach, *Proceedings of CLEO '94*, Baltimore, MD, 28 (1994).
- [Kohl79a] P.A. Kohl and A.J. Bard, *J. Electrochem. Soc.*, **126**, No. 1, 59 (1979).
- [Kohl79b] P.A. Kohl and A.J. Bard, *J. Electrochem. Soc.*, **126**, No. 4, 603 (1979).
- [Kova92] C.A. Koval and J.N. Howard, *Chemical Reviews*, **92**, 411 (1992).
- [Lang82] M.E. Langmuir, M.A. Parker, and R.D. Rauh, *J. Electrochem. Soc.*, **129**, No. 8, 1705 (1982).
- [Larg94] C.C. Largent, C.H. Wu, M.J. Grove, P.S. Zory, and D.P. Bour, *Proceedings of LEOS '94*, **1**, 325 (1994).
- [Larg95a] C.C. Largent, M.J. Grove, P.S. Zory, H.K. Choi, and G.W. Turner, *Laser Diodes and Applications*, Kurt J. Linden, Prasad R. Akkapeddi, Editors, Proc. SPIE **2382**, 244 (1995).
- [Larg95b] C.C. Largent, M.J. Grove, D.A. Hudson, P.S. Zory, and D.P. Bour, *Solid-State Electronics* **38**, No. 10, 1839 (1995).
- [Lewi95] N.S. Lewis, *American Scientist*, **83**, 534 (1995).
- [McQu84] D.A. McQuarrie and P.A. Rock, *General Chemistry*, W.H. Freeman & Co., New York, (1984).
- [Mull93] F. Muller, R. Herino, M. Ligeon, F. Gaspard, R. Romestain, J.C. Vial, and A. Bsiesy, *J Lumin.*, **57**, 283 (1993).
- [Rose84] M.L. Rosenbluth, C.M. Lieber, and N.S. Lewis, *Appl. Phys. Lett.*, **45**, No. 4, 423 (1984).
- [Sawy74] D.T. Sawyer, J.L. Roberts, *Experimental Electrochemistry for Chemists*, J. Wiley and Sons, New York, (1974).
- [Tan94] M.X. Tan, P.E. Laibinis, S.T. Nguyen, J.M. Kesselman, C.E. Stanton, and N.S. Lewis, *Progress in Inorganic Chemistry*, K.D. Karlin, editor, **41**, 21 (1994).
- [Turn79] G.W. Turner, J.C.C. Fan, and J.P. Salerno, *Solar Cells*, **1**, 261 (1979).
- [Wide96] R.D. Widenhofer, Master's Thesis, University of Florida, August, 1996.
- [Youn95] C.L. Young, Doctoral Dissertation, University of Florida, August, 1995.

[Zory93] P. S. Zory, *Quantum Well Lasers*, Academic Press, San Diego, (1993).

[Zory95] P.S. Zory, C.L. Young, C.F. Hsu, J.S. O, and C.C. Largent, *Proceedings of LEOS '95*, 2, 133 (1995).

BIOGRAPHICAL SKETCH

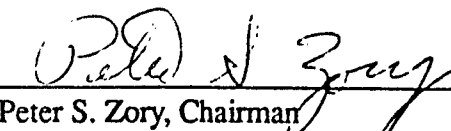
Craig Largent was born at [redacted] where his father was serving with the US Air Force. He grew up in Texas, California, and the Washington, DC area, where he graduated from Langley High School in McLean, VA, in 1983. After attending an intensive one-year Bible College program at Word of Life Bible Institute in Schroon Lake, NY, he enrolled at Northwestern University in Evanston, IL, as an Air Force ROTC scholarship cadet. At Northwestern, Craig studied electrical engineering and graduated with a Bachelor of Science in Electrical Engineering (highest distinction) in 1988. Upon graduation, he enrolled at Stanford University in Palo Alto, CA, as a Solid State Industrial Affiliates Fellow, obtaining his Master of Science in Electrical Engineering in 1989.

After earning his master's degree, Craig and his new bride, Donna, were stationed at Kirtland AFB, Albuquerque, NM, where he worked in the Semiconductor Laser Applications Branch at the Phillips Laboratory (formerly the Weapons Laboratory). Working on high power semiconductor lasers, Craig was the Phillips Laboratory Company Grade Officer of the Quarter in early 1991 and was an author and coauthor of nine technical journal articles and conference presentations. He holds one U.S. patent.

In the fall of 1993, Craig began working on his Ph.D. in electrical engineering under the direction of Dr. Peter Zory at the University of Florida. His research is focused on liquid contact luminescence and potential applications of interest to the Air Force.

Craig and his wife have one son, Chris, and they enjoy sports, travel, and attending Gator sporting events.

I certify that I have read this study and that in my opinion it conforms to acceptable standards of scholarly presentation and is fully adequate, in scope and quality, as a dissertation for the degree of Doctor of Philosophy.


Peter S. Zory

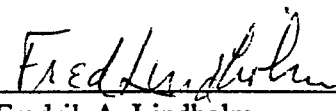
Peter S. Zory, Chairman
Professor of Electrical and Computer Engineering

I certify that I have read this study and that in my opinion it conforms to acceptable standards of scholarly presentation and is fully adequate, in scope and quality, as a dissertation for the degree of Doctor of Philosophy.


Gijs Bosman

Professor of Electrical and Computer Engineering

I certify that I have read this study and that in my opinion it conforms to acceptable standards of scholarly presentation and is fully adequate, in scope and quality, as a dissertation for the degree of Doctor of Philosophy.


Fredrik A. Lindholm

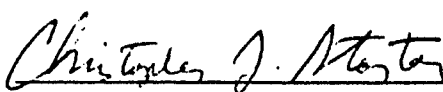
Professor of Electrical and Computer Engineering

I certify that I have read this study and that in my opinion it conforms to acceptable standards of scholarly presentation and is fully adequate, in scope and quality, as a dissertation for the degree of Doctor of Philosophy.


Ramakant Srivastava

Professor of Electrical and Computer Engineering

I certify that I have read this study and that in my opinion it conforms to acceptable standards of scholarly presentation and is fully adequate, in scope and quality, as a dissertation for the degree of Doctor of Philosophy.


Christopher J. Stanton

Professor of Physics